Density Functional Theory Studies of Surface Interactions and Electron Transfer in Porphyrins and Other Molecules

Alessandro Michael Pasquale Sena

A dissertation submitted in partial fulfillment

of the requirements for the degree of

Doctor of Philosophy

of

University College London.

London Centre for Nanotechnology

Department of Physics and Astronomy

University College London

2010

Abstract

This thesis contains a series of density functional studies on porphyrins, surfaces and other molecules, that are of relevance to surface science and electron transfer. In chapter 1 the main concepts of the thesis and how they fit together, are outlined. Chapter 2 describes density functional theory (DFT), the principle theoretical technique used throughout. The thesis then considers two main aspects. Chapters 3, 4 and 5 look at how systems interact with surfaces and compare and contrast situations of differing interaction strengths. Chapter 3 investigates the weak interaction of a haem molecule with the Si(111):H surface and studies how this interaction can be tuned by desorbing hydrogen atoms from the surface. In chapter 4, the structure of experimentally observed Mn nanolines on the Si(001) surface is studied. How these lines self assemble and interact strongly with the surface is discussed. Elements of these two studies are then combined in chapter 5 with a study of manganese porphyrin on the Si(001) surface displaying some features common to both previous systems. In chapter 6, 7 and 8 the focus switches to electron transfer. The basics of electron transfer theory are outlined in chapter 6. Then, the difficulties faced by DFT when studying electron transfer in large systems, such as the self-interaction error and cubic scaling, are described. Chapter 7 describes the constrained DFT formalism and its implementation into the linear scaling DFT code CONQUEST. In chapter 8, this implementation is used to perform some electron transfer calculations on small organic molecules, with systems demonstrating both charge localization and charge separation investigated. Chapter 9 concludes the thesis indicating how, following this thesis, large scale electron transfer calculations of organic molecules on surfaces can be performed with some confidence and giving suggestions for future calculations.

I, Alessandro Michael Pasquale Sena, confirm that the work presented in this thesis is my own. Where information has been derived from other sources, I confirm that this has been indicated in the thesis.

Acknowledgements

First and foremost I thank my supervisor David Bowler, who has provided unwavering support and guidance throughout the course of the PhD. I would also like to thank my second supervisor Andrew Fisher for his guidance, particularly during the transfer report. Post-doctoral support from Veronika Brázdova, Antonio Torralba and Alvaro Prieto has been much appreciated, especially during the ‘growing phase’ of the PhD . I also thank for similar reasons fellow PhD students Lianheng Tong and Flemming Ehlers. In addition, many thanks to Andy Gormanly for all his work on the LCN computing clusters and the members of the MOTH meeting group for providing interesting discussions throughout my time here. Finally a group of friends Angie, Aida, Mathew, Mark and Rafael that have made my time in the LCN so fulfilling and my housemates Jemima, Seraph and Gaz that have made my time out of it so fun.

Contents

List of Publications

- Density functional theory study of the iron-based porphyrin haem(b) on the Si(111):H surface.
  A.M.P. Sena, V.B. Bràzdovà, D.R. Bowler
  Phys. Rev. B, **79**, 245404, 2009.

- A density functional study of Mn nanowires on the Si(001) surface.
  A.M.P. Sena, D.R. Bowler
  In Preparation

- Linear scaling constrained density functional theory in CONQUEST.
  A.M.P. Sena, D.R. Bowler
  In Preparation

List of Figures

List of Tables

Chapter 1

Introduction

The study of atoms and molecules on nanoscale surface structures is a research area of huge technological importance [1–3]. The quantum nature of these nanoscale systems imbues them with novel properties quite unlike any classical analogue. Rapid progress in the experimental techniques available for surface science, has enabled the imaging [4], manipulation [5], control [6] and placement [7] of individual atoms and molecules on surfaces. Using these techniques to understand and exploit the novel quantum behaviour of these systems, in an attempt to construct technologically useful devices, has the potential to solve many outstanding scientific problems. Potential uses include artificial solar cells [8], hydrogen storage mediums [9], catalysts [10], gas sensors [11], and information storage [12], transport [13] and processing [14] devices.

Many different aspects determine the potential usefulness of a molecule-surface system, but two in particular will form the focus of this thesis. These are, the adsorbate-surface interaction and the electron transfer processes occurring within the system. The interaction between molecule and surface is important from both a structural and electronic standpoint. It will determine how an adsorbate binds to the surface and consequently, influence the complex's potential to be assembled easily, remain bound at a desired temperature and form specific desirable morphologies. The surface interaction will also greatly affect the molecule's electronic structure and this may open or close avenues for potential use. Electron transfer processes are very relevant, as many of the applications of surface systems involve the transfer of electrons in some way. This can be either direct transport of electrons, as in a molecular wire, or reversible transfers such as the formation and recombination of charge separated states. Investigating

electron transfer in surface-molecule systems can provide important information about their many potential applications. .

This thesis performs computational calculations on both the above themes, with the aim of providing a platform from which the electron transfer properties of surface-molecule systems can be studied. Whilst no computational methodology can hope to provide a catch-all solution to the huge array of properties that play a role in surface science problems, this work will provide a valuable contribution to a specific subset of them. In the first half of the thesis, the focus is on studying the interaction of molecules and other nanoscale systems, with the silicon surface. Two distinct systems are studied and then aspects of both are brought together in a third investigation. These works specifically investigate how interaction strengths and therefore construction paradigms, can change markedly from one system to another. The second half focuses on the study of electron transfer. First implementing a methodology that enables electron transfer to be investigated computationally in large systems. Then studying electron transfer in small molecules including some akin to those studied in the first chapter, which form the basis of larger interesting systems. The aim is to illustrate that the means and initial groundwork now exist to perform computational electron transfer calculations on large scale surface systems. The following sections of this introduction outline a number of different concepts important to the thesis, so as to illustrate how these different aspects fit together.

1.1 Common Themes

1.1.1 Surface Science

The ideas of adsorbing collections of atoms or molecules onto surfaces in order to construct potentially useful systems, can be couched in the field of surface science [3]. Surface science has been a hugely active area of research since the development of ultra-high vacuum (UHV) techniques for studying surfaces and its principle focus has always been on the technological applications of surface systems. These include uses in the industries of microelectronics, opto-electronics, catalysis and sensing. For many years, the typical length scale in surface science was the micrometer length scale. Recently, another branch of research has emerged which has applied some of the ideas

and techniques from surface science, particularly scanning probe microscopy, down at the nanoscale.

1.1.2 Nanotechnology

Nanotechnology is an umbrella term encompassing a range of varied research areas [15]. Its premise is to capture and utilize the non-classical behaviour exhibited by nanoscale systems, in order to produce novel solutions to a wide range of scientific problems. These include the miniaturization of electronic devices to below their current sizes [16], the construction of new paradigms of quantum computation and a vast array of applications in fields such as health care, clean energy and environmental applications [17].

1.1.3 Experiment and Theory

Often in nanotechnology and surface science, the focus is on providing solutions to real world technological problems. Consequently, the construction and characterization of systems that demonstrate the potential for use is often the end goal. Many of the challenges faced are engineering problems, where a proof of principle system or concept may exist and the difficulty is showing how it may be constructed reliably and repeatably. However, in two main ways, nanotechnology also benefits greatly from theoretical input. First it can be impractical to perform large numbers of experiments. Instead, by studying systems theoretically, predictions can be made about which systems are most promising and worth studying experimentally. Second, experimental results cannot always be straightforwardly interpreted and therefore theoretical analysis is important to explain the fundamental physics behind the situation and resolve any ambiguities.

1.1.4 Computational Physics

The systems to be studied are collections of nuclei and electrons. The behaviour of these nanoscale systems is governed according to the Schrödinger equation. However, this equation can only be solved analytically for a few very simple systems, such as the hydrogen atom. Approximate methods are needed to extract information about many-atom systems such as molecules or surfaces. As the processing power of computers has risen, there has been more scope to utilize them in theoretical investigations of

quantum mechanical systems. Many algorithms have been developed which allow the complicated equations governing quantum mechanical behaviour to be solved approximately. Computational physics is now used extensively to provide interpretation and guidance for ongoing and potential future experimental work. The studies in this thesis will use some of these computational methods to investigate the quantum mechanics of molecule-surface systems.

1.1.5 Density Functional Theory

Many different methods exist for calculating the electronic structure and properties of atomic systems. In particular, a large hierarchy of methods, known collectively as quantum chemistry [18], can ultimately provide very accurate answers. However, the most accurate of these are prohibitively computationally costly for systems with more than approximately 50 atoms, as their computational cost scales as $\mathcal{O}(N^4)$ up to $\mathcal{O}(N^7)$ with the number of atoms in the system. Instead, one of the most commonly used methods has been density functional theory (DFT) [19, 20]. While possessing some limitations [21], this method is able to achieve a good balance between accuracy and computational cost when calculating the ground state electronic structures for systems of up to several hundred atoms. DFT will be the primary method used throughout this thesis. It is useful not only for providing direct electronic structure information, but also enabling some post-processing, such as the production of simulated STM images, that can give extra information about a system and provide a strong link to experimental work. An explanation of DFT's theoretical formalism is given in chapter 2. Where possible, DFT results will be compared to other computational methods to ensure the conclusions drawn are not overly sensitive to the model or methods used.

1.1.6 Collaboration

An important aspect of all computational surface science, is collaboration with experimentalists. Computational physics often involves calculations where the accuracy with which a system is being treated is not perfectly characterized. Many times, methodologies may be relatively new or are being applied to a class of system untreated by them before. To ensure the methods being used are accurate, it is important to compare parts of the results to experimental work, in order to have more faith in other predictions

being made by the modelling. Often, there is also the complexity of the surface chemistry to consider, particularly when there are many possible surface arrangements and many possible surface processes could occur. Understanding how these occur through experiments alone can be challenging. In the studies performed here, efforts are made to link and compare results with experimental work, either through contact with experimental groups, or comparison with past literature. In many cases experimental groups have been contacted and have provided valuable feedback on the computational work. Results in some sections are compared with past experimental works, while in others future avenues of experimental activity are suggested.

1.2 Surface System Themes

1.2.1 Biological Molecules and Porphyrins

There have been many attempts to harness the power of biological molecules in nanotechnology. Biological systems are able to perform some very complicated tasks, with two prominent examples being the long range charge transport seen in the process of respiration and the creation of energy from light via the process of photosynthesis. They perform these so well that it is often sensible to try and utilize aspects of nature's ready made solutions, rather than create new ones. Some of the biological molecules most commonly involved in these processes are the porphyrins [22]. These carbon-nitrogen macrocycles, shown in figure 1.1, are found playing crucial roles in both respiration and photosynthesis. From gas sensors to artificial solar cells and nanowires to information storage devices, porphyrins and their man-made equivalent the phthalocyanine, have exhibited potential for use in a huge range of applications. One important feature that enables their properties to be tailored to many different applications, is the central metal atom. By changing this atom the electronic and magnetic properties of the molecule can be varied. Another important benefit is the organic carbon ring surrounding them. This both shields the metal atom and prevents it from drifting away, but also gives porphyrins various structural properties that can be advantageous, such as a strong energetic preference to remain planar due to the conjugated bonds around the ring. This gives for example, the ability to grow thin films of porphyrins which then provide ordered arrays of metal atoms. The morphology and optical properties

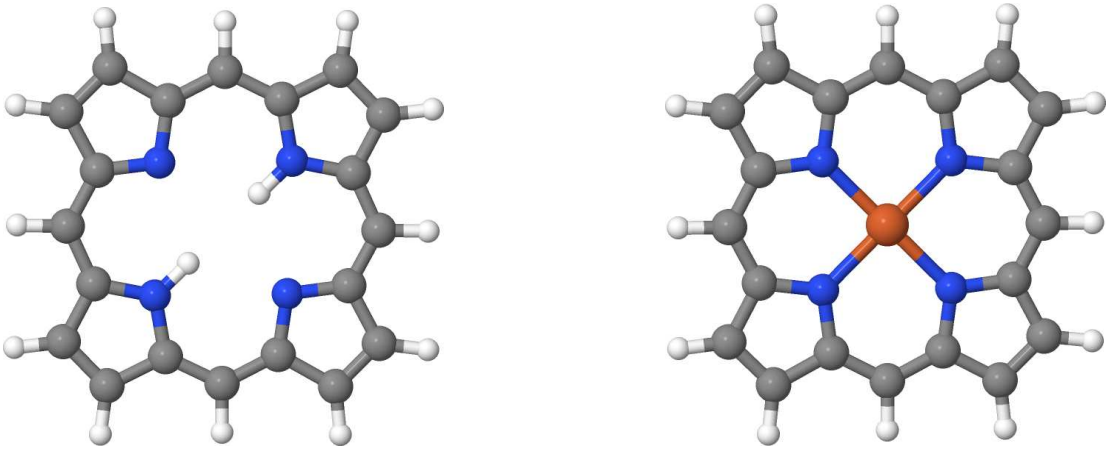

Figure 1.1: Left: Free base porphyrin molecule. Right: Metaloporphyrin molecule coordinated with an iron atom at the centre.

of these layers are often important [23]. Porphyrins can also be fashioned together in ribbon like chains [24], or even more complicated super-structures [25], both of which provide additional potential uses. Porphyrins can be functionalized with various side chains and have ligands joined to the central atom. This provides yet further possible ways of tuning their electronic and magnetic properties to a particular task, especially if the coordination of the central metal atom is changed.

1.2.2 Molecules on Surfaces

In many cases, the construction of a device requires the system to be assembled on a surface, in order to provide structural support to the molecule. When a molecule is deposited onto a surface, the electronic structure of both systems can change dramatically and what may be a useful electronic structure in the gas phase, may not be so when on a particular surface, or vice-versa. Porphyrins and phthalocyanines on surfaces have been proposed as a way of implementing a number of different systems. One example is to use the central metal atom to store information at very high densities via coupling to a magnetic surface [14]. Similarly, the construction of nanoscale wires on surfaces has also been proposed [26]. Many different surfaces have been used as substrates. Of particular relevance is the silicon surface, due to its prevalence in the semi-conductor industry. The Si(001) surface is the most important, however others are also of interest, in particular hydrogen terminated variants such as Si(001):H and Si(111):H. Passivated

surfaces can sometimes be easier to work with experimentally as the hydrogen layer makes them stable in air. They are easily prepared by dipping the surface in a hydrogen fluoride solution. For a clean surface, removing the SiO_2 layer formed during cleaving is not as straightforward. Hydrogen passivated surfaces also offer potential routes to tune interactions between molecules and surfaces, by using lithography to desorb hydrogen and create of dangling bonds on the surface.

1.2.3 Scanning Probe Microscopy

Once a molecule is on a surface, some way of imaging and manipulating its morphology is required. Scanning probe microscopy is one of the most important tools in surface science and is used to perform these tasks. There are many ways of using a probe to create an image of the surface. They all entail scanning across the surface and using the variation in the interaction between tip and sample to create a 2D map of surface. Using the interaction between tip and sample, means that the image is not diffraction limited, as is the case with microscopes, and can thus be of far higher resolution. One scanning probe that has played a huge role in nanotechnology, is the scanning tunneling microscope (STM). The STM is the most commonly used tool for providing a real space representation of the structure and electronic charge distribution of nano-structures on a surface. It can even be used to manipulate these structures and build or modify surfaces one atom at a time [5]. It is important that the computational work here is able to interface with STM images gathered by experimentalists, especially as these cannot always be unambiguously interpreted. STM images contain a combination of features from both the atomic structure and the charge density distribution and cannot give a definite distribution for each aspect independently. The density functional calculations performed in this thesis will often be used to create simulated STM images to compare with experiment [27, 28].

1.2.4 Direct vs Indirect Assembly Methods

The ability to manipulate atoms using an STM has made it possible to construct small surface structures and devices atom by atom. This is somewhat akin to the ‘factory-assembly’ methods used in industrial manufacturing and has been demonstrated in many systems such as nano-magnets or molecular switches [29]. However, the labour

intensive nature of this method and the difficulty in automating it, makes it hard to use for producing many nanoscale devices. An alternative is to search for systems which, to a greater or lesser extent, will assemble themselves. The idea of self-assembly is common in biology, where intricate systems such as DNA or large proteins will build or replicate themselves into working biological machinery. The focus here is on surface systems which may, when growth conditions such as temperature, annealing and coverage are suitable, self-assemble into a useful metastable structure or morphology. This is a more passive method of construction than direct manipulation and has greater potential for scalable repetition, however it lacks the precision and control of direct assembly. The studies in the first half will compare aspects of both direct and indirect assembly.

1.2.5 Variation of Interaction Strength

Another characteristic feature of a surface system, is the strength of interaction between the adsorbate and the surface. Strongly bound chemisorbed structures may be more useful as there is less danger of the complex dissociating once built. However, a surface that interacts strongly with adsorbates can be disadvantageous when trying to minimize impurities in a system or reduce the disturbance to an adsorbed molecule's electronic structure. The studies in the first half of the thesis feature contrasting interaction strengths and looks at ways to alter and tune the interaction strengths between system and surface. Doing so may enable beneficial aspects of strongly and weakly interacting surface structures to be combined.

1.3 Electron Transfer Themes

1.3.1 Electron Transport

In many of the technological applications that surface systems have been put to use in, the transport of electrons plays an important role. It can form part of the system's function directly, for example the charge transport along nanowires or the charge separation or recombination in artificial solar cells. And can also be important indirectly, for example determining how strongly a nanostructure may bind to a surface. Studying and harnessing the transport of electrons through nano-structures has been termed the

field of molecular electronics [30]. Molecular electronics aims to use small molecules to replicate some of the aspects of conventional electronics down at the nanoscale, with an eventual aim of creating fully functional nanoscale devices. The systems studied in the second half look at modelling charge transfer computationally using density functional methods in systems relevant to molecular electronics.

1.3.2 Marcus Theory

Harnessing electron transfer (ET) and creating molecular electronic devices from individual molecules, is a somewhat recent idea. The process of electron transfer however, has always had fundamental significance. Many chemical situations involve electron transfer and consequently much work was performed with the aim of understanding these processes. The main theoretical framework to emerge for studying charge transfer is known as Marcus Theory [31]. In its simplest form it is a classical theory with some quantum corrections, that enables the assessment of how rapidly or easily a certain system will undergo electron transfer. The studies in the second half of the thesis use DFT calculations to investigate ET in small molecules with potential nano-technological applications and looks at how to extract some of the Marcus theory parameters.

1.3.3 Constrained DFT

With the growing interest in nanotechnology and molecular electronics, the simulation of ET in molecular systems has become important. Simulating the dynamic process of electron transfer is more challenging than studying the ground state structural and assembly aspects seen in the first half. It would be desirable though, to still make use of the density functional methods due to their many advantages. There are a number of methods developed for studying electron transfer based on DFT calculations. Linear response time-dependent DFT (TDDFT) [32] can provide information on the optical properties, that is excited states, of molecules. With care, full TDDFT can even provide a dynamic picture of an ET event. Others such as the non-equilibrium Green's function method [33] are based on scattering and can give the steady-state current distribution when a voltage is applied across a system. However, these methods can be complicated to use and are most efficient with small systems. Another method, that is simple to implement and does not greatly increase the computational cost of a calculation, is

known as constrained DFT (cDFT) [34, 35]. This method adds an experimentally of physically motivated constraint to the ground state density search. It does not provide a complete picture of the process though time, but can give useful information on the start and end states of a process and therefore indicate the rate at which electron transfer events may occur. cDFT is most useful when considering electron transfer processes as individual, or a series of, discrete electron hopping events. This is often the framework considered most realistic when describing electron transfer in biological systems. In this thesis cDFT will be used to investigate electron transfer events in a variety of molecules.

1.3.4 Linear Scaling DFT

Conventional density functional theory scales cubically with the number of atoms in the system. This provides a sharp limit to the size of system that can be simulated. There are however some more complicated implementations which scale linearly with the number of atoms in the system [36]. Whilst requiring great care to use and not being applicable to every system, linear scaling DFT codes are able simulate some very large systems of the order $10,000$ atoms. Some of the most interesting electron transfer problems occur in large biological systems. Therefore the constrained DFT formalism will be implemented and bench-marked within a linear scaling code. This will enable the final thesis goal, of providing the implementation and initial background work, that better enable electron transfer to be studied computationally in large biologically and technologically relevant molecule-surface systems.

1.4 Aims and Outline of Thesis

The overall aims of the work are two fold. First, to better understand the interaction between molecules and the surfaces on which they are deposited. In particular, how the differing interaction strengths between systems and substrates can affect their properties and how the interaction strength between molecules and surfaces can be tuned. This is done through a series of studies that also provide valuable input to current experimental work. First, the interaction between haem(b) and the Si(111):H surface is investigated. Then the adsorption of Mn atoms onto the Si(001) surface is studied. Finally the two elements are combined when looking at how a Manganese porphyrin

molecule binds to the Si(001) surface.

The second aim is to provide an implementation that enables electron transfer to be studied computationally in large surface systems. This would be applicable to a broad range of surface science problems similar to those found in the first half. Then to demonstrate the method by investigating both charge separation and transfer in some technologically and biologically relevant molecules. First the implementation of constrained DFT into a linear scaling DFT code is described. Then, electron transfer calculations are performed on DNA base molecules and biphenyl molecules, which both have potential applications within larger molecular electronic systems. Finally some calculations are carried out on porphyrin molecules which also possess electron transfer applications. While only small systems are simulated here, these form the basis of interesting large scale systems to be studied in future.

Chapter 2

Density Functional Theory

This chapter outlines the basics of density functional theory (DFT) whilst also describing some extensions to the theory that will be used during the thesis. Doing so will allow the rest of the chapters to concentrate of results and analysis without stopping for methodological digressions. Further details on DFT can be found in many books, for example [37, 38].

2.1 Mathematical Tools

2.1.1 Functionals

A function takes one number as its input and returns one number as its output. It is said to map one number into another. A functional takes a function as its input and returns a number as its output. It maps a function into a number.

$$\text{Function :} \quad y(x) = x^2 \quad \rightarrow \quad y(x=2) = 4 \tag{2.1}$$

$$\text{Functional :} \quad F[y(x)] = \int_0^1 y(x)\mathrm{d}x \quad \rightarrow \quad F[y=x^2] = \frac{1}{3} \tag{2.2}$$

A functional such as 2.2 does not specify what the function to be input is, just as a function doesn't specify what the value of the variable is. The main functional used in DFT is the energy functional $E[n(\mathbf{r})]$. It acts on the electronic density, to return a number, the system energy.

2.1.2 Functional Differentiation

The energy functional of DFT must be minimized and therefore the differentiation of functionals will be an important concept. Consider a function $F[y]$ of one variable y.

The change in the function when moving from a point y_0 to another point $(y_0 + \delta y)$ is:

$$dF = F(y_0 + \delta y) - F(y_0) = F'(y)\Big|_{y_0} \mathrm{d}y \tag{2.3}$$

Then consider a situation with a number of different variables y_n. The derivative is defined as the sum of the partial derivatives:

$$dF = \frac{\partial F}{\partial y_1}\Big|_{y_0} \mathrm{d}y_1 + \frac{\partial F}{\partial y_2}\Big|_{y_0} \mathrm{d}y_2 + \ldots \tag{2.4}$$

If this is extended such that there are many variables y_n, then y becomes a function of n. In this case, y is now a function $y(n)$ and F becomes a functional $F[y(n)]$. If the domain of the function y is defined to be, say, the x axis, then $y_n = y(x_n)$, and the functional F takes as its input, *not* the value of the function at a specific point x_n, but its value at all these points. F therefore depends on the entire functional form of $y(x)$. A small change in the underlying function $y(x)$ is actually a small change in all of the points x_n, which make up this function. So the change in the functional can be written as the sum of all these changes.

$$dF = \sum_{n=1}^{N} \frac{\partial F}{\partial y_n}\Big|_{y_0} dy_n \tag{2.5}$$

Considering the intervals x_n to be small and defining the function to have limits a and b, turns the sum into a definite integral.

$$dF = \int_a^b \mathrm{d}x \frac{\delta F}{\delta y(x)}\Big|_{y_0(x)} \delta y(x) \tag{2.6}$$

This expression gives the definition of a functional derivative, but not a way to calculate it. However, the left hand side change can be calculated explicitly via

$$\mathrm{d}F = F[y + \delta y] - F[y] \tag{2.7}$$

By then equating it with the left hand side, the part that equals the differential can be found. This is best illustrated with an example as in [37].

$$T_{\mathrm{TF}}[n(\mathbf{r})] = C_F \int n^{\frac{5}{3}}(\mathbf{r})\mathrm{d}\mathrm{r} \tag{2.8}$$

$$T_{TF}[n + \delta n] = C_F \int [n^{\frac{5}{3}}(\mathbf{r}) + \frac{5}{3} n^{\frac{2}{3}}(\mathbf{r})\delta n(\mathbf{r}) + \ldots]\mathrm{d}\mathbf{r} \tag{2.9}$$

$$= T_{TF}[n(\mathbf{r})] + \frac{5}{3} C_F \int n^{\frac{2}{3}}(\mathbf{r})\delta n(\mathbf{r})\mathrm{d}\mathbf{r} + \ldots \tag{2.10}$$

Subtracting the two expressions to get the change in the functional and equating this with equation 2.6, the differential is calculated as:

$$\frac{\delta T_{TF}}{\delta n(\mathbf{r})} = \frac{5}{3} C_F n^{\frac{2}{3}} \tag{2.11}$$

2.1.3 Lagrange Multipliers

The differentiation of a function or functional to find its extrema is a common problem. It is also often necessary to find the extrema, subject to the function or functional obeying certain constraints. In this work functionals will have to be minimized subject to certain physically motivated constraints. This is done using the method of Lagrange multipliers. For example, to find the minimum of a function $f(x, y)$ under the condition $g(x, y) = 0$.

$$f(x, y) = x + 2y \tag{2.12}$$

$$g(x, y) = x^2 + y^2 - 1 \tag{2.13}$$

This is the minimum of the intersection between a tilted plane and a unit cylinder. A new function is written which consists of the old function, plus the constraint function, multiplied by a number known as the Lagrange multiplier.

$$h(x, y) = f(x, y) + \lambda g(x, y) \tag{2.14}$$

$$h(x, y) = x + 2y + \lambda(x^2 + y^2 - 1) \tag{2.15}$$

$$0 = \frac{\partial h}{\partial x} = 1 + 2\lambda x \tag{2.16}$$

$$0 = \frac{\partial h}{\partial y} = 2 + 2\lambda y \tag{2.17}$$

Along with the equation defining the constraint, this gives us three equation for three unknowns and thus can solve the problem to find the minimum subject to this constraint. For functionals the case is similar. Say $S[y(x)]$ needs to be minimized subject to $T[y(x)] = 0$. So form:

$$R[y] = S[y] + \lambda T[y] \tag{2.18}$$

and proceed in the same way, by performing functional differentiation with respect to y.

$$\frac{\delta R}{\delta y} = \frac{\delta S}{\delta y} + \lambda \frac{\delta T}{\delta y} \tag{2.19}$$

2.2 The Schrödinger Equation

The properties of matter at the nanoscale are described by the laws of quantum mechanics. The behaviour of atoms and electrons is approximately governed according to the non-relativistic Schrödinger equation (in atomic units):

$$i\frac{\partial}{\partial t}\Psi(\mathbf{r},t) = \hat{H}\Psi(\mathbf{r},t) \tag{2.20}$$

When considering a static situation, the Hamiltonian is independent of time. The equation can then be separated into spatial and time dependent parts and two separate equations for the wave-function evolution written:

$$\Psi(\mathbf{r},t) = \phi(\mathbf{r})\psi(t) \tag{2.21}$$

$$i\frac{\mathrm{d}\psi(t)}{\mathrm{d}t} = E\psi(t) \tag{2.22}$$

$$\hat{H}\phi(\mathbf{r}) = E\phi(\mathbf{r}) \tag{2.23}$$

This thesis uses a method known as Density Function Theory (DFT) to solve the second of these, the time-independent Schrödinger equation (TISE) and find the ground state wave-function of a system. The interactions within a system of atoms are described by a Hamiltonian with the following form.

$$\hat{H} = -\frac{1}{2}\sum_{i}^{N}\nabla_i^2 - \frac{1}{2m_A}\sum_{A}^{M}\nabla_A^2 - \sum_{i}^{N}\sum_{A}^{M}\frac{Z_A}{r_{iA}} + \sum_{i}^{N}\sum_{j>i}^{N}\frac{1}{r_{ij}} + \sum_{i}^{M}\sum_{B>A}^{M}\frac{Z_A Z_B}{R_{AB}} \tag{2.24}$$

where A, B count over the nuclei and i, j count over the electrons. This complicated expression can be simplified using the Born-Oppenheimer approximation. The nuclei will move much more slowly than the electrons due to them being so much heavier. Thus, the nuclear kinetic energy in this expression can be neglected to a first approximation. The indirect nuclear terms then result in a Hamiltonian with only a parametric dependence on the positions of the nuclei. Thus the wave-function in the TISE can be separated into electronic and nuclear components.

$$\Psi(\{r_i\},\{R_A\}) = \Psi(\{r_i\};\{R_A\})\Phi(\{R_A\}) \tag{2.25}$$

The equation to be solved now is that for a set of electrons surrounding a static set of nuclei which has the following Hamiltonian.

$$\hat{H}_{\mathrm{elec}} = -\frac{1}{2}\sum_{i}^{N}\nabla_i^2 - \sum_{i}^{N}\sum_{A}^{M}\frac{Z_A}{r_{iA}} + \sum_{i}^{N}\sum_{j>i}^{N}\frac{1}{r_{ij}} \tag{2.26}$$

DFT is concerned with solving a TISE with a Hamiltonian of this form.

$$\hat{H}\psi(\{r\};\{R_A\}) = \mathcal{E}(\{R_A\})\psi(\{r\};\{R_A\}) \quad (2.27)$$

$$\hat{H}|\psi\rangle = E|\psi\rangle \quad (2.28)$$

Solving this equation is difficult and only analytically possible in a few select systems, such as the hydrogen atom. To solve for a general system requires approximate computational methods, such as DFT.

2.2.1 Variational Principle

When considering how to approximately solve the TISE, the variational principle offers an indication of how to proceed. It states that:

Theorem 2.2.1 *The best approximation to the ground state wave-function is obtained by the wave-function that produces the lowest energy when acted on by the Hamiltonian.*

Mathematically it is stated as:

$$E_{\text{ground}} = \langle\psi_0|\hat{H}|\psi_0\rangle \leq \langle\psi|\hat{H}|\psi\rangle \quad (2.29)$$

This contains the basic idea of most computational methods. Try a great many different wave-functions and choose the one that gives the lowest energy. This is then the best approximation to the true wave-function.

2.2.2 Difficulties

The complicated many-body nature of the wave-function and the two electron operator $\frac{1}{r_{ij}}$ makes this idea difficult to carry out in practice. Whilst ways of solving the Coulomb problem exist, doing so whilst ensuring the many-body wave-function is anti-symmetric is challenging. Mean-field theories get round these problems using two modifications. Firstly the key point, they assume that each electron moves in an average potential created by all the other electrons in the system, rather than consider each electron's interaction with every other separately. This simplifies the Hamiltonian greatly and in turn enables the wave-function to be simplified. Now, instead of dealing with the complicated all-electron wave-function, an approximate simplified form can

be used, known as a Slater Determinant, that reduces the number of variables the wave-function depends upon, whilst still being physically sensible. There are a number of ways to proceed using these ideas. The two methods that follow are two of the most widely used and share similar concepts. In the first, the Hartree-Fock method, the focus is on the system's wave-function. While in the second, density functional theory, the system's total electron density takes the primary role. An exposition of density functional theory is clearer with knowledge of the Hartree-Fock method and therefore they are both presented.

2.3 Hartree-Fock

The main difficulty in applying the variational principle to find the ground state, is the complicated many-electron multi-dimensional nature of the state vector $|\psi\rangle$. The principle tactic of the Hartree-Fock method is to simplify this wave-function into a more tractable form. In conjunction with this it uses a mean field representation for the electron-electron interactions. First, the single and many electron terms in the Hamiltonian are put into separate groups.

$$\hat{H} = \sum_i h(i) + \sum_{i<j} v(i,j) + v_{NN} \tag{2.30}$$

$$\text{where} \quad h(i) = -\frac{\nabla_i^2}{2} - \sum_A \frac{Z_A}{r_{iA}} \tag{2.31}$$

If there was no electronic coupling, only the term $\sum_i h(i)$, it would be possible to separate the complicated many-body state vector into a product of single-electron wave-functions.

$$\Psi(r_1 \dots r_N) = \phi_i(r_1)\phi_j(r_2)\dots\phi_k(r_N) \tag{2.32}$$

This form of the wave-function is known as a Hartree-Product. Working with a product of single-electron wave-functions is far simpler than a many body wave-function. The many-electron wave-function contains information on the probability distribution for every electron in the system and accounts for how their probabilities depend on each other. In contrast the terms in a Hartree-Product are the probability distributions for individual electrons and these distributions do not depend on each other. Probability densities of single-electron wave-functions are easy to visualize; lobes can be drawn

around atoms in 3-D space to show where an electron is likely to be found. In contrast, for an all-electron wave-function this can only be done for the total charge density, not any individual electron. Only non-interacting electrons will have a wave-function of the form of a Hartree-Product. Interactions will add new features to the Hartree-Product wave-function. However, if a Hartree-Product can be modified to incorporate the effects of these interactions, then it may be possible to create a wave-function that more accurately represents the all-electron $|\psi\rangle$ without having to explicitly calculate the electron-electron interactions.

2.3.1 Slater Determinants

Anti-symmetry arises as a consequence of the indistinguishable and fermionic nature of electrons and the resulting Pauli Exclusion Principle. The Hartree-Product can be seen not to satisfy anti-symmetry. To impose anti-symmetry on a Hartree-Product, spatial orbitals ϕ are exchanged for spin-orbitals ψ, which are products of spatial and spin functions:

$$\psi(\mathbf{x}) = \chi(\omega)\phi(\mathbf{r}) \tag{2.33}$$

where ω can take values for spin up α, and spin down β, electrons. So

$$\psi_{2i-1}(\mathbf{x}) = \phi_i(\mathbf{r})\chi(\alpha) \tag{2.34}$$

$$\psi_{2i}(\mathbf{x}) = \phi_i(\mathbf{r})\chi(\beta) \tag{2.35}$$

The single-electron Schrödinger equation then reads

$$h(i)\psi_j(\mathbf{x_i}) = \epsilon_j\psi_j(\mathbf{x_i}) \tag{2.36}$$

The Hartree-Product created from these is

$$\Psi^{HP}(\mathbf{x_1}\ldots\mathbf{x_N}) = \psi_i(\mathbf{x_1})\ldots\psi_k(\mathbf{x_N}) \tag{2.37}$$

However this is not antisymmetric. Using these spin-orbitals ψ, an antisymmetric wave-function can be created by combining them in a determinant. For example, for a system with two electrons a and b.

$$\Psi^{SD}(\mathbf{x_1},\mathbf{x_2}) = \frac{1}{\sqrt{2}}(\psi_a(\mathbf{x_1})\psi_b(\mathbf{x_2}) - \psi_b(\mathbf{x_1})\psi_a(\mathbf{x_2}) \tag{2.38}$$

$$= \frac{1}{\sqrt{2}}\begin{vmatrix} \psi_a(\mathbf{x}_1) & \psi_b(\mathbf{x}_1) \\ \psi_a(\mathbf{x}_2) & \psi_b(\mathbf{x}_2) \end{vmatrix} \tag{2.39}$$

Now the use of the variational principle can now be modified slightly. Instead of searching over all wave-functions, the search is done only over the space of all Slater Determinant wave-functions.

$$E = \min(\langle \Psi_{SD} | \hat{H} | \Psi_{SD} \rangle) > \langle \Psi_{AE} | \hat{H} | \Psi_{AE} \rangle \tag{2.40}$$

This of course has the effect of reducing the variational freedom and so raising the energy found to be the minimum. The all electron wave-function is not a single Slater determinant. Using a Slater determinant is equivalent to saying that an electron moves independently of all the others, except that it feels the Coulomb repulsion due to the mean-field position of all the other electrons, and experiences an exchange interaction due the necessary asymmetry of the wave-function. For a Slater determinant wave-function, the following expression for the energy can be given after much derivation [18]:

$$E_{HF} = \langle \Psi_{SD} | \hat{H} | \Psi_{SD} \rangle = \sum_i \langle i | h(i) | i \rangle + \frac{1}{2} \sum_{i,j} [ii|jj] - [ij|ji] \tag{2.41}$$

where

$$\langle i | h(i) | j \rangle = \int \mathrm{d}\mathbf{x_1} \psi_i^*(\mathbf{x_1}) h(\mathbf{r_1}) \psi_j(\mathbf{x_1}) \tag{2.42}$$

$$[ij|kl] = \int \mathrm{d}\mathbf{x_1} \mathrm{d}\mathbf{x_2} \psi_i^*(\mathbf{x_1}) \psi_j(\mathbf{x_2}) \frac{1}{r_{12}} \psi_k^*(\mathbf{x_2}) \psi_l(\mathbf{x_1}) \tag{2.43}$$

2.3.2 Minimize the Energy

Having simplified the form of the wave-function and given the energy expression, the next step is to minimize the energy of the Slater determinant wave-function, subject to variations in the single-electron orbitals. This must be done subject to the constraint that the orbitals are orthogonal $\langle \psi_i | \psi_j \rangle = \delta_{i,j}$. That is, the total wave-function will normalize to give the correct number of electrons $\sum_i |\psi_i|^2 = N_e$. To do this method of Lagrange multipliers us used:

$$\mathcal{L}[\{\psi_i\}] = E_{HF}[\{\psi_i\}] - \sum_{i,j} \epsilon_{ij} (\langle i | j \rangle - \delta_{ij}) \tag{2.44}$$

where $\epsilon_{i,j}$ are the set of Lagrange multipliers, which become energy eigenvalues. Minimizing this expression yields, again after much algebra [18] the standard orbital form of the Hartree-Fock equation.

$$\left[h(\mathbf{x_1}) + \sum_{j \neq i} J_i(\mathbf{x_1}) - \sum_{i \neq j} K_j(\mathbf{x_1}) \right] \psi_i(\mathbf{x_1}) = \epsilon_i \psi_i(\mathbf{x_1}) \tag{2.45}$$

where

$$K_j(\mathrm{x}_1)\psi_i(\mathbf{x_1}) = \left[\int \mathrm{d}\mathbf{x_2}\psi_j^*(\mathbf{x_2})\frac{1}{r_{12}}\psi_i(\mathbf{x_2})\right]\psi_j(\mathbf{x_1}) \quad (2.46)$$

$$J_i(\mathbf{x_1})\psi_i(\mathbf{x_1}) = \left[\int \mathrm{d}\mathbf{x_2}\psi_j^*(\mathbf{x_2})\frac{1}{r_{12}}\psi_j(\mathbf{x_2})\right]\psi_i(\mathbf{x_1}) \quad (2.47)$$

K is the exchange integral and describes the exchange interaction introduced via the Slater Determinant wave-function. J is the Coulomb integral and describes the interaction of each electron with the mean field produced by all the electrons. A useful simplification is possible by noting that the two $i = j$ terms are the same for both expressions. Thus the restriction on the summation can be removed to give the set of coupled integro-differential single-electron equations as:

$$f(\mathbf{x_1})\psi_i(\mathbf{x_1}) = \epsilon_i\psi_i(\mathbf{x_1}) \quad (2.48)$$

where f is named the Fock operator. To solve these equations computationally a basis must be introduced to represent the spin orbitals. This results in the integro-differential orbital equations being turned into a set of linear equations that can be represented in matrix form. Usually in Hartree-Fock, the wave-functions are expanded as a linear combination of atomic orbitals.

$$\psi_i = \sum_{\mu=1}^{K} C_{\mu i}\chi_\mu \quad (2.49)$$

where χ_μ is an atom centred function usually taken to be a product of an angular atomic orbital part $Y_m^l(\theta,\phi)$ and a radial function $R_n(r)$ that is itself usually taken as a Gaussian, as this allows the integrals to be calculated analytically. This leads to the Roothan equations which are written as:

$$\mathbf{FC} = \mathbf{SC}\epsilon \quad (2.50)$$

As the Hamiltonian depends on the wave-function, these must then be solved in self-consistent manner to give the ground state wave-function in terms of the basis of orbitals.

2.4 Density Functional Theory

2.4.1 Introduction

The last section illustrated one way of dealing with the complicated many-particle nature of a system's state vector. Starting with a non-interacting system, add exchange

interactions by forcing the wave-function to be a Slater determinant and then treat the Coulomb interactions in a mean-field way. In this section, another closely related way of solving the TISE is explained. This method is called density functional theory and is the method used to produce all the results in the rest of the thesis. The principle idea is to replace the complicated many body wave-function with the much simpler density. The theorem of N-representability [39] states that any function $n(\mathbf{r})$ is a possible system charge density arising from a many body wave-function, so long as:

$$n(\mathbf{r}) \geq 0 \tag{2.51}$$

$$\int n(\mathbf{r})\mathrm{d}\mathbf{r} = N \tag{2.52}$$

The question is then whether this density is sufficient to determine the ground state energy and properties of the system. The two Hohenberg-Kohn theorems show that this is indeed the case.

2.4.2 Hohenberg-Kohn Theorems

The many-electron wave-function is a function of $3N$ variables and is too complicated to deal with. Hohenberg and Kohn proved two theorems that enable the electron density to be used instead. This is a far simpler quantity to deal with as it only depends on 3 variables, the spatial coordinates. The first Hohenberg-Kohn theorem is as follows:

Theorem 2.4.1 *The external potential $V_{ext}(\mathbf{r})$ is, to within a constant, a unique functional of the electronic density $n(\mathbf{r})$. Since in turn $V_{ext}(\mathbf{r})$ fixes $\hat{H}$, it is seen that the full many-particle ground state is a unique functional of $n(\mathbf{r})$.*

So the Hamiltonian and hence all the properties of a system are determined uniquely by the system's electron density. This suggests that recasting the Hamiltonian in terms of $n(\mathbf{r})$ would be a good idea.

Proof:

Assume there is an exact ground state density $n(\mathbf{r})$ and that this ground state is non-degenerate. Say there are two external potentials which produce two different Hamiltonians and hence two different wave-functions and ground state energies.

$$V_{\text{ext}}(\mathbf{r}) \rightarrow \hat{H} \rightarrow \psi \rightarrow E_0 \tag{2.53}$$

$$V'_{\text{ext}}(\mathbf{r}) \rightarrow \hat{H}' \rightarrow \psi' \rightarrow E'_0 \tag{2.54}$$

Now taking expectation values and using the variational principle:

$$E_0 = \langle\psi|\hat{H}|\psi\rangle < \langle\psi'|\hat{H}|\psi'\rangle \tag{2.55}$$

$$< \langle\psi'|\hat{H} - \hat{H}' + \hat{H}'|\psi'\rangle \tag{2.56}$$

$$< \langle\psi'|\hat{H} - \hat{H}'|\psi'\rangle + \langle\psi'|\hat{H}'|\psi'\rangle \tag{2.57}$$

$$E_0 < \int n(\mathbf{r})\left[V_{\text{ext}}(\mathbf{r}) - V'_{\text{ext}}(\mathbf{r})\right]\mathrm{d}\mathbf{r} + E'_0 \tag{2.58}$$

This calculation can be repeated but with the primes and non-prime quantities interchanged giving:

$$E'_0 < -\int n(\mathbf{r})\left[V_{\text{ext}}(\mathbf{r}) - V'_{\text{ext}}(\mathbf{r})\right]\mathrm{d}\mathbf{r} + E_0 \tag{2.59}$$

Adding these two together gives the contradiction: $E_o + E'_0 < E'_0 + E_0$. Therefore, there cannot be two V_{ext} which give rise to the same density $n(\mathbf{r})$, so each V_{ext} must give a unique density $n(\mathbf{r})$.

The fact that the density uniquely determines the energy, suggests writing the TISE in terms of the density instead of the wave-function. This is done using the Hohenberg-Kohn functional.

$$\hat{H} = \hat{H}_{\text{int}} + V_{\text{ext}} \tag{2.60}$$

$$E = \langle\psi|\hat{H}|\psi\rangle = F_{\text{HK}}[n] + \int V_{\text{ext}}(\mathbf{r})n(\mathbf{r})\mathrm{d}\mathbf{r} \tag{2.61}$$

Previously, the variational theorem suggested trying many different wave-functions in order to find the one with the minimum energy as the best approximation to the true wave-function. Now that the energy is expressed in terms of the density, an analogous idea is needed. This comes in the form of the second Hohenberg-Kohn theorem:

Theorem 2.4.2 *For a trial $\tilde{n}(\mathbf{r})$ that satisfies the boundary conditions $\tilde{n}(\mathbf{r}) \geq 0$ and $\int \tilde{n}(\mathbf{r})\mathrm{d}^3\mathbf{r} = N$ and is associated with a $\tilde{V}_{\text{ext}}$, the energy it gives is an upper bound to the true energy E_0.*

This theorem states that the energy of the system is variational with respect to the density, $E[n^0(\mathbf{r})] \leq E[\tilde{n}(\mathbf{r})]$. That is, the lowest energy is for the ground state density and any other density results in a higher energy.

Proof:

The first Hohenberg-Kohn theorem allows a density to determine its own potential, Hamiltonian and wave-function uniquely, $\tilde{n}(\mathbf{r}) \rightarrow \tilde{V}, \tilde{H}, \tilde{\psi}$. This wave-function can be used as a trial wave-function for the problem with a different external potential V.

$$\langle\tilde{\psi}|\hat{H}|\tilde{\psi}\rangle = \int \tilde{n}(\mathbf{r})V_{\text{ext}}(\mathbf{r})\mathrm{d}\mathbf{r} + F[\tilde{n}] = E[\tilde{n}] \geq E[n] = E_0 \tag{2.62}$$

Where the last step uses the conventional variational theorem to show that the energy must be greater than E_0. In summary, the second Hohenberg-Kohn theorem suggests that instead of searching variationaly over wave-functions, the search can be performed over densities.

2.4.3 Thomas-Fermi-Dirac (Orbital Free) DFT

Turning back to the energy expression, the energy of a system is given by $E = \langle\psi|\hat{H}|\psi\rangle$, with the simplified Hamiltonian.

$$E_{el} = \int \Psi^*(\sum_{i=1}^{N_{el}} -\frac{1}{2}\nabla_i^2)\Psi\mathrm{d}\mathbf{r} + \int \Psi^*(\sum_{i=1}^{N_{el}}\sum_{j=i+1}^{N_{el}} \frac{1}{|\mathbf{r_j} - \mathbf{r_i}|})\Psi\mathrm{d}\mathbf{r} + \int \Psi^*(\sum_{i=1}^{N_{el}} V_{\text{ext}}(\mathbf{r_i}))\Psi\mathrm{d}\mathbf{r} \tag{2.63}$$

The first Hohenberg-Kohn theorem showed that the energy of a system is determined entirely by the system's density. The last two terms are easily written in terms of the electron density. However the kinetic energy is not. An early attempt to write a density functional for the kinetic energy (1st term), as well as include the quantum effects not captured by the mean field Coulomb interaction (3rd term), is known as the Thomas-Fermi-Dirac (TFD) functional.

$$E_{TFD}[n] = c_1 \int n(\mathbf{r})^{\frac{5}{3}}\mathrm{d}\mathbf{r} + \frac{1}{2}\int\int \frac{n(\mathbf{r})n(\mathbf{r}')}{|\mathbf{r} - \mathbf{r}'|}\mathrm{d}\mathbf{r}\mathrm{d}\mathbf{r}' + c_2 \int n(\mathbf{r})^{\frac{4}{3}}\mathrm{d}\mathbf{r} + \int V_{\text{ext}}(\mathbf{r})n(\mathbf{r})\mathrm{d}\mathbf{r} \tag{2.64}$$

Attempts could be made to minimize this expression directly by making a guess at the density and computing the energy. This approach is known as the TFD approach to DFT. The problem with the TFD approach is simply that the density expression for

the kinetic energy is inaccurate and produces very wrong results, failing to produce the correct shell structure of atoms [40]. Therefore, the many-electron wave-function is too complicated to use in calculating the kinetic energy and it seems a good expression in terms of the density can't be found either. The solution is to make some use of the wave-function, in the same manner as Hartree-Fock, and some use of the density. The combination of these two approaches is known as Kohn-Sham density functional theory.

2.4.4 Kohn-Sham DFT

Use of the wave-function is prohibited by its complicated many body nature. The process was made easier by considering a non-interacting system of electrons and then adding the interactions in a mean field manner.

$$H_{\text{eff}} = \sum_{i=1}^{N_{el}} -\frac{\nabla_i^2}{2} + \sum_{i=1}^{N_{el}} V_{\text{ave}}(\mathbf{r_i}) + \sum_{i=1}^{N_{el}} V_{\text{eff}}(\mathbf{r_i}) \tag{2.65}$$

$$= \sum_{i=1}^{N_{el}} \left[-\frac{\nabla_i^2}{2} + V_{\text{eff}}(\mathbf{r_i}) \right] = \sum_{i=1}^{N_{el}} h(\mathbf{r_i}) \tag{2.66}$$

If the interactions can be treated in a mean-field way, the Hamiltonian can be written as a sum on one-electron operators.

$$h(\mathbf{r_i})\psi_a(\mathbf{r_i}) = \epsilon_a \psi_a(\mathbf{r_i}) \tag{2.67}$$

As seen in the previous section, this means that for a system with two electrons a and b, one acceptable form of solution to this Schrödinger equation is a Hartree-Product. The great advantage of Kohn-Sham DFT is that both the density and the kinetic energy expression can be rewritten almost exactly in terms of the single-electron orbitals of a Slater determinant. First, it can be shown that the density of a system can be written in terms of the single-electron orbitals

$$n(\mathbf{r}) = 2 \sum_{i=1}^{N/2} |\psi_i(\mathbf{r})|^2 \tag{2.68}$$

The approximation this is making is known as the Kohn-Sham ansatz. It says that the exact density can be replaced by the density from a non-interacting electron system. Not only does this allow the density to be written as above, but also it gives a way of

calculating most of the kinetic energy.

$$\langle \Psi^{AE} | \frac{-\nabla^2}{2} | \Psi^{AE} \rangle \simeq \langle \Psi^{SD} | \frac{-\nabla^2}{2} | \Psi^{SD} \rangle = \sum_{i \ \epsilon \ \text{occ}}^{N} \langle \psi_i | \frac{-\nabla^2}{2} | \psi_i \rangle \tag{2.69}$$

It is assumed that a single Slater determinant gives a good approximation to the wave-function and hence that the kinetic energy of a single Slater determinant calculated using the non-interacting electron orbitals as shown above, gives a good approximation to the real kinetic energy. By making use of the density and the Slater determinant wave-function or non-interacting orbitals, it has been possible to get accurate expressions for almost all the quantities needed. It is important to note that a Slater determinant is not the only possible anti-symmetric wave-function and thus using it does not imply that DFT contains the exchange effects exactly. Neither is the approximation for the kinetic energy enabled by a Slater determinant, the exact kinetic energy. This and the other missing many body effects, are included via the exchange-correlation energy E_{xc} described in section 2.4.7.

2.4.5 Minimizing Kohn-Sham Energy

The final expression for the Kohn-Sham energy is:

$$E[n] = \sum_{i=1}^{N_{el}} \int \psi_i^*(\mathbf{r}) (\frac{-\nabla^2}{2}) \psi_i(\mathbf{r}) \mathrm{d}\mathbf{r} + E_J[n] + E_{\text{ext}}[n] + E_{xc}[n] \tag{2.70}$$

This expression needs to be minimized subject to the condition that the orbitals remain orthogonal, or equivalently that the density integrates to the correct number of electrons.

$$\Omega_{KS}[n] = E_{KS}[n] - 2 \sum_{i=1}^{N_{el}/2} \sum_{j=1}^{N_{el}/2} \epsilon_{ij} \left[\int \phi_i^*(\mathbf{r}) \phi_j(\mathbf{r}) \mathrm{d}\mathbf{r} - \delta_{ij} \right] \tag{2.71}$$

Minimizing each of these terms gives [37]:

$$H_{KS} \psi_j(\mathbf{r}) = \epsilon_j \psi_j(\mathbf{r}) \tag{2.72}$$

$$H_{KS} = \left[\frac{-\nabla^2}{2} + V_{KS}(\mathbf{r}) \right] \tag{2.73}$$

$$V_{KS}(\mathbf{r}) = \int \frac{n(\mathbf{r}')}{|\mathbf{r} - \mathbf{r}'|} \mathrm{d}\mathbf{r} + V_{\text{ext}}(\mathbf{r}) + V_{xc}(\mathbf{r}) \tag{2.74}$$

So this energy expression, when minimized, produces another Schrödinger like equation. This time however it uses single-electron, instead of many-electron, wave-functions. The following sections will discuss how to solve this computationally to and produce accurate ground state energies.

2.4.6 Self-Consistency Using Single-Electron Orbitals

The equations resulting from the minimization of the energy are another set of single-particle Schrödinger equations. These define the single-electron orbitals which correspond to the minimum energy for the potential used in the energy expression above. Finding these orbitals is a simple matter of expressing them in terms of a basis and then diagonalizing the Hamiltonian, or more often in practice using a conjugate gradient energy minimization, to find the eigenvectors. This can be done for example by using a set of atomic centred functions as in the Hartree-Fock method or a linear combination of plane waves as is the case in some density functional codes. When the wave-function is represented in a basis, the Schrödinger equation above is turned from a set of linear equations into a matrix equation. To find the coefficients of the basis functions the Hamiltonian matrix must be diagonalized to give the eigenvectors and eigenvalues.

However, as the potential above depends on the electronic orbitals via the density, this is not the end of the process and these are not the ground state orbitals. Instead self-consistency between the orbitals and the density must be achieved. This is done by using the orbitals to build the new density that they correspond to via the equation:

$$n(\mathbf{r}) = 2\sum_{i=1}^{N/2} |\psi_i(\mathbf{r})|^2 \tag{2.75}$$

This density will be different to that initially input into the energy expression. A new input density is got by taking the output density and mixing it with the input density to create the density used in the next step. For example, a crude form of mixing scheme could be:

$$(\alpha - 1)n^0 + \alpha n^i = n^{\mathrm{New}} \tag{2.76}$$

Actual mixing schemes, such as Pulay mixing [41], are more complex and there are often special preconditioning schemes, such as Kerker preconditioning [42], to aid convergence. By scaling the contribution of each wave component by $\frac{k^2}{k_0^2+k^2}$ they are able to reduce the contribution from small wave-vectors and improve convergence of the conjugate gradient schemes. Eventually the densities will become self-consistent with the Kohn-Sham potential and the output density will correspond to the density created by the orbitals generated by the minimization.

2.4.7 Exchange Correlation Functionals

The exchange-correlation term $E_{\rm xc}$ is the energy contribution from the quantum effects not included in the Coulomb repulsion and (single-particle) kinetic energy. The exact form of this expression is unknown. For one system, the homogeneous electron gas, the exchange term can be calculated exactly. This is then used as the basis for the expression in other systems, via the local density approximation [37]

$$E_{xc}^{LDA}[n] = \int \mathrm{d}\mathbf{r} n(\mathbf{r}) \epsilon_{xc}^{\rm hom} n(\mathbf{r}) \tag{2.77}$$

For the homogeneous electron gas the exchange energy is given by.

$$\epsilon_x = \frac{-e^2}{4\pi\epsilon_0}\frac{3}{4}(\frac{3n}{\pi})^{1/3} \tag{2.78}$$

This enables the exchange-correlation potential, needed for the Kohn-Sham Hamiltonian, to be calculated by differentiation of E_{xc} with respect to the density. As the exchange energy scales as $\epsilon \sim n^{1/3}$, the potential is given in a local density approximation as:

$$V_{xc} = \left[\epsilon_{xc} + n\frac{\partial \epsilon_{xc}^{\rm hom}}{\partial n}\right] \tag{2.79}$$

$$V_x(\mathbf{r}) = \frac{4}{3}\epsilon_x^{\rm hom}(n(\mathbf{r})) \tag{2.80}$$

There is no exact expression for the correlation energy. An approximation is given by Wigner [37], but more often values are tabulated using results from exact quantum Monte Carlo simulations.

The first extension to the local density approximation, is to include some form of non-locality via the gradient of the density. This can improve the functional's performance greatly by helping to account for fast varying changes in the electron density not well described by the local density approximation.

$$E_{xc}^{GGA} = \int \mathrm{d}\mathbf{r} \epsilon_{xc}(n, |\nabla n|) \tag{2.81}$$

Semi-local approximations, such as PBE [43] and PW91 [44], have been particularly successful. However, further improvements can be made, although at additional computational cost. So called hybrid-functionals, aim to eliminate some of DFT's most significant problems, such as the self-interaction error. Initial schemes simply averaged the

Hartree-Fock exchange expressions and DFT exchange-correlation functionals. However, currently one of the most advanced commonly used work-horse functionals, is the B3LYP functional [45–47].

$$E_{\mathrm{xc}}^{B3LYP} = (1-a)E_x^S + aE_x^{HF} + bE_x^{B88} + cE_c^{LYP} + (1-c)E_c^{VWN} \tag{2.82}$$

These expressions are in effect taking portions of different functionals and mixing them together. The constants a, b, c are chosen in an empirical fashion, by altering them until the functional is able to most accurately reproduce the equilibrium bond lengths and formation energies of a defined test set of small molecules. With the ability to accurately reproduce these, the performance for larger more complicated systems is improved too. These functionals are usually more costly to implement however, as the exchange term will usually scale as N^4.

So far the exchange correlation functional has not considered the spin of the electrons. Electrons can be either spin-up or spin-down:

$$\sigma(\mathbf{r}) = n^{\uparrow}(\mathbf{r}) + n^{\downarrow}(\mathbf{r}) \tag{2.83}$$

The exchange correlation potential will then be different for the two spins. This leads to a spin dependence for the single-electron wave-functions and Kohn-Sham orbital eigenvalues.

$$H^{\mathrm{KS}}\psi_i^{\sigma} = \epsilon_i^{\sigma}\psi_i^{\sigma} \tag{2.84}$$

2.4.8 Calculating Forces

It has been described how DFT is used to find the ground state energy and density of a system of atoms. Once this has been found, the forces on the atoms can be calculated and the minimum energy geometry of the system found by progressive minimization. Calculation of forces is done formally via the expression

$$\mathbf{F} = -\nabla_{\mathbf{R}} E(\mathbf{R}) \tag{2.85}$$

The energy of the system is the expectation value of the Hamiltonian. The coordinates of the nuclei are parameters in the energy expression and so the Hellman-Feynman theorem can be used to calculate an expression for the force.

$$\frac{\partial E}{\partial R} = \langle\psi|\frac{\partial \hat{H}}{\partial R}|\psi\rangle \tag{2.86}$$

This equation is only valid when the wave-function is an exact eigenstate of the Hamiltonian. If the basis functions are dependent on the atomic positions, then there will be additional terms from the Pulay forces [48]

2.4.9 Stresses and Strains

As will be seen in section 2.5.3, when simulating a system the concept of the unit cell of a periodic system is often employed. The unit cell is defined by the vectors $\mathbf{a_1}, \mathbf{a_2}, \mathbf{a_3}$ and is periodically repeated to construct the full system. Consider a strain on the system $\mathbf{a_i} \rightarrow \mathbf{a'_i}$, where $\mathbf{a'_i} = \mathbf{a_i} + \sum_\beta \epsilon_{\alpha,\beta}\mathbf{a}_{\mathbf{i},\beta}$. Here, $\epsilon_{\alpha,\beta}$ is a 3×3 matrix called the strain tensor. Anti-symmetries in this matrix would simply correspond to rotations, therefore it assumed to be symmetric. The positions of atoms in the strained cell are shifted to

$$\mathbf{R}'_{\mathbf{i},\alpha} = \mathbf{R}_{\mathbf{i},\alpha} + \sum_\beta \epsilon_{\alpha,\beta} R_{i,\beta} \tag{2.87}$$

and the stress tensor is given by

$$\sigma_{\alpha,\beta} = \frac{\partial E_{Tot}}{\partial \epsilon_{\alpha,\beta}} \tag{2.88}$$

The system being simulated is only in complete equilibrium when the forces on all atoms inside the cell are zero *and* when all components of the stress on the unit cell vectors are zero. Therefore, the unit cell vectors must be altered in conjunction with the atomic positions until this is the case and $\sigma_{\alpha,\beta} = 0$.

2.5 Basis Sets

To solve the single-particle Kohn-Sham equations, the single-electron wave-functions must be expanded in terms of a basis. This transforms the series of integro differential single-particle Schrödinger equations, into a matrix equation which can be solved computationally in an efficient fashion.

2.5.1 Atomic Orbitals

Atomic orbital basis sets offer a simple intuitive way to solve the equations of DFT. They are usually derived from solutions to Schrödinger equation for an isolated atom. The radial solution gives functions of the form

$$R(r) = e^{-r/na_0} r^l L_n \tag{2.89}$$

where L_n are the Laguerre polynomials. These functions can be used somewhat directly in the form of Slater orbitals. Often however, Gaussian orbitals are used to facilitate computation of integrals. As the product of a Gaussian is a Gaussian, four-centre integrals reduce to just two-centre integrals. These functions differ depending on the angular momentum channel l. They are multiplied by the spherical harmonics, $Y_{l,m_l}(\theta, \phi)$.

2.5.2 Plane Waves

The Kohn-Sham wave-functions can also be represented as a linear combination of plane waves.

$$\psi_{n,\mathbf{k}} = \frac{1}{\Omega} \sum_{\mathbf{G}} c_{\mathbf{G},n,\mathbf{k}} e^{i\mathbf{G}.\mathbf{r}} \tag{2.90}$$

Plane waves have been a success for a number of reasons. They are not biased by the form of the system or the types of atom within it. They enable the use of fast Fourier transforms, to move between real space and k-space, making some operations much faster. In addition they allow calculation of the forces to be done straight-forwardly. As the plane waves do not depend of the position of the atoms, the Hellman Feynman theorem can be used to calculate the forces directly. The use of plane waves is motivated by the Drude-Sommerfield model. This shows that electrons in a system without ionic cores, will have plane waves as their eigenfunctions. That is, plane waves are eigenfunctions of the homogeneous electron gas. Therefore, the real wave-functions produced when including the effect of the cores, should be somewhat similar to plane waves, as in the nearly free electron model. The difference is taken into account by building up the wave-function from many different plane waves using Fourier analysis.

2.5.3 Periodicity

Simulating an isolated system containing few atoms is straightforward. But often it is required to simulate a bulk solid material, which would require a great many atoms. However, this can be avoided by simulating a unit-cell of the solid and periodically repeating this in all 3 spatial dimensions. Surfaces can be simulated in a similar way, by leaving a vacuum gap in one of the dimensions. By leaving vacuum gaps in all 3 dimensions, an infinite set of isolated systems is in effect being simulated. As well as enabling the simulation of bulk solids and surfaces, periodic boundaries also have

some computational benefits. When a periodic system is being treated, Bloch's theorem can be applied. This states that the eigenfunctions of the Schrödinger equation with a periodic potential can be written as

$$\psi_{n,\mathbf{k}} = u_{n,\mathbf{k}} e^{i\mathbf{k}.\mathbf{r}} \tag{2.91}$$

where $u_{n,\mathbf{k}}$ has the periodicity of the underlying lattice. These are the eigenfunctions of the wave equation with a periodic potential. The Bloch function $u_{n,\mathbf{k}}$ is defined as having the period of the lattice. Therefore, like any periodic function, it can be expanded using a Fourier series of terms that are the reciprocal lattice vectors. For example, as a series of plane waves with wave-vectors $\mathbf{G}$ equal to the reciprocal lattice vectors of the periodic lattice.

$$u_{n,\mathbf{k}} = \sum_{\mathbf{G}} \tilde{u}_{\mathbf{G},n,\mathbf{k}} e^{i\mathbf{G}.\mathbf{r}} \tag{2.92}$$

There are of course an infinite number of reciprocal lattice vectors defined by an infinite lattice. However, the higher frequency components of this plane-wave expansion for the Bloch function, are less important due to their higher curvature. Therefore, to a good approximation the expansion can be truncated at a certain cut-off. Note, that this truncation is required and determined by the amount of processing power and memory available for the calculation. Thus only components with

$$|\mathbf{k} + \mathbf{G}|^2 \frac{\hbar^2}{2m_e} < E_{\mathrm{Cut}} \tag{2.93}$$

are included. The effect of the cut-off is to produce a less accurate wave-function and hence a higher energy of the system. Systems should be tested for convergence to ensure that the effects of the truncation are not affecting the conclusions drawn from the calculation. Putting the expansion for the periodic Bloch function into the Bloch theorem expression of equation 2.91, gives:

$$\psi_{n,\mathbf{k}} = \frac{1}{\Omega} \sum_{\mathbf{G}} c_{\mathbf{G},n,\mathbf{k}} e^{i\mathbf{G}.\mathbf{r}} \tag{2.94}$$

This expression is simply a linear combination of plane waves. The original wave-function which was spread over the infinite space of the periodic lattice has been transformed into a wave-function localized inside just one of the periodic cells. However,

this wave-function must be calculated at an infinite number of k-points. This need can be circumvented by imposing Born von Karmen boundary conditions.

$$\psi(\mathbf{r} + N_i\mathbf{a_i}) = \psi(\mathbf{r}) \tag{2.95}$$

And using Bloch's theorem 2.91

$$\psi(\mathbf{r} + N_i\mathbf{a_i}) = e^{(iN_i\mathbf{k_i}.\mathbf{a_i})}\psi(\mathbf{r}) \tag{2.96}$$

The only k-values for which this is true are those which give the argument of the exponential a value of $2n\pi$.

$$k_i = \frac{\mathrm{Integer_i}}{N_i}\mathbf{g_i} \tag{2.97}$$

Thus there are an infinite set of infinitely close together k-points, if the number of cells N_i considered in the calculation is infinite. However, the energy is a smooth function of the wave-vector $\mathbf{k}$ and the Bloch wave solutions are unique only up to a reciprocal lattice vector. Therefore they can be fully described using just their components in the first Brillouin zone and the wave-function can be approximated by the average of its value at a finite number of k-points within this. Sometimes it is enough to take the average of the two equivalent Gamma points $k = 0$, and $k = \frac{\pi}{a}$. This transformation from real space into k-space is in effect numerical sampling and greatly simplifies the plane-wave formalism. Care must be taken as k-point sampling is more complex and important when dealing with systems with highly curved Fermi-surfaces, such as a nearly metallic system, which will then require more k-points to sample accurately.

2.5.4 Pseudo-potentials

Near an atomic nucleus, the Coulomb potential becomes extremely strong. To balance this the kinetic energy of the wave-function must also become very large and consequently the wave-function oscillates a great many times and requires a huge number of Fourier components to be accurately represented. This problem is avoided by using a pseudo-potential. In most situations the core electrons do not play an important role in the bonding of an atom, as they are highly localized around the nucleus. Only the valence electrons are involved in bonding. It is therefore a good approximation to take the core electrons in any system to have the same distribution as they would in an isolated atom. That is, solutions of the radial Schrödinger equation multiplied by spherical

harmonics. The interaction between the core electrons and the valence electrons is then approximated by what is known as a pseudo-potential, rather than being treated exactly. It is also possible to treat this interaction exactly using the projector augmented wave method, as discussed in section 2.5.5. But first here, the pseudopotential approximation is discussed.

There are several advantages to the pseudo-potential approach. First, it results in less electrons needing to be considered by the calculation and thus reduces the computational cost, as there are less Kohn-Sham eigenstates and therefore fewer matrix elements to compute. Another advantage is that the core electrons constitute a large fraction of the total energy. This energy can now be used as the base-line in a calculation and so the energy minimization can be sensitive to the far smaller energy changes of the valence electrons. The second advantage is that the creations of a pseudo-potential that has the same effect on the valence electron wave-functions away from the core, but allows them to be smooth within the core region, results in a dramatic reduction in the number of plane waves needed to represent those wave-functions.

The main drawback of using a pseudo-potential in contrast to an all-electron method, is that it compromises the universality of the method. A pseudopotential must do its best to accurately reflect the interaction between core and valence electrons, in all the different possible environments into which an atom could be placed. In a bulk solid, as part of a molecule, when in a liquid and so forth. This is known as the transferability of the pseudopotential. In most cases it is not perfect and should be checked. Transferability is particularly hard to achieve when an atom has many different possible charge states and therefore different possible numbers of bands. Often the correct charge state will depend on the coordination of the atom, which changes according to the environment. Titanium and Manganese are notable examples of important elements that pseudo-potentials can have difficulty with.

There are various different kinds of pseudopotential. Norm-conserving pseudo potentials ensure that the charge within the cut-off region is equal to the charge of the core electrons. This ensures that the core region of the atom is not greatly effected by the surrounding environment and so aids transferability. There are ultra-soft pseudo potentials, which result in smoother Kohn-Sham wave-functions and thus require fewer

plane waves. Finally there is a method known as the projector augmented wave (PAW) method which will be used in some of the studies in this thesis. This method is outlined next.

2.5.5 The Projector Augmented Wave Method

The projector augmented wave method [49] is used extensively in the first half of the thesis. An outline of the basics is given here, but as always the details of implementation are more complicated, see for example [50]. The advantages of both localized basis sets and plane wave implementations have been described. The PAW method however, combines the advantages of both basis sets. The PAW method uses plane waves in the interstitial region between atoms and a localized basis close to the atoms. This means that the method has access to the full all-electron wave-function and consequently that it can be a more transferable method than a pure plane-wave implementation. As the PAW method contains all the electrons in the system, it has at least some variational freedom in the core region that enables it to produce more accurate results than a frozen core approximation. However, retaining the plane waves for most of the system helps keep the computational cost down and retains the attractiveness of a single convergence parameter, namely the plane wave cut-off. The PAW method also has the straight-forward force calculation of the plane wave pseudopotential method.

In the PAW method a search is made for a smooth wave-function that is related to the exact all-electron wave-function via a linear transformation:

$$|\psi_n\rangle = \tau|\tilde{\psi_n}\rangle \tag{2.98}$$

Here, $|\psi_n\rangle$ is the fast oscillating all-electron wave-function that is hard to represent, while $|\tilde{\psi_n}\rangle$ is the smooth pseudo-wave-function that can be easily built using plane waves. A transformation is searched for such that

$$\tau = 1 + \sum_R S_R \tag{2.99}$$

where the function S_R is defined in non-overlapping spheres centred around the atoms, that is, the core region. Within this region, a partial-wave basis $|\phi_i^R\rangle$ is constructed from solutions of the Schrödinger equation for an isolated atom. For each of these functions,

there is also a corresponding 'soft' partial wave $|\tilde{\phi}_i^R\rangle$. These are chosen to match at the edge of the region R. A form for the wave-function can be derived:

$$|\psi_n\rangle = |\tilde{\psi}_n\rangle + \sum_{R,i}(|\tilde{\phi}_i^R\rangle - |\phi_i^R\rangle)\langle\tilde{p}_i^R|\tilde{\psi}_i^R\rangle \tag{2.100}$$

Which gives the linear transform as

$$\tau = 1 + \sum_I(|\phi_I\rangle - |\tilde{\phi}_I\rangle)\langle\tilde{p_I}| \quad \text{where} \quad I = (R, n, l, m) \tag{2.101}$$

The transformation above is used to create a basis in which plane waves represent the wave-function between the atoms and local functions (projectors), derived from the plane waves, represent the wave-function close to the atoms. The PAW method currently provides one of the best mixes of transferable accuracy and speed in density functional calculations.

2.6 The DFT+U Method

2.6.1 A problem with semi-local DFT

The pseudo-potential approximation struggles in situations where the valence electron wave-functions do not contain a node, 2*p* noble metals and 3*d* transition metals for example. In these cases, the pseudo wave-functions are very similar to the all electron wave-functions and since these wave-functions are strongly localized in the core region, a large number of plane waves is required to represent them. In addition, due to the approximate nature of the exchange-correlation functional, DFT has some systematic failings. Although these do not often cause the ground state energy or geometry of a system to be hugely incorrect, they do often greatly change the spin state energetics. The problem in DFT arises from the self-interaction error introduced by the mean-field treatment of the Coulomb potential. This results in every electron in the system repelling not only all the other electrons, but also itself. This results in the charge density being overly delocalized across a system. In HF, the exact exchange cancels this. But in DFT E_{xc} is approximate and therefore some self-interaction error remains. In effect, the on-site repulsion is not accounted for accurately. Thus electrons are able to delocalize themselves across multiple atomic sites more easily. DFT is unable to reproduce the characteristics of a Mott insulator, for example. The main aim of DFT+U

method is to improve DFT's physical description of some systems, without increasing the computational cost too greatly.

2.6.2 A Basic Way to Correct

The most serious problem to correct is the lack of correlation between unpaired *d* and *f* electrons. A correction therefore needs to be added to these electrons. As the over delocalization of electrons is equivalent to the lack of an on-site Coulomb repulsion, inspiration is taken from the Hubbard model and an on-site term is added to the Hamiltonian to correct this. The Hubbard model is:

$$\mathcal{H} = T \sum_{<i,j>} \sum_{\sigma} c^{\dagger}_{i\sigma} c_{j\sigma} + U \sum_{i} n_{i\uparrow} n_{j\downarrow} \tag{2.102}$$

The first term is the hopping integral and the second is the on-site Coulomb repulsion. In effect T gives the chance of making a hop from one site to another and U mimics the screened Coulomb repulsion between electrons. The sum $\langle i, j \rangle$ is taken over just nearest neighbour lattice sites. $c_{i,\sigma}$ are the creation operators for putting an electron of spin σ into an electronic orbital at the i$^{\text{th}}$ lattice site (each orbital can hold two electrons). The sum is only over the *d*-electrons of the system, which are the only ones for which this correction is added. It is the U term, which localizes electrons, that is used to correct DFT. By including a term of this form in the Hamiltonian, an extra energetic penalty can be added to discourage electrons delocalizing across multiple atomic sites in the system. In addition a second term must be included which is essentially the mean-field interaction of DFT for the *d* electrons, put into a Hubbard-like form, to remove the double counting of the interaction.

$$E^{LDA+U}[n] = E^{LDA}[n] + E^{U}[n_i^{\sigma}] - E^{DC}[n_i^{\sigma}] \tag{2.103}$$

$$E^{LDA+U}[n] = E^{LDA}[n] + \frac{U}{2} \sum_{i \neq j} n_i n_j - U \frac{N(N-1)}{2} \tag{2.104}$$

$$\tag{2.105}$$

This expression can be differentiated [51] to give the eigenvalues of the orbitals.

$$\epsilon_i = \frac{\partial E^{LDA+U}}{\partial n_i} \tag{2.106}$$

$$= \epsilon_i^{LDA} + U \sum_{j \neq i} n_j - \frac{U(N-1)}{2} - \frac{UN}{2} \tag{2.107}$$

$$= \epsilon_i^{LDA} + U(N - n_i) - UN + \frac{U}{2} \quad (2.108)$$

$$= \epsilon_i^{LDA} + U(\frac{1}{2} - n_i) \quad (2.109)$$

where $N = \sum_i n_i$ has been used. Note that this expression does not yet include the exchange contribution. With this included, the double counting term is actually

$$E^{dc} = \frac{UN(N-1)}{2} - \frac{J}{2}(N^{\uparrow}(N^{\uparrow} - 1) + N^{\downarrow}(N^{\downarrow} - 1)) \quad (2.110)$$

However the DFT+U formulation used in this thesis, from Dudarev [52], is simplified such that only the difference $(U - J)$ is meaningful. Therefore the role of J is not discussed further.

The equations above show that the energy will be lowered if an orbital is less than half occupied, and raised if it is more than half occupied. This results in the less-than-half-occupied orbitals being favoured. As more-than-half-occupied orbitals would require electrons to have opposite spin, favouring less-than-half-occupied orbitals also results in higher magnetic moments in most cases. It often has the effect of opening up a gap at the Fermi level to give an insulator, where DFT has incorrectly predicted a metal. Another way to think of the correction is as follows; when an electron is delocalized across a system, it comes close to electrons on other atomic sites, and will have to adopt the opposite spin direction in order to occupy the same orbital as them. This results in the overall magnetic moment dropping. When electrons are localized to their own site, they all have their own orbital and so can all point in the same direction increasing the magnetic moment. Parallel magnetic moments are favoured as they give a symmetric spin wave-function. As the overall wave-function must be antisymmetric, this results in an antisymmetric spatial wave-function. For this wave-function the electrons are further apart on average and therefore, lower in energy. It is important to note that the parameter U must be fitted to ensure that the system matches certain experimental results, for its spin state energetics for example. Once a value for U has been found for one specific system, it can then also be used as a correction in similar situations with reasonable confidence. In particular it must be checked that the description of a system provided by the DFT+U method, is not overly sensitive on the parameter U. It should also be noted that the parameter U suitable for a given system, will vary with the particular implementation of DFT used.

There are many other ways to reduce the effects of the self-interaction error and improve the results given by DFT methods. Functionals that include portions of exact Hartree-Fock exchange will have reduced self-interaction errors. Similarly there are fully self-interaction corrected implementations of DFT, though these can be significantly more costly computationally. Another method, that will form part of the work in this thesis is constrained DFT. This method can force electrons within a system to localize in specific places. In all systems it is a case of picking the method that best provides a route to the answers sought about the system, for a manageable cost.

2.7 Theoretical STM Imaging

2.7.1 Electron Tunneling

The scanning tunneling microscope (STM) discussed in chapter 1, functions by applying a voltage, of $2-3$V in the case of the semi-conductor, or 50 meV in the case of a metal, across a tip and a sample surface separated by a small vacuum region. Electrons from the tip can quantum mechanically tunnel through this vacuum region into the sample, or vice versa, creating a current that can be measured. The tunneling probability depends exponentially on the separation between the tip and the sample and therefore this setup gives excellent topographic resolution. The main limitation of STM imaging is that it does not produce a map of either the atomic charge density, or of the height of the sample. Instead it gives a picture that is a combination of the structural and electronic properties of the sample. Consequently it is not always straight forward to identify the underlying structure from an experimental STM image. Theoretical methods which can model possible structures and then produce a simulated STM image to compare with experiment are desirable. Density functional calculations can be used to produce simulated STM images [27, 28]. This technique will be used extensively in the first half of the thesis and an understanding of it will be useful. First, an assumption is made that the tip and the sample can be treated as two weakly coupled systems. The total Hamiltonian is then:

$$\hat{H} = \hat{H}_1 + \hat{H}_2 + V = \hat{H}_0 + V \tag{2.111}$$

where $\hat{H}_0$ is the Hamiltonian of the two sub-systems and V is the perturbation that describes their coupling. Unless a tight binding model is used, where $\hat{H}_1$ and $\hat{H}_2$ are localized entirely on the surface or tip, then there is a problem. The kinetic energy term in this equation is effectively included twice.

2.7.2 Bardeen and the Transfer Hamiltonian

Instead the problem must be solved using two sets of states which are eigenfunctions of the isolated tip or sample. Each of these states only solves the Schrödinger equation in a certain area of space (the two could overlap). This means that between the two there is a surface along which we can take the potential to be zero, that is, a vacuum. Bardeen then proposed that:

$$M_{i,j} = \int \mathrm{d}\mathbf{r}\psi_i^*(\hat{H} - E_0)\psi_j \tag{2.112}$$

The rate of tunnelling can then be got using Fermi's golden rule

$$\Gamma_{i,j} = \frac{2\pi}{\hbar}|M_{i,j}|^2\delta(E_i - E_j) \tag{2.113}$$

In order to evaluate the actual $M_{i,j}$ Bardeen [53] used integration by parts to give:

$$M_{i,j} = \frac{\hbar}{2m_e}\int_S \mathrm{d}^2\mathbf{r}[\psi_i^*(\mathbf{r})\nabla\psi_j(\mathbf{r}) - \psi_i^*(\mathbf{r})\nabla\psi_j(\mathbf{r})] \tag{2.114}$$

S is a surface between the surface and the tip. In effect the DFT calculation generates the ψ_i and then integral is used to give the value of M.

2.7.3 Tersoff-Hamann

Tersoff and Hamann transformed the unwieldy equation above into a simpler expression that can be more readily calculated. They made some assumptions in the process which are as follows [54]: First that it is sensible to use perturbation theory to model the tip-sample interaction. Then that there is a region between the tip and the sample where the tip-sample potentials cancel and the potential becomes zero. Also that the main tip state is an s-state. Then the asymptotic form of the surface wave-function and the tip s-state can be used to perform the integration. Together these led to the expressions for the matrix element and tunneling current [55].

$$\rightarrow M_{i,j} = \frac{\hbar^2}{m_e}2\pi\Omega_{\mathrm{tip}}^{\frac{-1}{2}}\mathcal{R}e^{\kappa R}\psi_j(\mathbf{r_0}) \tag{2.115}$$

$$I = A\sum_{\text{sample states j}}|\psi_j(\mathbf{r_0})|^2 \tag{2.116}$$

where κ is the decay length of the tunneling electron, $\mathcal{R}$ is the radius of the s-state of the tip and Ω is its solid angle. The Tersoff-Hamann expression essentially states that the current is proportional to the local density of states in the sample. This is determined by the the presence of an atom and the electron charge distribution around it. Thus again it is emphasized that the image contains both topographic and electronic features.

Chapter 3

Haem on the Si(111):H Surface

3.1 Introduction

Chapter 1 described the importance and potential benefits of studying molecules on surfaces for use in surface science and nanotechnology. Porphyrin molecules and the silicon surface were highlighted as particularly important systems. In this chapter, a study of the functionalized iron porphyrin haem(b) on the hydrogen terminated Silicon (111) [Si(111):H] surface is performed in order to investigate and understand the interaction between molecule and surface, interpret how this may affect the molecules potential for different applications and provide guidance to experimental work currently being performed on this system.

3.1.1 Haem and Iron Porphyrins

The biological molecule haem(b) consists of an iron porphyrin with a number of side chains. Haem acts as an electron transfer co-factor in the respiratory protein cytochrome(c) [56]. It is also involved in regulating the release and uptake of oxygen from the bloodstream as part of the protein haemoglobin [22, 57]. The role played by the molecule in these important biological functions has led to much computational work being performed on haem, and iron porphyrins in general, partly to assess their potential for use in technological analogues of these systems [58–60]. The magnetic moment of the central atom and its complicated spin state energetics, have resulted in iron porphyrins being explored as potential switches or molecular memory devices [14, 61] as well as conducting nanowires [62, 63]. In turn, this resulted in the molecule's surface properties being characterized on a number of surfaces, such as Ag(111) [64] and

Au(111) [65].

In addition, recent experimental work has proposed decorating amyloid fibrils with haem molecules in the hope of creating a conducting nanostructure [66]. Whilst it was possible to decorate the fibrils with haem, it was found that the haem molecules are no longer able to support charge transport once attached. To further understand the electronic structure of the haem molecule while on a surface and to look for ways past this problem, it is desirable to carry out STM investigations of haem on a surface. Experimental collaborators have performed work that attempted to image haem on the Si(111):H surface. However, this has also proved difficult, as it has a high mobility when on a passivated surface such as Si(111):H [67].

3.1.2 The Si(111):H Surface

The Si(111):H surface is chosen in particular to facilitate experimental collaboration. It is inert and easy to handle experimentally, as the hydrogen layer prevents impurities from binding to the surface. It is also easy to prepare, only requiring the clean Si(111) surface to be immersed in a Hydrogen Fluoride solution, to provide the surface Hydrogen layer. Its relation to the much used Si(001) surface also makes it somewhat relevant. Si(111):H is also a good choice from a computational perspective as it has a simple (1×1) reconstruction, unlike the clean Si(111) surface which has a complicated (7×7) reconstruction that requires a large computational cell to capture.

Most importantly, the presence of the hydrogen layer also offers a way to tune the interaction with the surface, via the removal of individual hydrogen atoms from the surface allowing the haem to interact with the resulting dangling bond. A number of recent experimental works have shown that porphyrin and phthalocyanine molecules can be tethered to a passivated surface by creating defects in the surface's hydrogen layer [68, 69]. The dangling bond created by the removal of a hydrogen atom from a passivated surface, can form a bond with an atom of the porphyrin. This results in the molecule being pinned to the surface, which is potentially useful for a number of reasons. First, it could hold a molecule in place and facilitate STM imaging. Second, if a series of defects were created at desired positions using an STM tip, a pattern of porphyrins could be built up to suit a particular application, for example a nanoline. In

this chapter a density functional theory study of haem on the Si(111):H surface is performed, both to study the electronic structure of the molecule whilst it is on the surface and to investigate whether creating defects in the surface's hydrogen layer allows the molecule to be pinned in position.

3.2 Methods

3.2.1 Haem Molecule

Here the computational method used, calculation parameters and the degree of calculation convergence are discussed. The calculations in this chapter are performed using the plane-wave code VASP [70, 71], working with the projector augmented wave (PAW) method [49]. The calculations use a plane-wave cut-off of 325eV and a GGA-PW91 [44] exchange-correlation functional. A cell size of $23\text{Å}\times20\text{Å}\times38\text{Å}$, is used. This gives at a 16Å vacuum gap between the adsorbed haem and the next periodic slab image. The Brillouin zone is sampled at just the Gamma point, enabling a halving of the memory and doubling the speed of calculation for tolerable loss of accuracy in such a large cell. The electronic minimization procedure had a tolerance of 1×10^{-6} eV and the ionic force minimization a tolerance of 0.01 eVÅ^{-1}. The unpaired *d*-electrons of the iron atom in a haem or iron porphyrins molecule, often make DFT produce incorrect spin state energetics for these systems [58, 72]. As described in chapter 2, this can be partially remedied by using the DFT+U method [51, 73] which in VASP is implemented using the Dudarev formalism [52]. Calculations here illustrate the effect of the DFT+U method and then go on to use it in the rest of the calculations. The method was used with parameters $U = 4$eV and $J = 1$eV, which were found to be accurate for iron porphyrins in [58].

Convergence tests were carried out to ensure that calculations are performed accurately without using wastefully large parameters that would be a great hindrance in such a large (384 atom) system. As stated in chapter 2, one of the most important convergence parameters in a plane wave density functional code is the largest reciprocal lattice vector that is included in the expansion of the periodic Bloch wave-function, or equivalently the energy cut-off. In DFT, convergence of absolute energies is extremely slow, usually requiring a very high cut-off and many plane waves. However conver-

gence of energy differences is rapid. As this is the important factor in many studies, for example binding energies and such like, most calculations look to converge energy differences. Figure 3.1, shows a graph of the energy difference $\Delta E_{\mu=0,2}$ between the $\mu = 2\mu_B$ state and the $\mu = 0\mu_B$ state of the haem molecule. This is important to get accurate to ensure the correct state is identified as the ground state. $\Delta E_{\mu=0,2}$ was found to change by 30 meV between performing the calculation with 325 eV and 400 eV cut-offs. This is certainly enough to identify the correct ground state and sufficient for the purposes of the study here, which will investigate the broad features of the binding regime.

3.2.2 Silicon Surface

To model the Si(111):H surface, a 6-lattice-plane (1×1) reconstructed slab was used. The bottom two layers of silicon atoms were fixed in their bulk positions. Both the upper and lower surface were passivated with hydrogen. To study molecular adsorption onto the surface, the separation between the molecule and the next periodic slab image must be sufficiently large and as stated, this was at least 16Å. The change in energy with vacuum gap is plotted in figure 3.1 and shows that this is sufficiently converged. The surface was sampled at the gamma point. Again, while total energies are slow to converge, energy differences between a normal Si(111):H surface and one with a defect were found to be converged to within 30 meV of those from a $4 \times 4 \times 1$ k-point sampling calculation, which is sufficient to capture the broad adsorption features in this investigation.

Throughout, binding energies between the molecule and surface were calculated using the following formula, which equates a positive ΔE_{bind} with an attractive interaction.

$$\Delta E_{\mathrm{Bind}} = E_{\mathrm{IsolatedHaem}} + E_{\mathrm{CleanSurface}} - E_{\mathrm{Complex}} \tag{3.1}$$

When simulating a surface, it is important to ensure that the model used is able to accurately capture the structural relaxations of a real surface. Yet at the same time, it is beneficial to have the surface as thin as possible, as this reduces the number of atoms needed in the simulation dramatically. With the thin layer under consideration surface energies are converged to within 0.05 eV of a 12-lattice plane slab, which will

be sufficient for this investigation. As described in chapter 2, the creation of theoretical STM images is an important aspect of computational surface science. Here the program bSkan [27, 28] was used in the Tersoff-Hamann [54] approximation, with bias voltages of $\pm 1.5V$ to produce images of empty and filled states respectively. All images were produced using the OPENDX visualization program, at WWW.OPENDX.ORG.

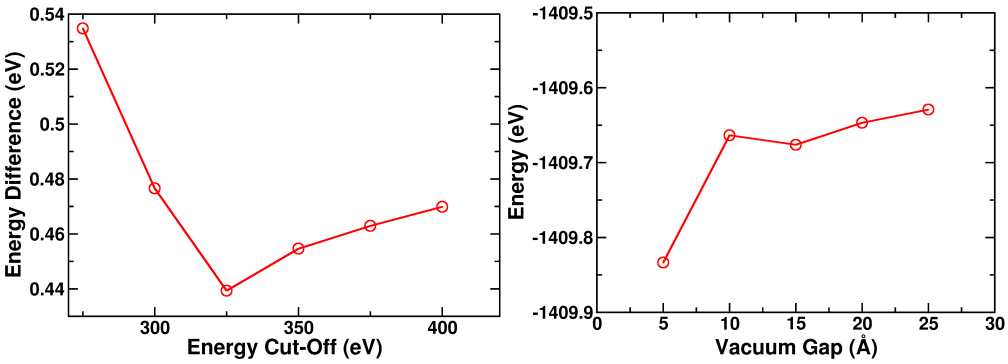

Figure 3.1: Left: Change in the energy difference between haem states $\mu = 2\mu_B$ and $\mu = 0\mu_B$, with plane wave cut-off. Right: Change in the total energy with vacuum gap, of the Si(111):H surface.

3.3 Results

3.3.1 Isolated Haem

Before adsorbing the haem onto the surface, an accurate gas phase structure for the molecule must be produced. This can then be used to correctly simulate how a gas phase molecule will act when approaching the substrate. The equilibrium structure produced by a gas phase DFT+U calculation is shown in figure 3.2. The central ring of the haem remains planar, kept so by the de-localized π-electrons, while the oxygen legs tilt slightly out of plane. Even if initially displaced, the iron atom relaxed back into the plane of the porphyrin. The Fe-N bond length was 2.01Å, in agreement with a previous study using the DFT+U method and this exchange-correlation functional [60]. This gives confidence that the geometric features of the haem are not adversely affected by the smaller cut-off chosen to facilitate the larger on-surface simulations later. The haem molecule was found to have a magnetic moment of $2\mu_B$, which arises from two unpaired electrons in the *d*-orbitals. Figure 3.2 shows that the spin distribution is cen-

tred on the central iron atom. This again agrees with calculations on iron-porphyrins performed using semi-local DFT functionals (PW91 and PBE) in [60]. This is expected as the iron atom in haem is still 4-fold coordinated. Changes in the magnetic moment usually only arise through the coordination of extra ligands to the central metal atom.

When considering binding of the haem to the surface, the orbitals closest to the Fermi level will play the most important role. These are plotted in figure 3.3. They are conjugated across the molecule with a component also on the central iron atom. The central atom appears to have d_{yz} and d_{xz} orbitals. None of the orbitals in figure 3.3 contain the d_{z^2}, which has a large out of plane component and is therefore most likely to be able to interact with the surface below. In some porphyrins this orbital has been found to be close to the Fermi energy [72] and therefore likely to interact with the surface.

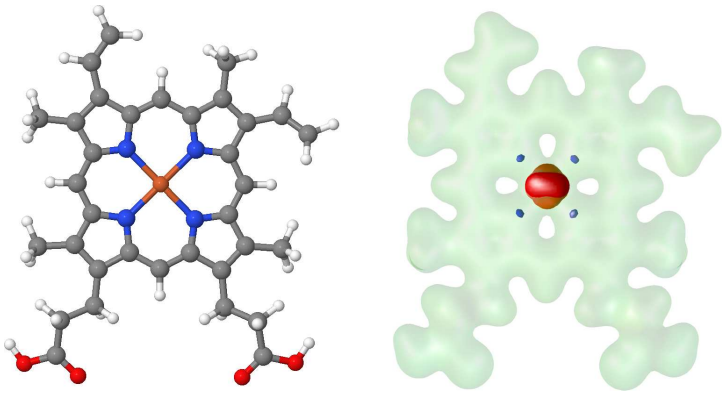

Figure 3.2: Left: Equilibrium structure of isolated haem molecule. Right: Charge (green) and spin (red=up, blue=down) isosurfaces. All isosurfaces are plotted at 0.01 e^- $Å^{-3}$ and use the DFT+U method.

Density of states plots for both the DFT+U and conventional DFT methods are shown in figure 3.4. There is a clear shifting of the occupied *d*-orbitals to a lower energy and of the un-occupied to a higher energy, when using the DFT+U method. This phenomenon was explained in chapter 2 and follows from the expression for the energy eigenvalue in a DFT+U method

$$\epsilon_i = \epsilon_{GGA} + U(\frac{1}{2} - n_i) \tag{3.2}$$

The main effect of this is to change the minority spin component from a metallic distri-

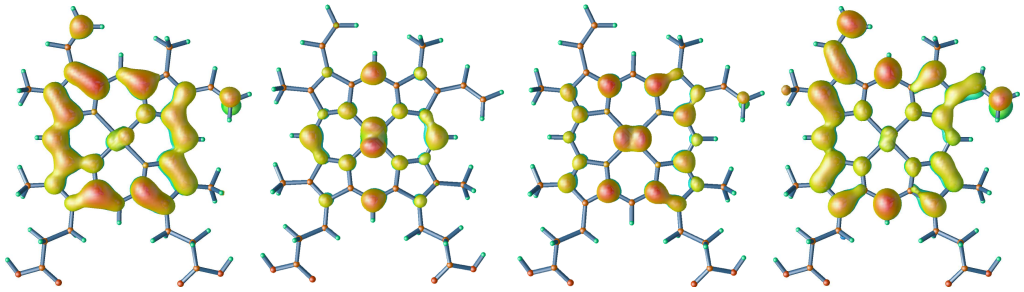

Figure 3.3: From left to right, the HOMO-1, HOMO, LUMO and LUMO+1 orbitals for the haem molecule simulated with the DFT+U method. Isosurfaces are plotted at 0.01 e^{-} $Å^{-3}$.

bution to a gapped one. Although the density of states changes significantly, both the magnetic moment of the system and the geometry remain relatively un-affected.

The gas phase structure and properties of the haem molecule have been thoroughly characterized. Haem was found to be similar both structurally and magnetically to an un-ligated iron porphyrin studied by other groups. The effect of the DFT+U method was investigated and found to produce marked changes in the density of states; though in this case conventional DFT produces the correct magnetic moment of the ground state as well. Previous work has looked at the effect of the DFT+U correction in more detail, and ascertained that it better reproduces the ordering of spin orbitals observed in experiments on iron porphyrins [58, 72]. Therefore the DFT+U method will be used for the remainder of the chapter.

3.3.2 Perfect H Surface

Next the adsorption of the haem molecule upon the surface is investigated. There have been a number of studies of similar porphyrin based molecules on surfaces, for example [64, 65]. These find the molecule to be adsorbed in a planar geometry, particularly when in isolation as opposed to high coverages. The haem was therefore adsorbed on the surface in a planar manner as shown in figure 3.5, with the iron atom in turn centred over each the three different adsorption sites shown in figure 3.6. The binding energies are shown in the table 3.1. The largest is 0.424 eV with the haem centred over a surface hydrogen atom, site A. The haem was then adsorbed in a standing configuration as shown in figure 3.6. This time was haem was found to have a binding energy 0.114

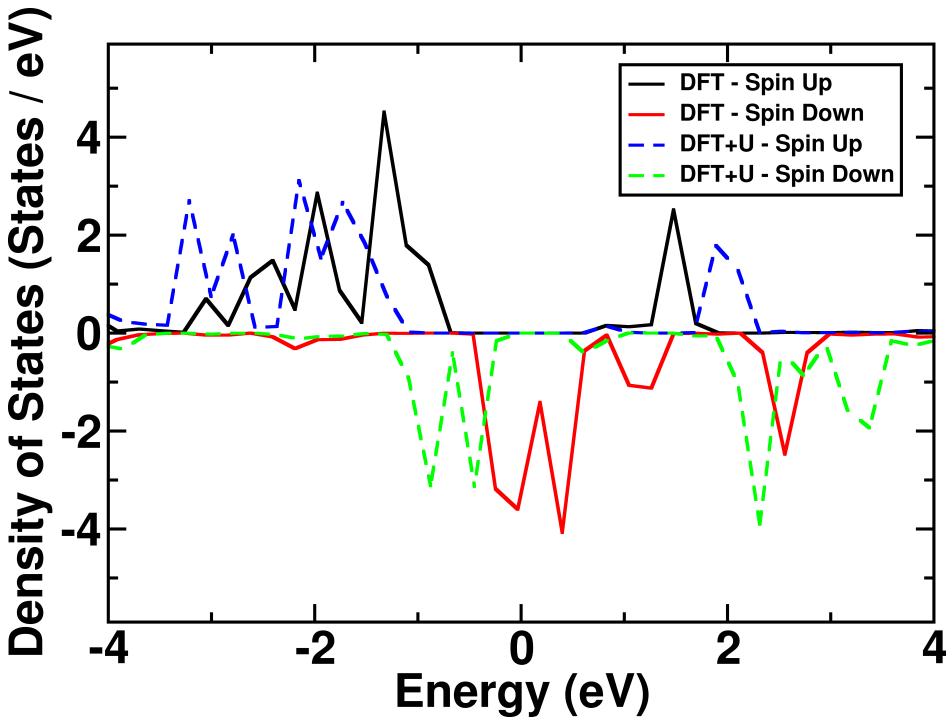

Figure 3.4: Density of states for the *d*-orbitals of the isolated haem molecule, shown for DFT and DFT+U simulations. The DFT+U method is clearly seen to shift the filled / empty states down / up in energy. In the DFT+U case the presence of 4 occupied spin-up orbitals and 2 occupied spin-down orbitals, can be seen clearly. These give the molecule its overall $\mu = 2\mu_B$ magnetic moment.

eV. By tilting the haem towards the surface by an angle of $45°$, the binding energy could be increased to 0.159 eV. This indicates that when the haem does not prefer to bind in a standing configuration. When it approaches the surface it should collapse into a planar adsorption conformation. The situation may become more complex if there is a high coverage of molecules on the surface. Then, there may be some benefit to standing up cooperatively [74], or forming tilted stacking phases, as seen for copper phthalocyanines [23]. The experiments on haem performed by collaborators use low coverages and therefore the molecule is likely to be adsorbed flat in this case.

As stated, the strongest binding for planar adsorption was over site A (0.42 eV) with adsorption over sites B (0.32 eV) and C (0.36 eV) being slightly less well bound. The equilibrium distance from the plane of the porphyrin to the hydrogen plane of the surface was found to be 3.25Å for site A, which is consistent with a previous work

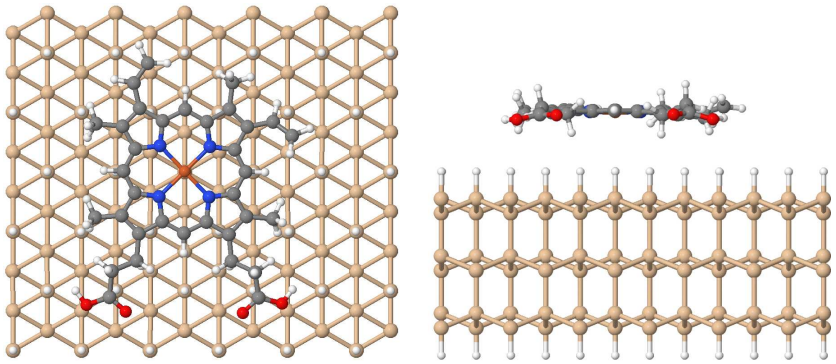

Figure 3.5: Here the planar adsorption configuration for haem on the Si(111):H surface is shown. Left: From above. Right: Side view

[65]. To ensure that the haem had not adsorbed to a poorly bound precursor, a binding curve was created and is shown in figure 3.7. To produce this, the iron atom was fixed at various heights above site A and all other atoms were allowed to relax. The graph shows that there is one shallow minimum at 3.25Å. The molecule was found to have rotational freedom on the surface. Rotations of 45° about an axis through the iron atom and perpendicular to the surface cost less than 10 meV. From this it appears that, even if it provides the majority of the binding energy, the C-N macrocycle of the porphyrin does not have a preferred site on the surface. Only the central iron atom has a site-specific interaction.

For all adsorption sites, the interaction between the molecule and the surface was minimal. The density of states and spin distribution around the molecule remained similar and still produced a magnetic moment of $2\mu_B$. These observations, together with the low binding energy, are indicative of a weak interaction between the molecule and surface with no covalent bonding component. This is the binding regime typically seen in these systems. DFT is not able to capture the dispersive van-der-Waals interactions thought to be important here [75]. The failure for dispersive interactions arises due to the absence of long range correlation in the exchange-correlation functional and there are a number of groups working on functionals to try and improve DFT's description of dispersive binding interactions [76, 77]. Nevertheless, as the haem repels the surface very strongly when pushed close, it is probable that the binding here is a different regime compared to the strong adsorption of aromatic molecules onto clean silicon sur-

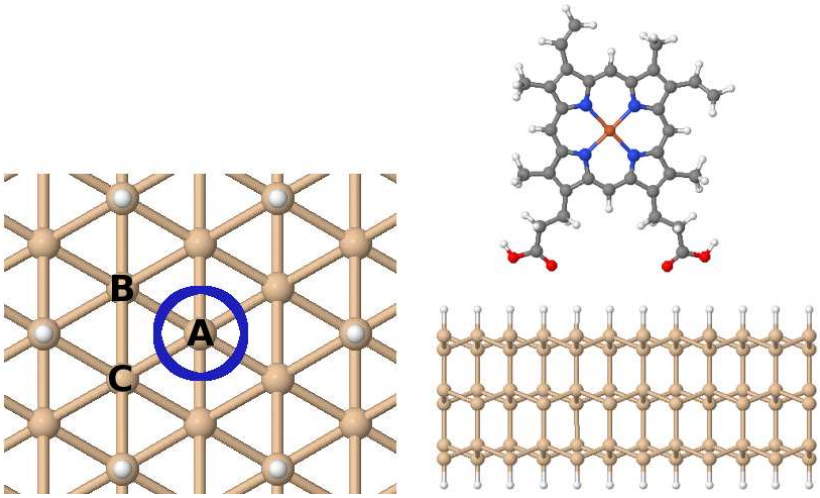

Figure 3.6: Left: There are three distinct surface sites. (B and C differ due to the differing depth of the underlying silicon atom. Site A has a hydrogen bound to the silicon atom.) In some simulations this hydrogen atom was removed as shown. Right: Simulations with the haem in a standing configuration were also performed.

faces, such as the adsorption of Benzene on Si(001) [78, 79]. One way to investigate the interaction with the surface is to look at the change in the haem molecule's charge distribution created by the nearby surface. A plot of the charge difference between the on-surface haem and an isolated haem at the same geometry, is shown in the left panel of figure 3.8. In this case there is little interaction and only the orbitals of the central metal atom are slightly perturbed.

As described in the methods chapter, collaboration between theory and experiment is extremely important in surface science. The principle tool for experimental investigation is the STM and so here, theoretical STM images are generated as described in the methods chapter, in order to guide future experimental work. Figure 3.9 shows simulated STM images of the haem on the Si(111):H surface taken at ± 1.5V. The images broadly reflect that shape of the isolated molecule's HOMO and LUMO. There is a noticeable symmetry change between filled and empty states, which mimics that between the HOMO and LUMO. The contrast of the image is constant around the carbon ring of the molecule, particularly in the case of the filled states. This indicates that the haem has maintained its $\pi-$conjugated charge distribution when on the surface; electrons are still de-localized around the molecule and not in definite double or single bonds. This

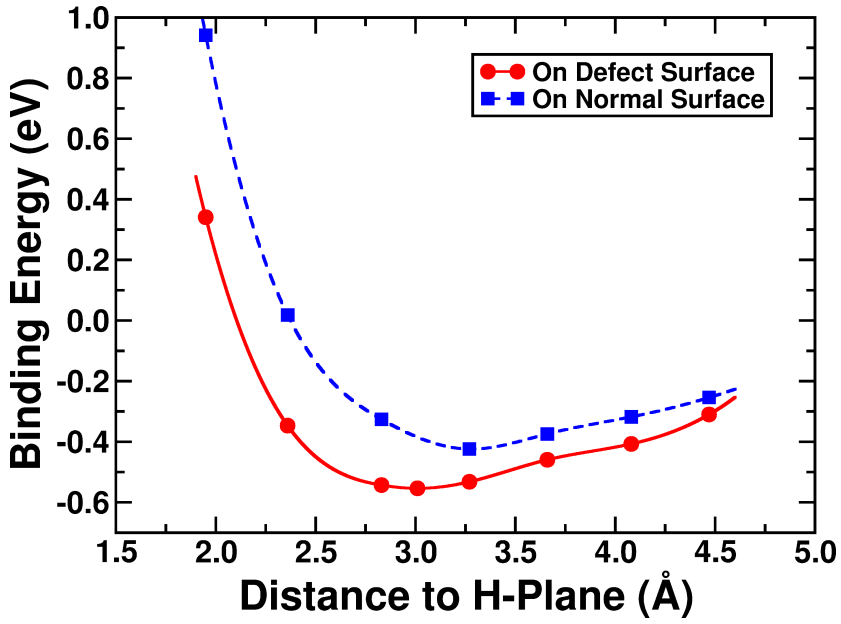

Figure 3.7: Graph showing the change in binding energy with height from surface for planar adsorption of haem on a perfect and defective Si(111):H surface. Line through points is a cubic spline intended only as a guide to the eye.

keeps the molecule planar while on the surface.

The results in this section show that the haem should be visible in STM experiments and distinguishable from the substrate. However, the weak binding with the surface results in the haem having a very high mobility and explains why recent attempts to image haem on Si(111):H have failed. As described in the introduction, some studies have been able to tether molecules to dangling bonds on a surface thereby holding the molecules in place. In the next section this phenomena is investigated theoretically. A hydrogen atom is removed from the Si(111):H surface and the change in interaction between the molecule and surface that this defect causes is investigated.

3.3.3 Defect Surface

The haem was adsorbed with the iron atom centred over the hydrogen defect above site A, shown in figure 3.6. The overall magnetic moment of the cell increased to $3\mu_B$ due to the polarization of the dangling bond beneath the iron atom. The binding energy was found to increase to 0.54eV and the molecule-substrate separation decreased by 0.25Å to 3.06Å. Again a binding energy curve was created, figure 3.7, by fixing the iron atom

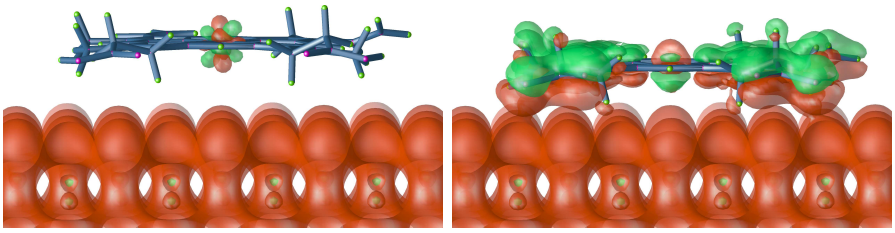

Figure 3.8: Charge difference plots for the perfect and defect surfaces. Left: Perfect Surface. Right: Defect Surface. Green indicates areas where the isolated haem had excess charge over the on-surface haem. Red indicates areas where the haem-surface complex has excess charge. Isosurfaces are 0.1 e^{-}Å^{3}.

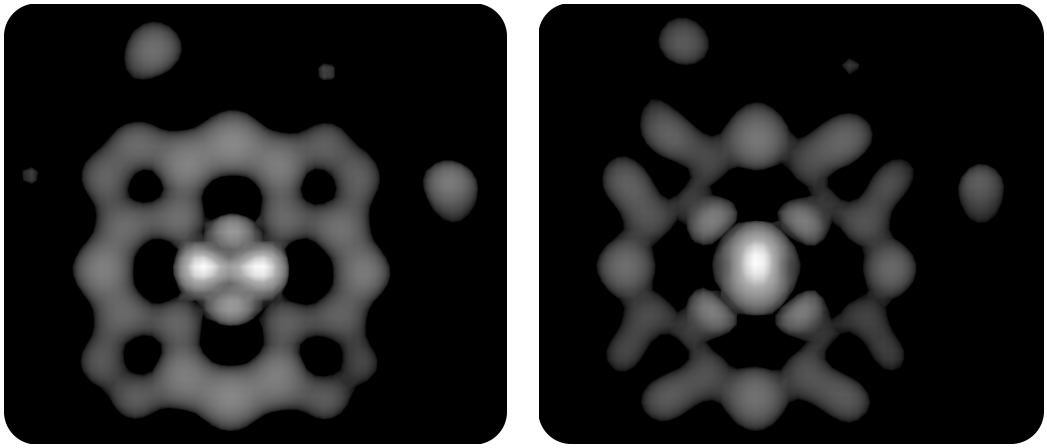

Figure 3.9: Simulated STM image of haem on the perfect Si(111):H surface. Bias voltage ± 1.5V. Left, filled states. Right, empty states. Isosurface of 0.003 e^{-} Å^{-3}.

at various heights and this exhibited another shallow energy profile with a minimum at 3.00Å. The removal of the hydrogen atom has allowed the molecule to move closer to the surface, but this has not dramatically increased the binding energy.

Previous experimental work has found that as well as the central metal atom, other parts of a phthalocyanine molecule can bind to dangling bonds on a silicon surface [80]. Specifically, the dangling bond was able to hybridize with the de-localized electrons of one of the benzene rings within a phthalocyanine. This tethered the molecule to the surface, but allowed it to pivot around the bond. Simulations were also performed with the defect centred under other haem atoms and beneath one of the 5 membered carbon-nitrogen rings (referred to as R centred). However, these were found to produce less strongly bound structures at larger separations from the surface. The results are

summarized in table 3.1. From this point on, the study concentrates on adsorption of the haem with the iron atom centred over the defect.

The important properties of a metaloporphyrin often originate from the electronic configuration and geometric coordination of the central metal atom [22]. When on the clean surface this was essentially unchanged from the gas phase case. While the interaction on the defect surface is still weak, the dangling bond of the surface does have some effect, First, via the hybridization of the $2p_z$ orbitals of the underlying silicon atom with the $3d_{r^2-z^2}$ of the iron atom. A similar phenomena was observed in, for example, Nitrogen atoms on Cu(100) surfaces [81]. The interaction between the molecule and the surface has changed the spin distribution around the central iron atom. This can be seen in figure 3.10, which also illustrates the polarization of the silicon's $2p_z$ dangling bond. Secondly, the surface has affected the charge distribution of the molecule. The effect of this is also evidenced by the charge difference plot of the right panel in figure 3.8. The defect has allowed the molecule to sink closer to the surface. However, the iron atom has had its charge pushed away from the dangling bond on the surface, evidenced by the red lobe above and green lobe below, the iron atom. The situation is reversed for the conjugated carbon ring of the molecule. The green charge distribution above the haem indicates that in isolation the molecule has more charge above its plane than when on the surface. The red charge below the plane indicates that the presence of the surface pulls charge of the molecule downwards. Both these points are further indication that the binding seen in these cases if due primarily to the carbon-nitrogen macro-cycle rather than a strong bond between the iron atom and the dangling bond. Again STM images were created of the molecule on the surface and these are shown in figure 3.11. The interaction with the dangling bond creates an observable change in the appearance of the central iron atom. The rest of the appearance remains broadly similar indicating that this change is not having a large effect on electronic structure of rest of the molecule.

The binding of haem to the Si(111):H surface can be increased by creating a defect in the surface hydrogen layer. This allows the haem to sink slightly closer to the surface when over this site. However, this causes only a negligible change in interaction. The haem remained far enough away to prevent strong covalent bonding between

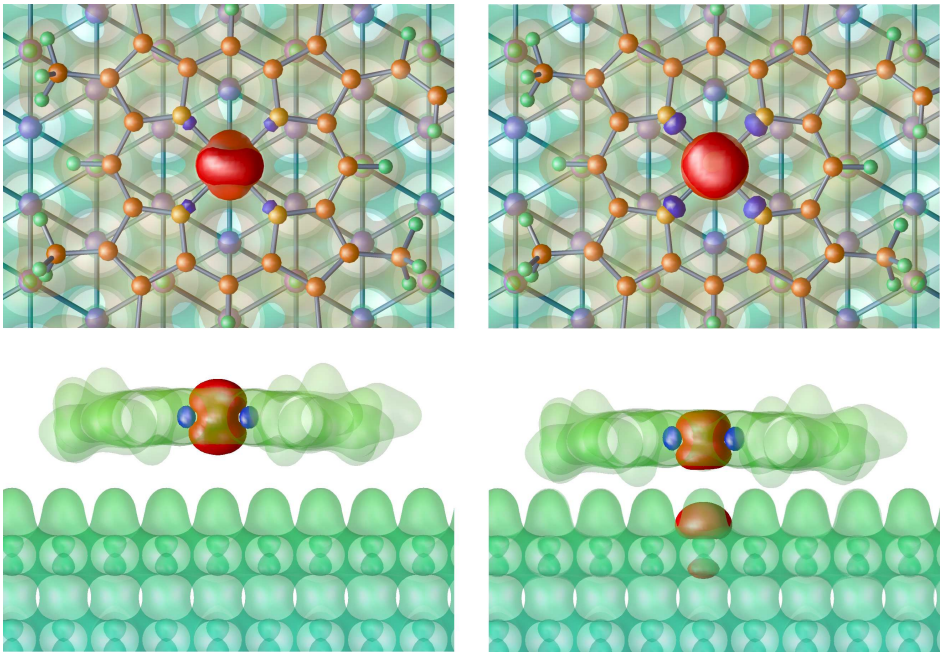

Figure 3.10: Left: Spin distribution for haem on the perfect Si(111):H surface. Right: For haem on defect Si(111):H surface. There is a clear difference in the spin distribution around the iron atom, although both have a magnetic moment of $2\mu_B$.

the iron atom and the underlying silicon and was still only weakly physisorbed. The iron atom, even when pushed down to meet the dangling bond, returned to the plane of the porphyrin ring. It is unclear whether the weak binding is due to the iron atom and silicon atom not being able to hybridize, or simply because the surface hydrogen atoms prevent the molecule getting close enough. These force the molecule to distort in an unfavourable way if it approaches too close to the surface. This would break the aromatic de-localized structure of the pi-electrons around the porphyrin ring, costing more energy than would be gained from the covalent bond. In the next section, the interaction of a SiH_3 complex with the haem molecule is investigated, in order to answer these questions.

3.3.4 SiH_3-Haem Complex

DFT+U simulations were performed on the SiH_3-[Haem] complex shown in figure 3.12. The silicon bound to the iron atom with an energy of 1.24eV and bond length 2.33Å. The iron atom was displaced out of the plane of the haem to check if this was a stable configuration, but it always relaxed back into the plane, regardless of the Si atom

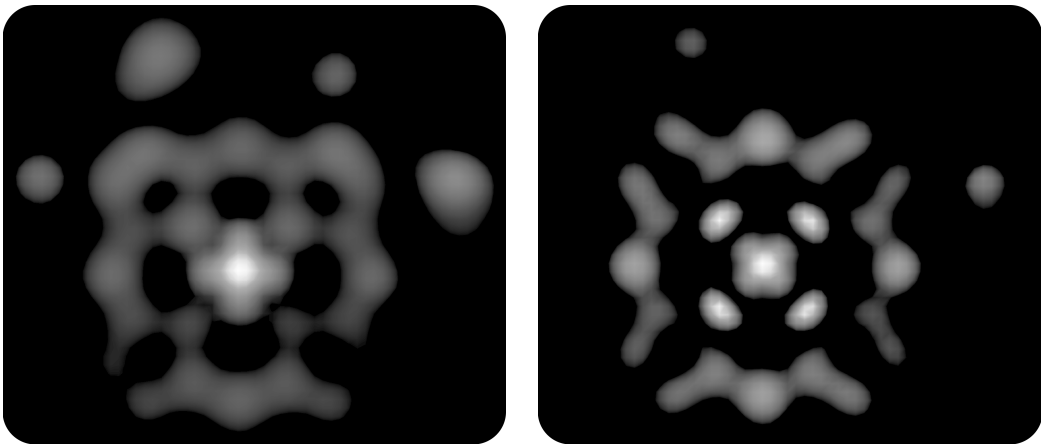

Figure 3.11: Simulated STM image of haem on the defective Si(111):H surface. Bias voltage ± 1.5V. Left filled states, right empty states. Isosurface of 0.002 e^{-} $Å^{-3}$.

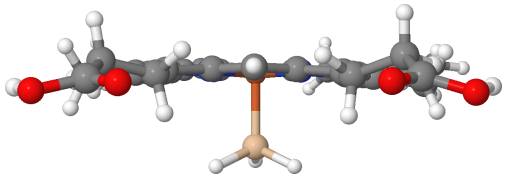

Figure 3.12: The optimized geometry for a SiH_3-[Haem] complex.

position. The magnetic moment of the total system was found to reduce to $1\mu_B$. Charge transfer from the silicon atom to the iron atom created an extra spin down occupation on the iron atom at -2eV as shown in the density of states figure 3.13. It is likely that when on the surface the iron atom did not get close enough for this hybridization to occur.

3.4 Conclusion

A density functional study of the iron porphyrin derivative haem(b) on the Si(111):H surface has been performed to investigate the effect of a surface on this molecules electronic structure and to provide guidance to current experimental work involving room temperature STM imaging of the molecule. This is done with a view to the potential technological applications of haem in areas such as molecular wires or nano-storage, akin to recent applications demonstrated for iron porphyrins.

The molecule was found to physisorb onto the Si(111):H surface with a binding energy of 0.42eV and minimal disturbance to its electronic structure. The molecule was

Table 3.1: Summary of results for the binding energies, magnetic moments and separations for different haem-substrate adsorption conformations.

Configuration		Separation[a]	Moment	Binding
Surface	Site	(Å)	(μ_B)	(eV)
Perfect	Site A	3.246	2.000	0.424
	Site B	3.504	2.000	0.317
	Site C	3.438	2.000	0.361
	Standing	8.679	2.000	0.114
	Tilted	8.421	2.000	0.159
Defect	Fe Centred	3.056	3.001	0.543
	N Centred	3.089	2.275	0.418
	C Centred	3.200	2.292	0.367
	R Centred	3.153	3.000	0.457

[a] Distance from the central iron atom to upper hydrogen plane of surface.

visible on the surface in simulated STM images. It was found that creating a defect in the hydrogen layer directly beneath the haem, increased its binding to the surface to 0.54eV and allowed it to move 0.25Å close to the surface. Although there was some electronic interaction between the surface dangling bond and the iron atom, no strong covalent bonding was observed. This was not the case for an SiH_3 molecule, which bound to the haem strongly. This indicates that the interaction of the silicon surface hydrogen atoms with the porphyrin macro-cycle is hindering the adsorption.

3.4.1 Future Directions

The removal of a hydrogen atom from the surface created a favourable binding site for the haem on the surface, which is useful for two reasons. First, it may be that this defect tethering can hold the molecule in position and enable room temperature STM imaging. Second, there is great potential for using these sites to create useful patterns of molecules. Using voltage pulses from an STM tip, Hydrogen atoms can be removed from specific sites of semi-conductor surfaces. This technique has been demonstrated for organic molecules on two silicon surfaces Si(111):H [80] and Si(001):H [69]. By

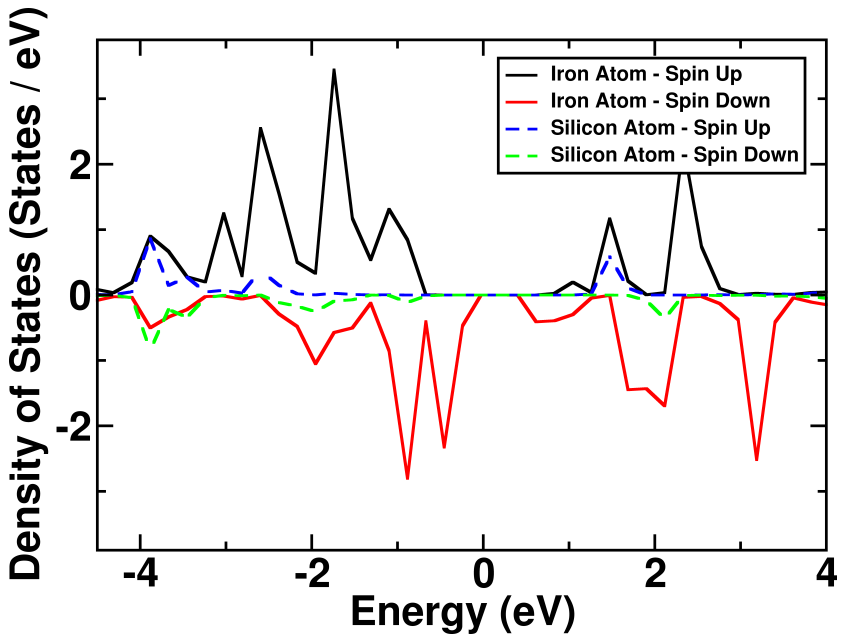

Figure 3.13: Density of states of the iron atom and the silicon atom for an SiH_3-[Haem] complex.

removing hydrogen atoms from the surface in a line for example, porphyrins can be adsorbed to the surface in long chains which may then act as a nanowire. A detailed look at the electron interaction between the orbitals of the iron atom and those of the dangling bond below would be useful. Higher accuracy quantum chemistry methods, performed using smaller sub-units of the surface and haem molecule, may be better suited to studying the exact spin state energetics in these systems.

3.4.2 Assembly techniques and Interaction Strengths

Creating patterns by removing hydrogen atoms from the surface and adsorbing molecules can be considered as part of a factory assembly paradigm. Molecules are chosen because in other situations, for example the gas phase or when in a bio-system, they are known to have the right desirable electron transfer properties. They are then encouraged to assemble into a useful structure such as a line. In the next section a different case is looked at. The formation of nanolines is found to occur spontaneously under certain conditions for some deposited materials. It is then a case of searching for ones which exhibit useful electronic properties when assembled. This is coming at the issue from a different direction. Lines of porphyrin molecules would be weakly bound,

made by active construction and possess similar properties to the gas phase. Deposited magnetic atoms would be strongly bound, be constructed via a growth process, with properties determined by the interaction with the surface.

Differing interaction strengths will also be contrasted. In this chapter there was only a weak physisorption interaction between the haem and the surface. This has the benefit of not disturbing the electronic structure, but of course makes assembly challenging. In the next two chapters, systems are adsorbed onto clean surfaces and much stronger chemisorption interactions are observed. These stronger interactions result in more interesting and complex reconstructions of the surface and adsorbate, and also alter the electronic structure more profoundly. This means that less information about the electronic properties of the on-surface system can be gleaned from the gas phase, but assembly should be more robust.

Chapter 4

Manganese on the Si(001) Surface

4.1 Introduction

4.1.1 Magnetic Atoms on Surfaces

Depositing magnetic atoms onto surfaces has been an area of active research for many years. More recently, these ideas have been applied to nanoscale systems, looking at the behaviour of individual and small groups of atoms on a surface [1]. These systems are interesting partly as they often exhibit novel physical phenomena that can shed light on the basic nature of many-body interactions. For example, the study of the force required to move an individual atom while on a surface [5]. However the main driver for research is the potential application of these system as nano-technological devices. In the field of spintronics [82], attempts are made to build systems which can perform computations or store information using not only the charge of an electron, but also its spin. This would allow many devices which currently do these tasks to be scaled down greatly in size. One of the most important steps towards a spintronic device is the creation of a spin polarized current. One potential method for producing this is to create a ferromagnetic semi-conductor [83]. This can be done by injecting magnetic atoms into a semi-conducting substrate, or by creating a magnetic thin film on top of its surface. The deposition of transition metal atoms onto the silicon surface is the subject of this chapter.

When atoms are adsorbed onto surfaces, potentially useful morphologies can form at sub-monolayer coverages. Some of the most studied are the various forms of nano-line. These are 1-dimensional structures on a surface and have the potential to operate

as wires or interconnects in nano-scale electronic devices [84]. Alternatively, magnetically coupled chains of atoms or spins could act as information or signal propagating systems [85]. Nanowires have been observed to grow in a number of different surface-adsorbate systems. Their primary advantage over other methods of nanostructure formation is that they are self-assembling. That is, they form during the growth process under specific conditions, rather than having to be assembled piece by piece. Although conditions must be carefully controlled, this is much more straightforward than assembling the structure atom by atom and could greatly facilitate them being produced in large numbers. However, to date there have been no wires found which have both desirable electronic properties and the ability to form in sufficient lengths and with sufficient ease via self-assembly. Some nanoline systems of note include the extremely long Bi lines which grow on Si(001) [86], while shorter nanolines have been observed in a number of other systems [84]. Functional lines may have to be isolated from the substrate to prevent current or signal travelling via the substrate. Therefore, the linear 1-D structures formed by atoms deposited on semi-conductor surfaces are of great interest also from the point of view of acting as a template for a more electronically useful structure to be built on top.

4.1.2 Manganese Atoms on the Silicon (001) Surface

In all of the areas outlined above, manganese atoms deposited on semi-conducting surfaces have been a particularly fruitful research area. While they have been the subject of studies on spin flipping and the Kondo effect [87], there has also been great interest in Mn atoms on the silicon surface for spintronic applications. Kratzer and Scheffler were able to demonstrate that a ferromagnetic layer of Mn atoms on the Si(001) surface would act as a half-metal [88]. This would be a possible way to build a spin injector to create a polarized current. Subsequently much work was performed, analysing the growth and morphology of Mn thin films on the Si(001) surface and the effect of subsurface atoms on these films [89, 90].

More recent experimental work has found that in addition to previously studied nano-structures, Mn atoms can form into nanolines of around 10-15 atoms in length when deposited on the Si(001) surface under certain conditions [91]. However, in this

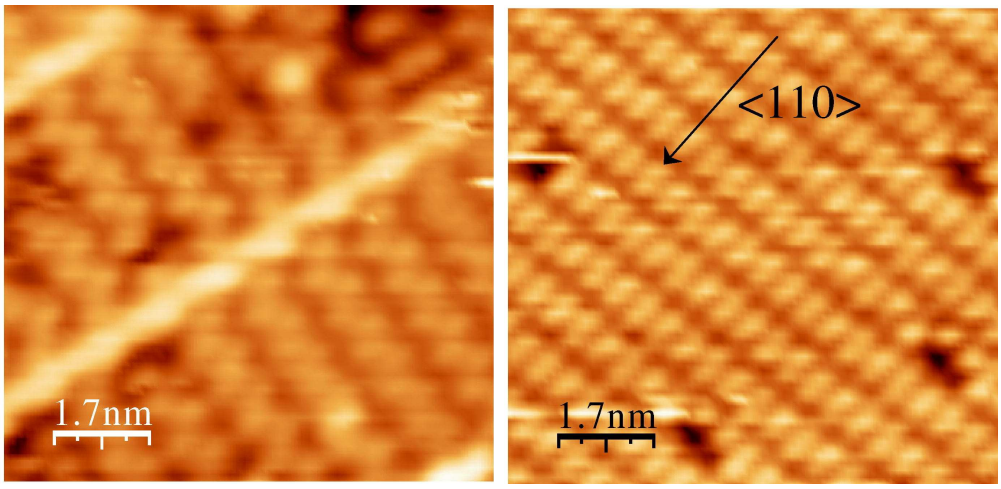

Figure 4.1: Left: Mn nanoline on the Si(001) surface. Right: Clean Si(001) surface. These STM images show unoccupied states at a bias of 3V and are reproduced from [91] with permission of Petra Reinke.

experimental work the exact structure of the lines was not entirely clear. In particular, the question of whether each bright sub-unit seen in the STM image, reproduced in figure 4.1, is made from one or more Mn atoms, or even Si atoms, is hard to answer. The electronic properties of the wire are also of great interest and have not yet been fully characterized. There are also open questions regarding the maximum length of the lines. 15 sub-units may be an upper limit, but perhaps defects or adjacent adsorbates could act to relieve strain and lengthen the lines, as in [92]. Performing numerous STM experiments to answer these questions can be very time intensive, and theoretical calculations offer a way to help identify the structure more rapidly. This is motivation for performing a computational study to ascertain the structure of the lines and explain the observed STM images and then to go on and look at the electronic and magnetic properties of the system. The lines seen in experiment ran perpendicular to the silicon dimer rows. They appear to consist of bright spots centred at a site between dimer rows, though the spots appear slightly smeared or elongated in the image, figure 4.1. When performing density functional calculations and building up a structure, attention will be paid both to the total energy and a structure's ability to reproduce the features of this image.

4.1.3 Outline of Chapter

First, the energetics of individual Mn atoms on the surface will be investigated and compared to previous works [93]. These sites will then be used as a basis for more complicated structures. Then, line-like structures will be created from Mn atoms placed on the surface. Simulated STM images will be created of the most energetically favorable line structures and compared to experimental images. Then the electronic and magnetic properties of the line thought most likely to be the observed structure will be investigated. Throughout, the effect of using the DFT+U method to study the system will also be studied, as in some Mn based compounds this can better reproduce the spin state energetics [65, 94]. The effect of the Coulomb screening on binding energies has not yet been investigated for the Mn nanoline system and its effect will be interesting to observe.

4.2 Methods

The methods used here are similar to those in chapter 3. Density functional calculations are performed using VASP with the projector augmented wave method. The manganese projector has been used in previous works such as [95, 96] where is was seen to reproduce experimental data accurately and can thus be considered suitable for use here. The smaller computational cell and lower number of atoms in this study enables some of the parameters to be run at more accurate levels. This will be important in this study as various structures are likely to have only small energetic differences. The plane wave cut-off is 400eV. The Si(001) surface was modelled using a 6-layer p(2$\times$2) reconstructed slab that contains 8 silicon dimers. The image of figure 4.1 appears to show the atomic lines cause the Si surface dimers in the vicinity to buckle into a p(2$\times$2) configuration as opposed to the c(4$\times$2) configuration. The size of the computational cell is $15.36 \times 15.36 \times 16.29$Å^3, which left at least an 8Å gap between the adsorbed atoms and the next periodic surface, sufficient to prevent interaction for these strongly adsorbed structures. The Brillouin zone is sampled using a $2 \times 2 \times 1$ Monkhorst-Pack k-point mesh.

Conventional DFT can successfully describe the electronic structure of many types of surface systems. However, as discussed in chapters 2 and 3, it can be less accurate in

some magnetic transition metal systems, due to its poor description of highly localized *d*-electrons. It is possible that when Mn atoms are at high coverages on the surface they may be highly coordinated and thus the effect of correcting the delocalized *d*-electrons may be important and interesting to investigate. DFT+U is for example, important for the highly coordinated Mn atoms in Mn Porphyrins, especially when these are ligated [65]. Therefore adsorption energies are also calculated using the DFT+U method.

4.3 Results

4.3.1 Isolated Mn Atoms on Si(001)

A common mode of nanoline growth is for atoms to aggregate around other atoms already adsorbed on the surface. A clean surface may have a well defined potential energy landscape that determines where adsorbed atoms will prefer to sit. However once the surface is decorated with adatoms, this landscape will change. To develop a candidate structure for the nanoline it is therefore important to consider the growth of nanolines as a process. In addition, line structures must have a greater binding energy per atom than individually adsorbed atoms on the surface. Otherwise, it would be preferable for atoms to adsorb at other locations on the surface, rather than joining the line structure.

The series of adsorption sites investigated is shown in figure 4.2. Where possible the nomenclature used is the same as that in [93]. The binding energy and magnetic moment for each site is given in table 4.1. Note that at this stage nothing is said about the direction of the magnetic moment. The calculations spins are simply being divided into up or down, not given specified directions. The results for the conventional DFT method have similar absolute and relative binding energies to those from [93]. The two sites D and D_{Sub} stand out as the most well bound. These are the replacement of a silicon dimer with a Mn atom and the placement of an Mn atom beneath a silicon dimer respectively. Of immediate relevance at the start of the growth process will be the most stable on-surface site, that does not involve removal of Silicon atoms from the surface, or diffusion to a subsurface site. The most stable such location is site H, with sites H' and M also being similarly well bound.

Binding energies using the DFT+U method are also shown in table 4.1. The rela-

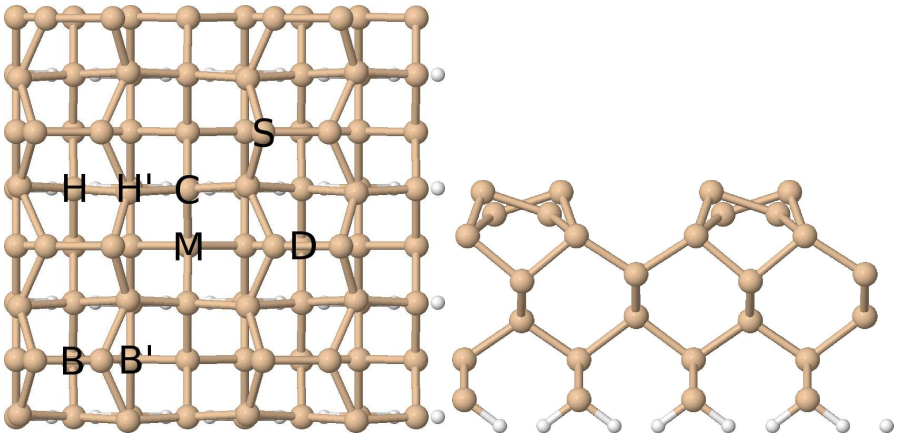

Figure 4.2: The adsorption sites investigated for isolated Mn atoms on Si(001) p(2×2).

tive stabilities of the sites are mostly unchanged although there is a trend for the relative binding energies of highly coordinated sites like site H and site D_{Sub} to change by a greater amount. The DFT+U correction may be more important when the surface has a greater coverage of Mn atoms as in this case Mn atoms may interact with each other. The only site with a dramatic relative change is site D_{Sub} which becomes markedly less well bound. When an atom reaches the sub-dimer site, it will cause the silicon dimer above to flatten [90]. This is because the Mn atom pulls in charge away from dimer in order to form a bond with it. This also results in the bond length of the dimer above increasing to a value greater than the buckled dimer bond length, going from 2.68Å to 2.73Å. When using the DFT+U method, the Mn *d* orbitals are contracted and so can interact less easily with the silicon atoms around and above them. This results in the reduced binding energy for this highly coordinated site when using this method.

4.3.2 Single Adsorption Site Lines

Having identified the most stable sites that are likely to be involved in the line structure, models for the observed lines are created using the experimental image as a guide. As a first step, lines consisting of just one adsorption site, repeated across the surface, are investigated. In figure 4.3, a number of these different single-site line structures are shown. Their binding energies and magnetic moments are shown in table 4.2. The energetic ordering of these lines is very similar to the isolated atoms of the previous section from which they are composed. In addition, there is very little change in the

binding energy per atom in each case. This indicates that the atoms in these lines are not interacting with each other. Once one of them has been deposited, there is no energetic benefit to another atom occupying the next site in the line, as opposed to a similar site elsewhere on the surface. There would therefore be no driving force for the formation of these morphologies. It is likely that the coverage of Mn on the surface needs to be increased to account for the propensity to form lines.

The only structure with a significant increase in binding is the line M structure, figure 4.3(a). The Mn atoms in this structure bind to the adjacent Si dimer atoms and cause the dimer to flatten out. This is a common occurrence when metal atoms bind to Si dimers [97, 98]. This flattening of dimers across the cell allows a small cooperative interaction between the Mn atoms. This will be born in mind when increasing the manganese coverage in the next section. Although it is a very poor candidate energetically, the structure of figure 4.3(b) is also important. It contains Mn atoms at site C the location of the bright spots of the experimental STM image. A simulated STM image of this structure is shown in figure 4.4 and indeed produces elongated bright spots predominantly in the trench between dimer rows. This indicates that the structures seen in

Table 4.1: The binding energies and magnetic moments of Mn atoms on the Si(001)-p(2×2) surface at various adsorption sites. The more positive the binding energy, the stronger the atom is bound to the surface.

	DFT		DFT+U		K&S [93]
Site	**m** (μ_B)	Δ E (eV)	**m** (μ_B)	Δ E (eV)	Δ E (eV)
H	1.00	2.72	3.00	1.88	2.91
H′	5.00	2.71	5.00	2.07	-
B	5.00	2.69	5.00	1.79	2.72
B′	5.00	2.38	5.00	2.03	-
M	5.00	2.65	5.00	1.84	2.63
C	3.00	1.76	5.00	1.23	-
S	3.00	2.59	3.00	1.66	2.86
D	3.00	3.74	5.00	3.21	4.29
D_{Sub}	3.00	3.70	3.00	1.58	3.80

experiment might be built around this site.

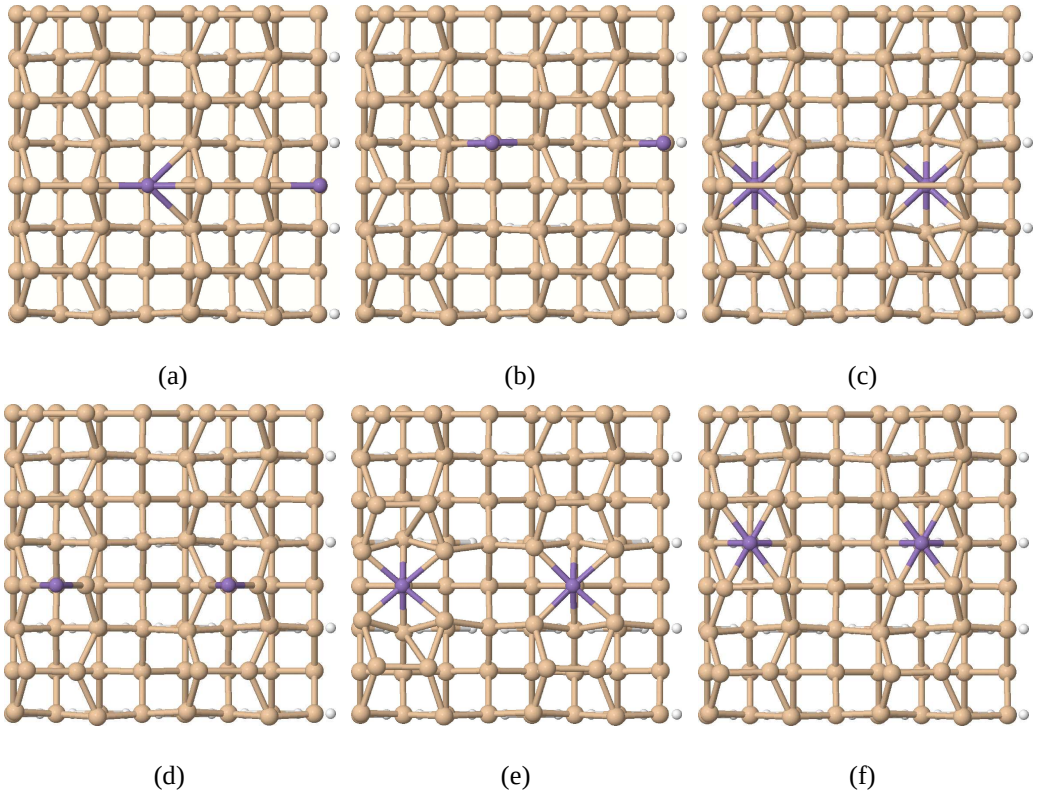

Figure 4.3: Atomic lines built from just one type of isolated atom adsorption site in each case.

Table 4.2: Binding energy *per Mn atom* and magnetic moment *total of cell* for a number of atomic line structures. Each line consists of Mn atoms at only one particular type of adsorption site. These are the structures shown in figure 4.3.

		DFT		DFT+U	
Site	Figure	$\Delta E\ (eV)$	**m** (μ_B)	$\Delta E\ (eV)$	**m** (μ_B)
LineM	4.3(a)	2.80	10.00	2.20	10.00
LineC	4.3(b)	1.76	8.00	1.31	10.00
$\text{LineD}_{\text{Sub}}$	4.3(c)	3.69	0.00	1.56	6.00
LineB	4.3(d)	2.43	10.00	1.81	10.00
LineD	4.3(e)	3.90	4.00	2.35	6.00
LineH	4.3(f)	2.85	6.00	1.87	6.00

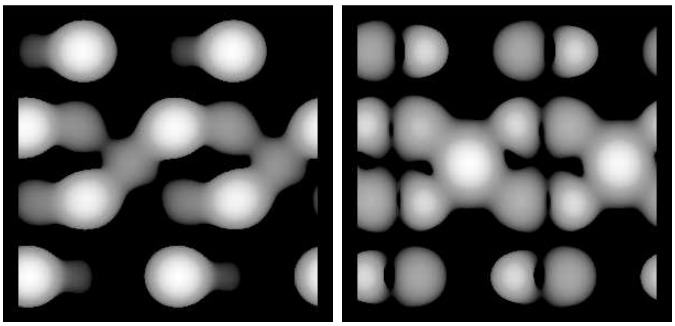

Figure 4.4: STM image of Structure 4.3 (b), a line of site C atoms, with binding energy 1.31 eV per Mn atom. Although not energetically very favorable, this structure produced an STM image similar to experimental ones. Images are for filled (left panel) and empty (right panel) states at $\pm$1.5V.

4.3.3 Many Adsorption Site Lines

Lines consisting of just one type of adsorption site possessed minimal interaction between the Mn atoms. This indicated that a higher coverage of Mn atoms is needed on the surface for there to be a cooperative driving force for line formation. One structure was found that produced a similar STM image to the experiments, while another structure showed at least a little cooperative behaviour. Using these two sites as inspiration structures consisting of Mn atoms at more than one type of binding site are studied. Where the structures in the last section had two Mn atoms per cell, the structures here have four, doubling the coverage of Mn. Three multi-site line structures are shown in figure 4.5 and their binding energies are given in table 4.3. These structures all have a greater binding energy *per Mn atom* than the single site structures of the previous section. This indicates that there is now some cooperative interaction between the atoms. Atoms will prefer to form these line structures, rather than adsorb on similar sites randomly over the surface; there is a driving force for line formation. However all three line structures are similar energetically, using both DFT and DFT+U methods. There is no clear indication of which structure is likely to be the experimentally observed nanoline.

To assess which line is the most likely structure, simulated STM images were created of all three multi-site line structures. The images produced by a line of site H and M atoms, shown in figure 4.6 is clearly not line-like and so this structure is

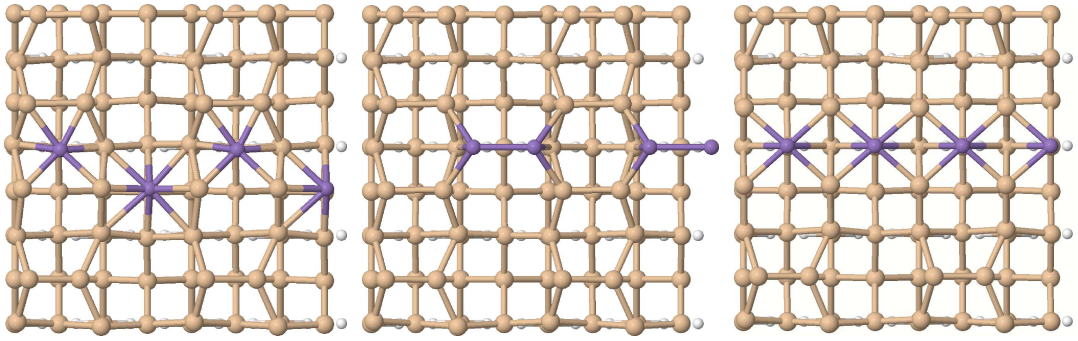

(a) (b) (c)

Figure 4.5: 'Multi-site' adsorption lines, consisting of atoms positioned on the most promising adsorption sites identified in the previous sections.

disregarded. Of the other two structures, the STM of LineH′2, shown in figure 4.8, is most akin to the elongated bright spot seen in experimental images. This structure is therefore proposed as being responsible for the experimentally observed image. It is also the most stable of the structures using the DFT+U method. This image is promising as it exhibits the elongated nature of the bright spot, by containing two atoms, but at the same time remains as one continuous bright spot in the image, similar to the experimental work. In particular, when imaged at $\pm$3V as in the lower panels of figure 4.8, a continuous bright line across the surface seen, with the contrast brightest in the trench between dimer rows, as in experiment.

As a final check on potential adsorption geometries, a DFT+U calculation was performed with the Mn atoms aligned parallel to the dimer rows as in figure 4.9. Although each Mn atom is still coordinated to two silicon surface dimer atoms, they no longer

Table 4.3: Binding energy *per Mn atom* and magnetic moment *total of cell* for three atomic line structures. This time the lines consist of Mn atoms at more than one type of adsorption site.

		DFT		DFT+U	
Site	Figure	$\Delta E\ (eV)$	**m** (μ_B)	$\Delta E\ (eV)$	**m** (μ_B)
LineHM	4.5(a)	3.11	12.00	2.00	16.00
LineH′2	4.5(b)	3.07	0.00	2.31	0.00
LineHC	4.5(c)	3.24	15.77	2.22	17.86

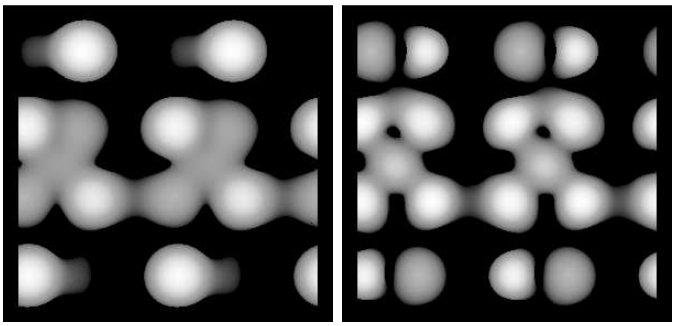

Figure 4.6: STM image of structure 4.5 (a) LineHM with binding energy 2.00 eV per Mn atom, using the DFT+U method. Images are for filled (left panel) and empty (right panel) states at $\pm$1.5V.

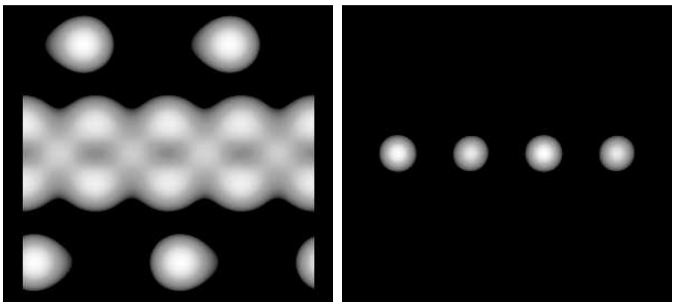

Figure 4.7: STM image of structure 4.5 (c) LineHC with binding energy 2.22 eV per Mn atom, using the DFT+U method. STM Images are for filled (left panel) and empty (right panel) states at $\pm$1.5V.

move towards each other to form Mn-Mn bonds. The binding energy of this structure is 2.02 eV per Mn atom, less than that for the proposed structure. The magnetic moment remained 0.00 indicating the atoms were still anti-ferromagnetically coupled. Along with the experimental image, this indicates that line formation parallel to dimer rows is less favourable than line formation across them.

4.3.4 Properties of Proposed Structure

The promising features identified in some single site lines are contained in the proposed structure. The flattening of the dimers, seen in the line of site M atoms, is also seen in the proposed structure. This allows some cooperative interaction between the manganese atoms across dimer rows, which remain uncovered. Again the mechanism for this flattening is common to many metal elements placed on the Si(001) surface. The

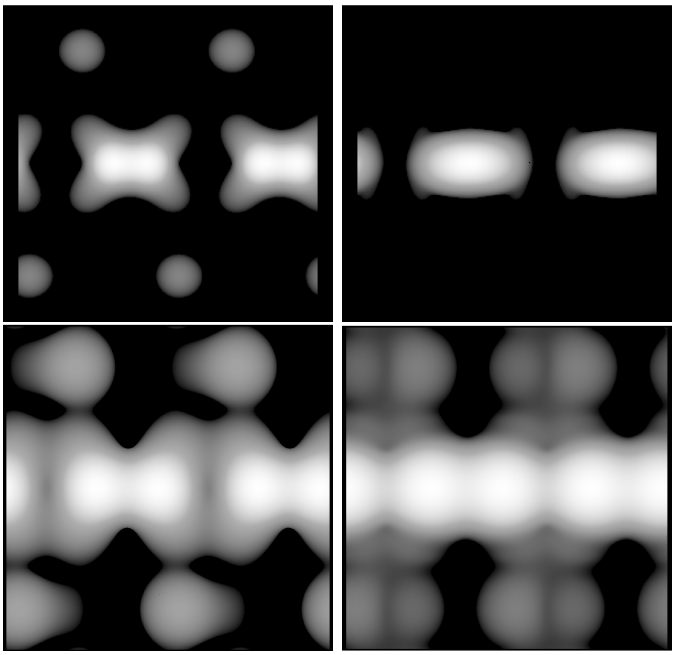

Figure 4.8: STM image of structure 4.5 (b) LineH′2 with binding energy 2.31 eV per Mn atom, using the DFT+U method. STM Images are for filled (left panels) and empty (right panels) states at $\pm$1.5V (top panels) and $\pm$3.0V (bottom panels).

metal pulls charge away from the atoms of the silicon dimer thus giving them equal charge and causing them to flatten. Their bond length also increases, indicating a decreased amount of charge. The placing of two Mn atoms at this location breaks that π bonding between 4 different Si dimers. This then affects the energy greatly.

Having seen increased coverage result in stronger binding, it is natural to consider adding further additional atoms to this line. Adding at site H is a potential way to complete the line, although there appear to be no bright spots in this position in the experimental STM images. DFT simulations found that atoms at these sites had no greater a binding energy than when at an isolated H site and there is therefore no reason for atoms to bind there specifically. Although it could be that the large number of Mn atoms in this small cell, is causing too much strain. Also tried were atoms at D_{Sub} in this line. This was not found to be energetically favourable. With the charge from the dimers already being taken by Mn atoms on the surface, there is not much easily available for atoms in the subsurface. Whilst more detailed modelling using larger unit cells is important, from the work here the candidate structure of figure 4.5(b) can be

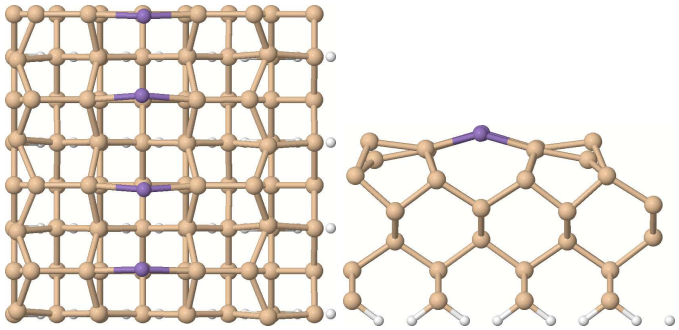

Figure 4.9: Structure of a line of Mn atoms grown parallel to the dimer rows. The binding energy was 2.01 eV per Mn atom, using the DFT+U method.

proposed with some confidence.

The electronic structure of the proposed nanoline structure is now outlined. One point of interest is the HOMO and LUMO of the structure. States within 0.5eV of the Fermi level are projected out and shown in figure 4.10. These reflect the nature of the occupied and unoccupied states STM images. The HOMO is predominantly located on the up-buckled silicon atoms of the un-flattened dimers away from the Mn atoms, as would be expected on the clean Si(001) surface. The LUMO is spread across the entire line complex having large lobes on the bond between the two Mn atoms in each sub-unit and also on the flattened silicon dimers. Projecting out states further from the Fermi level shows a more uniform charge distribution across the surface and wire atoms. It is hard to assess whether this type of distribution of homo-lumo states would facilitate signal transport through these structures. There is no clear conjugated pathway across the whole system due to the gap between the two atoms of a silicon dimer. However, the bridging Mn atoms do enable some link between dimer rows. The strength of the coupling between the two atoms is investigated next.

Spin active nanoline could have potential to act as information transfer or storage systems. The individual Mn atoms in the nanoline have magnetic moments of $4\mu_B$. This contrasts with the isolated Mn atom, which in a DFT calculation will have a magnetic moment of $5\mu_B$. However, each pair of Mn atoms in a sub-unit are coupled anti-ferromagnetically (AFM), which give the cell an overall moment of $0\mu_B$. When forcing the atoms in the line to ferromagnetically (FM) couple, the binding energy 0.19 less well bound. This is indicative of an exchange interaction between the two coupled

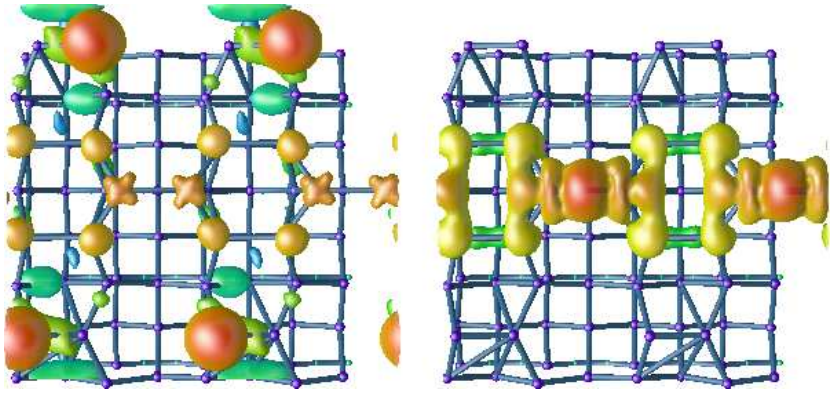

Figure 4.10: The HOMO and LUMO charge densities of the anitferromagnetic state of the line $H'2$ in figure 4.5 (b). They illustrate the presence of unoccupied states near the fermi level centred on the nanowire atoms. Simulations performed with the DFT+U method.

Mn atoms. Upon switching from AFM to FM alignment, the band gap decreases from 0.46 eV to 0.37 eV. The Mn atoms are also pushed away from each other by 0.57 Å, see figure 4.12 as the electrons are now of the same spin and therefore prefer not to occupy the same region of space.

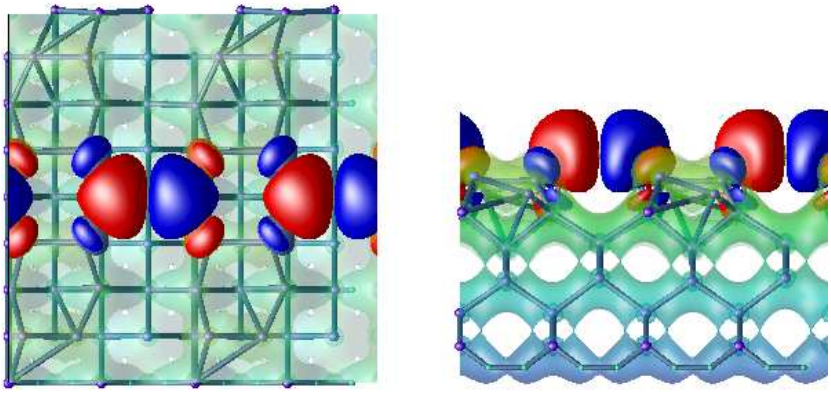

Figure 4.11: The spin distribution for the antiferromagnetic state of the structure of line $H'2$. Red = spin-up, blue = spin-down, green = charge isosurface. Simulations performed with the DFT+U method.

4.3.5 Non-Collinear Spin Calculations

One final aspect worthy of investigation, is the potential existence of non-collinear spin structures. In the previous calculations, spins have simply been divided into up and

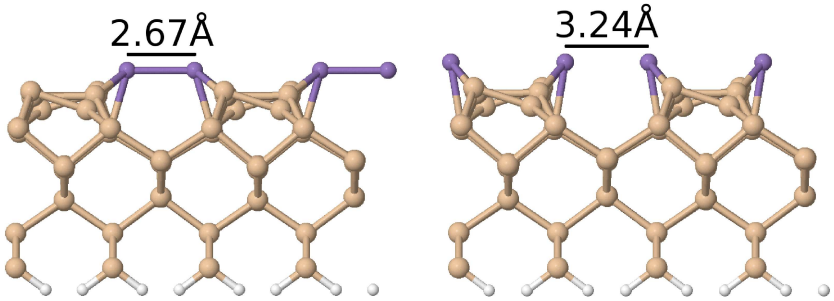

Figure 4.12: The structural change occurring when the line $H'2$ is switched from an anti-ferromagnetic state, to a ferromagnetic state. The bonded Mn atoms are pushed further apart by 0.57Å. Simulations performed with the DFT+U method.

down components, with no reference made to the direction of magnetic moment. Now spins are free to adopt a spatial direction and the magnetic moment projected along the x, y and z axes can be calculated. By allowing non-collinear spins, any directional preference for the magnetic moments of the Mn atoms can be found. In addition, more complex spin structures within the wires, such rotations or spirals may be discovered. Calculations were performed with the anti-ferromagnetic LineH′2 structure identified above, figure 4.5 (b). The Mn atoms' magnetic moments were initialized to couple anti-ferromagnetically along the $+x, -x$ or $+y, -y$ or $+z, -z$ axes, in three separate calculations. Then in each case, the spins were allowed to relax in any direction.

Table 4.4: Magnetic moments for non-collinear spin calculations on the LineH′2 structure. The table shows the magnetic moments found on each Mn atom in the cell. These are $\pm$ values to indicate that the atoms couple anti-ferromagnetically.

Configuration	$\mathbf{m}_x$ (μ_B)	$\mathbf{m}_y$ (μ_B)	$\mathbf{m}_z$ (μ_B)
AFM(x)	$\pm$4.716	0	$\pm$0.546
AFM(y)	0	$\pm$4.716	$\pm$0.546
AFM(z)	0	0	$\pm$4.747

For each calculation the binding energy of the system was unchanged. However, there appears to be a preference for the magnetic moment to align perpendicular to the surface in the $\pm z$ direction. Table 4.4 shows that when calculations were started with the magnetic moments in the $\pm x$ or $\pm y$ directions, though these remained the dominant

magnetic direction, there was some leakage of moment into the $\pm z$ direction. When started in the $\pm z$ direction, the moments remained in this direction only. These calculations were also performed for the ferromagnetic configuration of this line structure. The same pattern was observed, with the binding energies remaining unchanged, but there being tendency for the magnetism to prefer to align along the z axis, no matter which direction it was aligned to initially.

Finally some more complicated spin structures were investigated. In particular, allowing the magnetic moments to rotate from one Mn atom the next, rather than being forced to couple in rigid anti-ferromagnetism. These complex spin structures again exhibited little energetic change and had a tendency to relax back to either a ferromagnetic or anti-ferromagnetic structure aligned along the z-axis. Non-collinear spin is a complicated area and one in which much further work on this system could be performed. Both further theoretical calculations, but also experimental work to ascertain some magnetic information about the lines.

4.4 Summary

4.4.1 Summary of Findings

Nanolines are a potentially useful systems that may enable nanoscale signal transmission or other applications. The deposition of magnetic atoms on a surface is interesting to study both from the point of view of spintronics, by being used as a surface film to create a spin polarized current and fundamental physics. Manganese atoms on semiconducting surfaces have shown promise in all three of these areas. In this chapter the adsorption of Mn atoms of the Si(001) surface has been investigated, in order to determine the exact structure of experimentally observed Mn nanolines. Based on total energy calculations and simulated STM images, a candidate structure has been proposed, that explains experimentally observed nanolines and is energetically favourable. The electronic and magnetic structure of the line structure was then investigated. They were found to be anti-ferromagnetically coupled with each atom having a moment of $4\mu_B$.

4.4.2 Future Directions

The observation of nanolines on the surface provides many opportunities for future work. First it would be interesting the further experimentally investigate the spin structure of the nanolines. A number of methods can do this to some extent though often have some difficulties. Inelastic tunneling spectroscopy cannot currently be performed on semi-conductor surfaces. While spin-polarised STM and STS experiments are also very new techniques. Magnetic circular dichromism or using a vibrating sample magnetometer could be used to investigate the system studied here [99], however they both address a macroscopic scale area of the surface and so cannot easily address the exact spin structure of the nanoline. Another important extension is to investigate the possibility to increase the length of these nanolines. At 10-15 sub-units in length they are significantly shorter than some systems. This could be due a build up of strain in the sample and the effect of silicon dimer vacancies in the surface will therefore be important to look at. These can relieve strain in the sample and possibly increase the line length. However, recent experimental work has revealed that if the defect concentration increases above 4% then line formation stops and cluster formation becomes the prevalent growth mode [99].

4.4.3 Assembly Techniques and Interaction Strengths

The lines observed here are said to self-assemble. That is their structure will form when grown under the correct conditions. Self-assembly is an extremely attractive property for potential nano-devices to have. Scaling up structures created using brute force methods, such as positioning atoms using an STM, is unrealistic in many cases. While being possible in individual experimental studies, it is too intensive for use as a production method. Self-assembly offers some automation of the process that can result in the same structure being grown repeatably.

Mn lines can be contrasted with the haem seen in chapter 3. The effect of Mn atoms on the clean surface was much more dramatic thanks to the absence of hydrogen termination. This allowed complicated reconstructions, cooperation between the atoms deposited onto the surface and very strongly bound structures to form. It is interesting to find out to what extent this differing interaction paradigm from chapter 3 is due to the

difference in adsorbate, the absence of a passivating surface or both. In the next chapter an intermediary system of an Mn porphyrin on the Si(001) surface is studied. This is somewhat similar to the adsorption of a benzene ring on the Si(001) surface, which is known to bind strongly to the surface. Comparisons can be made that may illustrate how the metal is affecting the binding of the system. A binding regime somewhere between those of haem on Si(111):H and Mn atoms on Si(001) may be found.

Chapter 5

Manganese porphyrin on Si(001)

5.1 Introduction

In this chapter, elements of the previous two studies are combined and the adsorption of a Manganese porphyrin (MnPor) onto a clean silicon Si(001) surface is investigated. The aim is to see whether a porphyrin will bind strongly to a clean silicon surface and whether or not this binding is dependent upon the central metal atom. This will give an indication of whether the central Mn atom, or the outer macro-cycle, is mainly responsible for the binding to the surface. As well as combining elements of the previous two studies to answer these questions, MnPor are also of strong technological relevance in their own right. Experimental work is currently being performed on manganese phthalocyanines, the man-made porphyrin analogue of this system, for a number of specific applications such as catalysis [100, 101]. In particular, there is interest in the ordered monolayers the molecules that can form on the surface, and the different electronic and optical properties of these morphologies [23]. In addition, once monolayers have formed UV light can be used to remove the organic portion of the molecule, and implant the remaining Mn atoms into the surface [102]. The implanted ions have potential for use in spintronics and can also provide a way of doping a substrate to a specific concentration depending on the thickness of the films grown.

A study of Mn porphyrins on the clean Au(111) surface [65] found that the binding between the molecule and the surface was 0.74 eV. Another study on a cobalt surface found two separate binding regimes, one of weak physisorption at 3.5Å and one of strong chemisorption at 2.1Å from the surface [103]. These however are different

surfaces to the non-magnetic semiconductor silicon surface and so very different behaviour on this surface may well be expected. As isolated Mn atoms bind so strongly to the Si(001) surface, it is possible that the Mn atoms will be able to take a more active role in binding of the MnPor to this surface, perhaps by being displaced out of the plane of the porphyrin ring. This is often seen when ligands are bound to the central metal atom of porphyrins. The Si(001) surface also has the potential to undergo structural rearrangements, for example flattening of the surface dimers. These may be induced by the porphyrin adsorption, and this may further aid the binding.

5.2 Method

Parameters are kept similar to those in the chapter 4, in order to facilitate comparisons. Calculations were performed using the plane wave pseudopotential code VASP, with the projector augmented wave method. The PW91 exchange correlation functional was used with a plane wave cut-off of 400 eV. The unit cell was sampled with a Monkhorst Pack $2 \times 2 \times 1$ k-point mesh. A cell size of $16 \times 16 \times 22$ Å^3 was used, which ensured a vertical separation of at least 10 Å between the adsorbed porphyrin and the next periodic repetition of the surface. The surface was modelled using a six lattice plane slab with a hydrogen terminated base, as in chapter 4. Calculations were again performed using the DFT+U method as this is known from a previous work [65] to be essential for reproducing the correct ground state spin state of MnPor. There, values of $U = 4.2$ eV and $J = 1$ eV were found to be optimal and so are used here.

5.3 Results

5.3.1 Isolated Mn Porphyrin

Previous work [65] has found that the ground state of MnPor is incorrectly described by semi-local DFT functional such as PBE or PW91. Experimentally the ground state is known to be a high spin $5\mu_B$ state, however these DFT methods produce an intermediate $3\mu_B$ value for the magnetic moment. Using the DFT+U method corrects this and produces the correct high spin value for the magnetic moment. This is in contrast to the haem molecule case where DFT+U did not change the magnetic moment. The charge and spin isosurface from a DFT+U calculation is shown in figure 5.1 and illustrates the

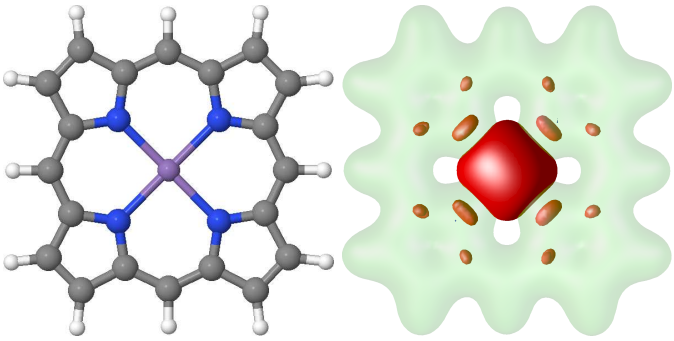

Figure 5.1: Left: Final structure of an isolated MnP molecule. Right: Charge (green) and spin(red) isosurfaces, at 0.05 e^{-} $Å^{-3}$.

magnetic moment centred around the manganese atom. The Mn-N bond length was 2.09 Å only 4% longer than the value 2.01Å found in [65].

5.3.2 Site H Adsorption

The most stable on-surface site for a Mn atom on the Si(001) surface, was the site *H* between two silicon dimers. The gas phase MnPor structure was therefore first adsorbed onto the clean Si(001) surface, with the Mn atom centred at this site. The final equilibrium structure is shown in figure 5.2. The binding energy for this structure was 0.90 eV. This is far stronger than the interaction seen for haem on Si(111):H and indicates probable chemisorption of the molecule onto the surface. There are some striking features to this adsorption geometry. Firstly there is significant non-planarity, with the majority of the molecule bending up away from the surface. The exception to this is the four central nitrogen atoms, which form bonds to the four silicon dimer atoms underlying the molecule. A simulated STM image of the adsorbed molecule is also shown in figure 5.2. There is a change in direction of the bright lobes around the porphyrin ring when imaging occupied and unoccupied states. This appears to indicate that there is an alternation of the single-double bonds around the ring once adsorbed. These images provide a guide to show what MnPor will look like, once it has been adsorbed on the surface at this site. This can help experimentalists identify whether they are producing a structure with the porphyrin at this site.

To assess the extent to which the interaction with the clean surface is due to the Mn atom, the binding energy of a free base porphyrin (FbPor) at the same site with

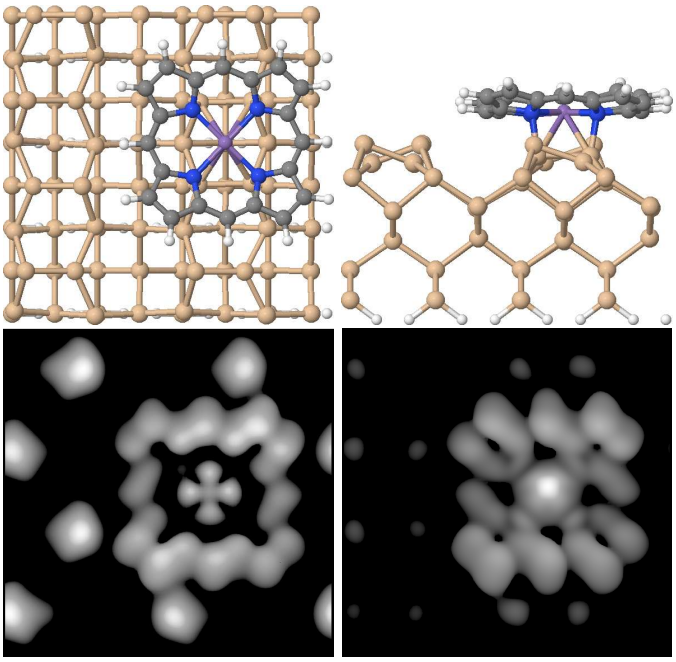

Figure 5.2: Structure of MnPor with Mn atom centred over site H, the most stable on-surface site for an isolated Mn atom. STM images below show occupied (left) and un-occupied (right) states imaged at $\pm 1.5V$.

the silicon surface is investigated. The binding energy is found to be 1.307eV which is larger than for the MnPor. This suggests that the binding is determined almost exclusively by the nitrogen-carbon macrocycle. The presence of the Mn atom may have hindered charge transfer between the molecule and surface by keeping hold of some charge.

5.3.3 Over Dimer Atom

Another site with potentially good registry between the surface and the porphyrin ring occurs when the porphyrin is placed with the Mn atom directly over the raised atom of a silicon dimer. This site may also increase interaction between the Mn atom of the porphyrin and the surface. This structure for this adsorbtion site is shown in figure 5.3. This was the most well-bound site for this MnPor on the surface. There is both a good registry between the carbon nitrogen macrocycle and the silicon dimer row below, and an interaction between the Mn atom and the silicon dimer atom directly beneath it. These combine to give a very strong binding energy for this site of 3.07 eV. The STM image shown in figure 5.3 is brighter to the right hand side of the porphyrin. This shows

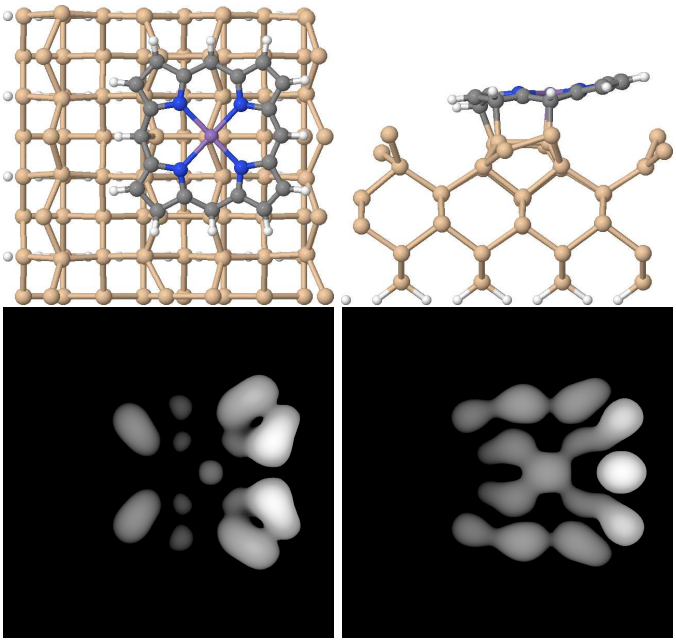

Figure 5.3: Structure of MnPor with Mn atom centred over site D. This is the most stable adsorption site for a MnPor on Si(001). STM images below show occupied (left) and un-occupied (right) states imaged at $\pm 1.5V$.

that the molecule has been buckled upward by the surface on this side and that there is a resulting difference in the bonding. The left side is bound to the surface, while the right is not.

The binding energy here, compares with a binding energy of 1.42 eV for a benzene ring on this surface [79]. Again it is important to find whether the metal atom is contributing a great deal to the binding and therefore a free-base porphyrin is simulated over the same site. This structure had a binding of 2.46 eV. In this case the Mn atom appears to be playing a role in the binding of the molecule, although the majority of the binding still comes from the C-N macrocycle. A point to note is that these structures both result in 3 silicon dimers beneath the ring being buckled. In the case of a benzene ring, calculations find that the ring straddles two dimers. Although a slightly naive interpretation, it is therefore not so surprising that the binding energy of a free-base porphyrin on this surface is around 1.5 times that of a benzene ring on the same surface, which is 1.42 eV for the bridge site [78, 79].

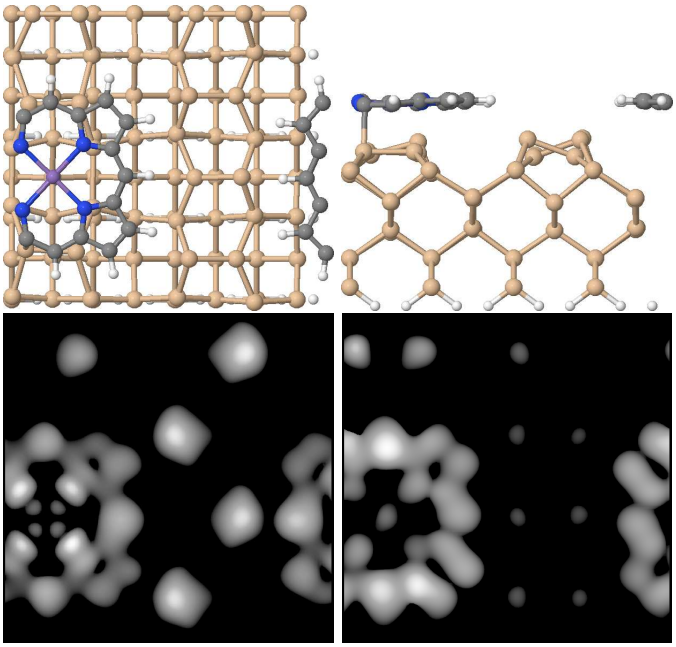

Figure 5.4: Structure of MnPor with Mn atom centred over the dimer vacancy, the most stable adsorption site for an isolated Mn atom on Si(001). STM images below show occupied (left) and un-occupied (right) states imaged at $\pm 1.5V$.

5.3.4 Adsorption Over Dimer Vacancy

The most favourable site for adsorption for a single Mn atom on the surface, was in a dimer vacancy. Therefore the MnPor is adsorbed with the Mn atom centred over a dimer vacancy. However, when over this site, the molecule was found to not bind to the surface at all and had a repulsive energy of 0.197 eV. Porphyrins are extremely stable molecules and placing the MnPor close to a dimer vacancy may have disturbed their electronic structure which results in dissociation of the molecule-surface complex being more favourable. The defect site is good for an isolated Mn atom due to the 4 bonds that it can form to the surrounding silicons. In a porphyrin the Mn atom is already 4-coordinated and so there is less benefit to forming new bonds with the silicon surface. The adsorption geometry and STM image are shown in figure 5.4. The central Mn atom does not appear as bright compared to when centered over the site H. If a free base porphyrin is more stable than a MnPor when over the vacancy, then it is possible that the Mn atom could fall out of the molecule in to the vacancy. Dimer vacancies could then potentially be sites for Mn atom deposition from MnPor molecules. Future

Table 5.1: Summary of results for the different MnPor-substrate adsorption conformations. Positive adsorption energy is defined as a binding to the surface.

Surface	Binding (eV)	Moment (μ_B)
MnPor Site H	0.904	5.00
FbPor Site H	1.307	0.00
MnPor Site D	3.075	5.00
FbPor Site D	2.455	0.00
MnPor DV	-0.197	5.00

work could investigate the barrier to this process occurring.

5.4 Discussion

5.4.1 MnPor on Si(001) Summary

The work in this section has demonstrated first that porphyrins bind more strongly to silicon surfaces in the absence of hydrogen termination. Second that the strong binding is mainly due to bonds forming between the carbon-nitrogen macrocycle and underlying silicon atoms although at specific sites, binding does involve the Mn atom. The excellent match in spacing between the macrocycle atoms and underlying silicon dimers facilitates the binding of these molecules in certain specific sites. There are also significant similarities between the binding of these molecules to the surface and the binding of a benzene ring. In particular, the flattening of dimers and slight buckling of the adsorbate are common features.

5.4.2 Conclusion To Silicon Surface Studies

Chapters 3,4 and 5 have exhibited the different ways in which functional surface structures could be assembled and have assessed the benefits of the different methods. They have also illustrated how the interaction strength between system and surface can vary greatly between systems and have demonstrated a potential way to tune this interaction strength in certain cases via hydrogen desorption. In chapter 3, DFT calculations were used to illustrate that the binding of a haem molecule to a passivated silicon surface could be increased by desorbing a hydrogen atom from the surface to create a dangling

bond that acted as a favourable binding site. This technique has already been observed experimentally for other systems. However, the lack of a significant structural change in the surface or the molecule in this case meant that the interaction between haem and surface remained weak. Chapter 4 looked at the strong binding of a Mn atom on the clean Si(001) surface. Using total energy calculations and simulated STM images a candidate structure was proposed to explain the line-like structures observed in experimental STM images. The candidate structure has a greater binding energy per atom than adsorption of separate isolated atoms. This shows that when Mn atoms interact strongly with a surface, cooperative effects are possible that lead to interesting new structures.

This chapter has drawn these two themes together, by looking at the binding of a MnPor to a clean silicon substrate. First this was compared to the haem Si(111):H binding. For MnPor on Si(001), reorganization of the surface results in a far stronger binding regime, than is present for the haem tethered to a passivated surface. Which one of the two binding regimes is more suitable may depend on the intended application. Tethered porphyrins will not change the de-localized electron structure of the macrocycle and so may be ideal if transport based systems are to be made out of the porphyrins. On the other hand if the central atom of the porphyrin is central to the intended use, such as in information storage for example, then using this atom to tether to the surface may be undesirable and it may be preferable to have it take no part in the binding.

Second MnPor on Si(001) is compared to the Mn nanoline of chapter 4. Unlike for the isolated Mn atoms and Mn nanolines on the Si(001) surface, the Mn atom of the porphyrin does not play the primary role in the binding to the surface. In fact, a free base porphyrin bound more strongly to the surface over some sites. The relatively minor interaction between the porphyrin's Mn atom and the surface may be advantageous. It may be that molecules with desirable properties can be found and then bound to a surface without overly disturbing the electronic structure of the metal atom. This would make searching for useful systems easier, as molecules in the gas phase are often more easily characterized. Of course, in many cases the binding to the substrate can be advantageous as seen for example in the ferromagnetic coupling of some porphyrins to

magnetic surfaces.

For these porphyrins on semi-conductor surfaces, the macro-cycle is more important in determining the binding, whereas the central metal atom is more important in determining the electronic properties. The strong adsorption of MnPor on this surface should be contrasted with the weak adsorption seen for MnPor on Gold surfaces. The key to the strong adsorption here is the ability of the Si(001) surface to buckle and accommodate the molecule when it is deposited, coming about due to its reactivity, particularly of the dangling created when Silicon dimers are broken.

Chapter 6

Theory of Electron Transfer

6.1 Introduction

Up until now the thesis has focused on the structural aspects of surface systems. Now the attention will shift to investigating the electron transfer properties of molecules. As outlined in chapter 1, understanding both of these aspects will enable important electron transfer calculations on surface systems to be performed. Before carrying out calculations on molecules, this chapter outlines Marcus Theory, an important theoretical framework within which electron transfer processes can be understood. Marcus theory allows links to be made between the computer simulations of an electron transfer system, and the relevant physical quantities that characterize a transfer process. In doing so, it enables conclusions to be drawn on the potential applications of various systems.

Electron transfer is a fundamental chemical process and along with the substitution of atom or ligands, is one of the two processes that can occur during a chemical reaction. For example, the transfer of electrons is involved in the change of an atom's valence and the breaking and formation of bonds. Unsurprisingly for such a fundamental process, electron transfer plays an important role in a number of biological and technological systems, some examples of which are given below.

6.1.1 Biological Importance

During aerobic respiration electrons are transferred from electron rich NADH molecules, to oxygen atoms. This is done via a number of electron transfer steps and is accompanied by the release of energy, which is used to create a proton gradient

across a mitochondrial membrane. This gradient is then used to perform work and synthesize ATP, the body's energy currency. The careful tuning of the geometry and electronic structure of the molecules in order to maximize the energy gained from the electron transfer process is remarkable. The protein cytochrome(c) is one of the intermediary molecules involved in transferring electrons from NADH to oxygen and contains a variant of the haem molecule studied in chapter 3.

In photosynthesis, the adsorption of a photon creates an excited state in a chlorophyll molecule. This excited state decays rapidly to a charge separated electron-hole pair. This pair could recombine within the chlorophyll, releasing energy as heat which would be wasteful. To prevent this, the electron is rapidly transferred away from the hole to other nearby molecules via an electron transfer chain. Meanwhile a separate electron from a nearby Magnesium atom, is used to neutralize the hole. The whole process creates a source of electrons that are subsequently used for phosphorylation and converting ADP to ATP. The competition between the charge recombination and the transfer of the electron away from the hole, is important in determining the efficiency of the photosynthetic process. In the photosynthetic reaction centre, the system is superbly tuned for great efficiency. Man-made dye sensitized photovoltaic cells are able to convert light into electrical energy but so far it has not been possible to reproduce this kind of process with the same high efficiency of plants.

6.1.2 Molecular Electronics

The transfer of electrons between redox centres forms the basis of the idea to use molecules as nanoscale systems for signal propagation. The coupling between subunits within, and charge conjugation across a molecular wire for example, affects how easily an electron can transfer down the system. The interplay between the electronic structure of oxidized and reduced molecules is therefore important to understand.

Electron transfer also influences the geometry of a system and this effect has been put to use in sensing and switching applications. When molecules bind onto a system, the structure of the system may be altered. This changes the transport properties and can thus be detected. This is most commonly seen in gas sensor devices which alter their transport properties according the amount of a certain gas molecule that has bound

to the detector. Similarly, if a system is excited by light a charge separated state may form, which in turn changes the geometry of the system [104, 105]. Examples of photo-switches such as these, will be discussed in chapter 8.

6.2 Overview of ET Concepts

6.2.1 Donor and Acceptor

The atom or ligand from which an electron leaves in a reaction is referred to as the donor, D. That which receives the electron is known as the acceptor, A. It will be useful to consider two types of electron transfer reaction. Those where an un-paired, or extra, electron is transferred from D to A. And those where the system is neutral but there is a formation or recombination of a charge separated pair.

$$D^- + A \rightarrow D + A^- \tag{6.1}$$

$$D + A \rightarrow D^+ + A^- \tag{6.2}$$

These both consist of an original state, the reactants R and a final state, the products P, in which the electronic charge distribution is different. The concepts behind how the transformations between the reactant and product states occur, is now discussed.

6.2.2 Electron Transfer As A Reaction - Arrhenius

The Arrhenius expression is an empirical expression that describes the observed temperature dependence of reaction rates. Arrhenius observed that some ET events behaved with a similar dependence. Thus he framed the transfer process as a reaction with a rate k, dependent on some important parameters, namely the activation energy E_a and temperature, T and A is the frequency factor.

$$k = Ae^{\frac{-E_a}{RT}} \tag{6.3}$$

6.2.3 Geometric Motion During ET - Taube

Henry Taube subsequently performed a series of experiments looking at electron transfer in detail [106]. In particular he looked at the structural changes occurring during an electron transfer reaction that involved the ‘Creutz-Taube ion’. His important realization was that the position of the atoms in the system was contingent on how far the

reaction had progressed. He saw that a bridging chlorine atom was passed from one side of the molecule to the other as an electron was transferred. This was the first time that the coupling of geometric motion to an electron transfer event observed, and the idea that hindrance to this motion may hinder the transfer, was fully appreciated.

6.2.4 Harmonic Approximation - Marcus

Marcus took the ideas of a chemical reaction coupled to geometric motion and put them together in a coherent framework now referred to as Marcus Theory [107]. One of its main developments, was to approximate the interactions between nuclei as harmonic. This enables them to be amalgamated into a single reaction coordinate. The electronic state curves can then be represented as single parabolas, figure 6.1. These are the diabatic state curves of the molecule. They illustrate how the energy of the molecule in a given electronic state changes as the reaction coordinate varies. The reaction coordinate can then be used to measure the progress of the reaction. Using this figure, Marcus was able to extract expressions for the activation energy that the Arrhenius reaction rate depended on. Finally he used a Landau-Zener type coupling element to model the chance of making a jump from one state curve to the other at the crossing point. Together these gave the correct observed temperature dependence for the reaction rate at high temperatures. The great vindication of Marcus theory was the discovery that its prediction of the 'Marcus inverted region' was indeed correct. This states that if the driving force is increased beyond a certain point, the reaction rate is found to decrease, rather than increase any further. This prediction is unintuitive and does not arise from simple reaction rate theories.

6.3 Marcus Theory

6.3.1 Transition State Theory

As noted, the picture of two curves in figure 6.1 describing the two electron transfer states, is not dissimilar to the picture of a conventional reaction. A finite temperature will cause thermal fluctuations in the reaction coordinate that allow the system to travel up the curve defining its electronic state. When the system fluctuates far enough from the bottom of the reactants curve to reach the crossing point, there is a chance that it

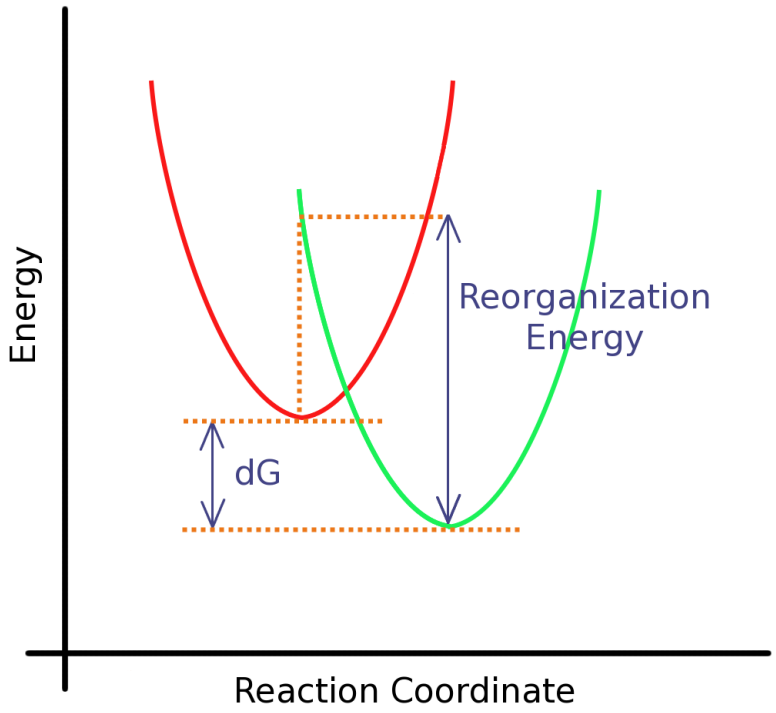

Figure 6.1: The state curves for the initial state and final state of an electron transfer reaction are shown, along with the important electron transfer parameters.

will change state to the product state. That is, that the electron will be transferred.

6.3.2 Harmonic Approximation

To progress beyond the Arrhenius expression, Marcus assumed that all the atoms in the system were coupled together with harmonic oscillator-like springs. Increasing the thermal energy of the system makes the two atoms vibrate back and forth with greater amplitude. If all the interactions are treated as harmonic, then even when they are aggregated together into the reaction coordinate, the curve drawn will be a parabola. This enables some parameters to be extracted. The two curves on the diagram 6.1 can be written as:

$$y = x^2 \tag{6.4}$$

$$(y-b) = (x-a)^2 \tag{6.5}$$

$$\rightarrow y = x^2 - 2ax + a^2 + b \tag{6.6}$$

Combining these two equations gives:

$$x^2 = x^2 - 2ax + a^2 + b^2 \tag{6.7}$$

$$= -2ax - a^2 + b^2 \tag{6.8}$$

$$x = \frac{(b - a^2)}{2a} \tag{6.9}$$

$$y = x^2 = \frac{(b - a^2)^2}{4a^2} \tag{6.10}$$

If the energy zero is placed at the bottom of the first parabola, then this expression gives the y value of the intersection, which is the activation energy E_a, from now called ΔE. The reorganization energy can also then be defined as $\lambda = -a^2$. This is the energy needed to deform the molecule from the geometry of the reactants, to that of the products, without allowing the electron transfer event to occur. That is while remaining on the same state curve. Large reorganization energies will then serve to hinder a reaction, whilst small ones will see reactions proceed with little difficulty, other factors being equal. The driving force, that is the difference in ground state energy between the reactants and the products, is defined as $\Delta G = b$ to give the energy change as:

$$\Delta E = \frac{(\Delta G + \lambda)^2}{4\lambda} \tag{6.11}$$

This equation gives the energy barrier in terms of the change in energy released and can be put into Arrhenius-like expression to yield

$$k = A \exp(\frac{-(\Delta G + \lambda)^2}{4\lambda RT}) \tag{6.12}$$

6.3.3 The Quantum Jump

The Arrhenius rate equation and a harmonic approximation give a qualitative description of the reaction rate. Marcus also required an expression for the exponential prefactor, that is, how likely is the system to transition into the product state once it has fluctuated up to the crossing point. This term also contains a temperature dependence, which is important to include. For this term, a quantum Landau-Zener expression was used [108]. This describes the probability of making a quantum jump from the reactant state surface to the product one at the crossing point. Because energy must be conserved, the transition must be horizontal in the diagram. In addition, the electron is assumed to transfer far faster than the motion of the heavier nuclei. Thus the transition occurs at a constant $\{\mathbf{R_i}\}$. Consequently, the transition can only occur at the crossing point. This is more strict than the Franck-Condon approximation which states that

the transition must be vertical [109]. Landau and Zener derived an expression for the probability of a transition, given that the probability is small and therefore diabatic.

$$P_{RP} = \frac{2\pi}{\hbar}|H_{RP}|^2 \frac{1}{\nu \Delta F} \tag{6.13}$$

Here ΔF is the difference in slopes of the two curves at the crossing point. $|H_{RP}|$ is the coupling element between the reactant and product states, explained in the next section. The rate at which the system fluctuates up the state curve and passes through the crossing point must be calculated. Then, this is used together with the Landau-Zener transition expression to calculate the rate at which transitions from reactant curve to product curve will occur. This procedure is outlined in [108] and gives the expression for the ET rate as:

$$W = \frac{2\pi}{\hbar}|H_{RP}|^2 \frac{1}{\sqrt{4\pi\lambda k_B T}} \exp\left[\frac{-(\lambda - \Delta E)^2}{4\lambda k_B T}\right] \tag{6.14}$$

This expression was derived by treating the nuclear vibrational modes as classical harmonic oscillators. Therefore it is only valid at high temperatures when the majority of the vibrational energy levels are excited. An expression for the rate which yields the correct low temperature behavior and gives the same expression as above at high temperatures, can be derived using a quantum theory. The derivation is far more complicated and is also covered in [108]. The expression derived here is effectively Fermi's Golden Rule, with a more explicit form for the density of states.

6.3.4 Electronic Coupling

An expression for the electron transfer rate has been derived using a classical harmonic oscillator approximation for the nuclei and a Landau-Zener type quantum jump for the transfer of an electron from the reactant electronic state to the product. So far, the reactant and product have been treated as independent. However, this is not always the case, particularly when the donor and acceptor are close together. When nearby, the molecular orbitals of the donor and the acceptor can overlap significantly and the two states of the system will interact. This gives an electron a small chance to quantum mechanically tunnel through the potential barrier from the donor to the acceptor, without climbing up the reaction curve. The probability of tunneling, as opposed to climbing and making a Landau-Zener jump, is accounted for by the coupling matrix element

$|H_{RP}|$ out in front of the rate expression. The tunneling probability has the effect of lowering the energy barrier needed for a reaction to take place. A gap of $2H_{RP}$ opens up at the crossing point where

$$H_{RP} = \langle \psi_R | \hat{H} | \psi_P \rangle \tag{6.15}$$

6.4 Adiabatic Representation

In the absence of coupling, the electron transfer process is said to be diabatic and that states used to represent the reactant and product $|\psi_R\rangle$ and $|\psi_P\rangle$ are orthogonal to each other. When the reactant and product states are coupled however, they are by definition no longer orthogonal and no longer diabatic states of the system. Instead of considering two states R and P with the electron localized on either donor or acceptor, it can be more convenient to think of a ground state and an excited state which are linear combinations of R and P

$$|\psi_G\rangle = c_1|\psi_R\rangle + c_2|\psi_P\rangle \tag{6.16}$$

$$|\psi_E\rangle = c_1|\psi_R\rangle - c_2|\psi_P\rangle \tag{6.17}$$

The coefficients c_1 and c_2 for these states are found by diagonalizing the following matrix to give a measure of how much of each $|\psi_R\rangle$ and $|\psi_P\rangle$ is present in each adiabatic state:

$$H = \begin{pmatrix} \langle \psi_R | H | \psi_R \rangle & \langle \psi_R | H | \psi_P \rangle \\ \langle \psi_P | H | \psi_R \rangle & \langle \psi_P | H | \psi_P \rangle \end{pmatrix} \tag{6.18}$$

These states produce two separated smooth curves. Now the electron transfer process can be viewed as one in which the electron gradually transfers from donor to acceptor as the geometry is changed from R to P. In this case the electronic state isn't changing during the course of the reaction. Electron transfer can be modelled using both diabatic and adiabatic curves in different approaches. Either as a discrete reaction, or a continuous process. It is important to note that the two adiabatic and diabatic models are describing the same process and are simply different ways of thinking of the problem in order to bring to the fore the most important aspects of particular situations.

The work here is mainly concerned with hopping type events and discrete transfers of electrons, the frameworks usually taken as most representative of biological electron

transfer. The coupling matrix element will not play a central role in the work at this stage and therefore the diabatic treatment of electron transfer is most appropriate.

Chapter 7

$\mathcal{O}(N)$ Implementation of constrained DFT

7.1 Introduction

In the previous chapter the importance of electron transfer (ET) to a number chemical and biological processes was described. Then Marcus theory, the theoretical framework built to study ET, was outlined. Chapters 1 and 6, described why there is great motivation for studying electron transfer in large surface systems. The next two chapters of the thesis aim to provide a method with which the electron transfer characteristics of these large molecular systems can be studied. First, in this chapter, the implementation of the method is described. Then in the next chapter, some initial results are presented.

Chapters 3, 4, and 5 illustrated that DFT is an excellent method for studying the properties of molecules and other systems on surfaces. Its combination of speed and accuracy, along with the large body of previous work and expertise which provide a guide as to how well certain systems can be treated, make it a good choice in these cases. Using DFT as the basis for studying electron transfer in surfaces systems is therefore very appealing. In this section the problems encountered when trying to use DFT for electron transfer are outlined and an implementation that partially overcomes them is described.

7.1.1 Problems With DFT

Chapter 6 illustrated two types of electron transfer process that are of interest. They were the transfer of an unpaired or excess electron from a donor to an acceptor, and the charge separation and recombination in a neutral system. Both of these have relevance in potential on-surface systems. However, there are certain limitations to DFT which prevent it from being able to study electron transfer very easily in either of these situations. In addition, when trying to study these situations in large molecule-surface complexes problems are further exacerbated.

The first significant error limiting DFT's use for electron transfer, is known as the self-interaction error (SIE). It is particularly apparent when looking at localized un-paired electrons. The SIE arises from the mean-field treatment of the Coulomb interaction. This results in every electron interacting with the charge due to every electron in the system - including itself.

$$E_H[n(\mathbf{r})] = \int \frac{n(\mathbf{r})n(\mathbf{r}')}{|\mathbf{r}-\mathbf{r}'|}\mathrm{d}\mathbf{r} \tag{7.1}$$

Strictly the integral should only count contributions of density that arise from different electrons. Instead electrons effectively repel themselves as well as each other. This results in the over delocalization of electrons. DFT will naturally produce overly delocalized charge distributions in system. In Hartree-Fock this error is not present due to its cancellation by the exact exchange interaction. In DFT, exchange effects are only included approximately and therefore do not cancel the self-interaction completely.

Whilst the SIE error may seem severe, it does not prevent DFT from providing accurate ground state energies and geometries in the majority of cases. Overly delocalized charge distributions do however cause a number of important problems. The most commonly cited problem is the under-estimation of band gaps in materials [110]. There are also situations where the energy and geometry of the system are very sensitive to the density, for example when bonds in the system are stretched or broken [111]. The SIE can also be responsible for incorrectly identified ground states in molecules with unpaired electrons [112].

DFT's second limitation is simply that it is a ground state theory. The second Hohenberg-Kohn theorem states that the density which produces the lowest energy, is

the one most like the true ground state density. It does not specify how to search for the densities of excited states. This usually makes it impossible to look at the charge separated states of a molecule, as these will often not be the ground state of the system. That is to say that even if a calculation is fixed at the charge separated geometry, the charge separated distribution will not be the one produced by DFT. Both these effects will be illustrated in studies in chapter 8.

The above issues make standard DFT unsuited for electron transfer. Additionally, the eventual goal is to study the electron transfer processes occurring in large biological molecules and surface systems, in order to assess their potential for use in nano-technological devices. Including a surface in the calculation increases the system size greatly. Sometimes the system may be a biological derivative and in these systems, solvents will play an important role. Including this solvent in simulations also greatly increases number of atoms in the simulation. The exact scaling of a DFT calculation depends on the specific implementation used. The most common and straight-forward schemes scale cubicly with the number of atoms in the system and this provides a sharp cut-off to the number of atoms that can be included in a simulation. Consequently, studies of large systems are often prohibitively costly to perform.

7.1.2 Fixing the Problems

Much work has been performed finding ways to address the issues above and each of the problems described above has at least a partial solution. To reduce the self-interaction error, it is possible to use the hybrid functionals [45] [46] [47], that were briefly described in chapter 2. By modifying the exchange correlation functional to include a portion of Hartree-Fock exchange, they partially cancel the self-interaction error in the Coulomb term of the energy expression. Full Hartree-Fock theory is self-interaction free, but does not include correlation effects and is therefore inaccurate in other ways. Hybrid functionals are seen to improve band-gaps for many systems [113]. There are also more complicated methods to treat the self-interaction error. Fully self-interaction corrected methods are amongst the most complex of current DFT extensions and can provide an accurate solution to the error at somewhat higher computational cost [110]. There are also extensions to DFT that enable the study of excited states

and thus provide ways to access some of the charge separated density distributions not produced by conventional DFT. Time-dependent density functional theory [32], particularly in linear response mode, is one method that has been able to successfully calculate excited state energies and charge distributions. However, even this method still has problems, such as incorrectly accounting for electron-hole interaction in charge separated states [114]. It is also more computationally demanding than DFT, although there is scope for future developments. Another popular method for studying transport processes is the Non-Equilibrium Green's Function (NEGF) method [33]. This models a transport process by treating the transport of charge as a scattering problem and is able to produce the steady state current distribution present in the molecule under a bias voltage. Various other *ab-initio* methods have been used to investigate electron transfer for example, the work of Sprik [115, 116] and Marzari [117]. Furthermore there are also implementations of DFT that are able to scale linearly with the number of atoms in the system [36]. Although they require careful use and are inefficient for small systems, they can be used to overcome the cubic scaling of conventional DFT. It would be advantageous if the modifications to DFT allowing ET to be performed could fit easily into a linear scaling code. It would then be possible to perform ET simulations on large complex surface-molecule based systems.

However, many of the corrections outlined above can be challenging to fit within a linear scaling framework. They will often destroy the O(N) behaviour of the system and thus would not be ideal to study large systems. Instead of these, a method is desired that addresses the specific problems DFT faces when studying electron transfer, and does so in such a way that will not preclude use in a linear scaling DFT code. Constrained DFT (cDFT) [34] is one such extension that has recently been developed and does not affect the scaling of a code. In this chapter, the formalisms of $\mathcal{O}(N)$ DFT and cDFT are described. Then, an implementation of cDFT into an $\mathcal{O}(N)$ code is described and some initial benchmarking results presented. This will allow large scale electron transfer simulations on relevant biological and surface systems to be performed with the potential to make useful contributions to molecular electronics and nanotechnology.

7.2 Linear Scaling DFT

A number of linear scaling DFT codes that have been developed. These include, SIESTA [118], ONETEP [119] , OPENMX [120], and CONQUEST [121]. Though the actual implementations in each code are different, the basic principles behind them are similar. Linear scaling codes take advantage of the near-sightedness of electronic matter [122]. The principle of near-sightedness states that the effect of the electron density at one point of the system, on that at another point of the system, decays exponentially with distance in a large bandgap system. In principle therefore, the properties of a system at a certain point, should only depend on the environment immediately around that point. Thus the amount of information to be stored and computed only grows linearly with the system size, not cubicly. This phenomenon manifests itself computationally through the locality of the density matrix. The number of non-zero elements in the density matrix will grow linearly with size, rather than cubicly, as many off-diagonal elements will be approximately zero. The work here implements the constrained DFT formalism into a linear scaling code. Whilst no development of linear scaling algorithms is performed, an understanding of their workings is useful to help implement the constraint effectively. A brief outlined of linear scaling DFT is therefore given here.

7.2.1 Mathematics of Implementation

In conventional DFT, the energy is minimized subject to variations in the electron density and implicitly, the single electron Kohn-Sham orbitals. In a linear scaling code, density matrix minimization, which can scale linearly, takes the place of matrix diagonalization, which scales cubicly. The Kohn-Sham equations are re-written in terms of the density matrix and density. The energy is then minimized subject to variations in these, thus forgoing direct use of the Kohn Sham orbitals. The density matrix is defined formally as:

$$\rho(\mathbf{r}, \mathbf{r}') = \sum_i f_i \psi_i(\mathbf{r}) \psi_i(\mathbf{r}')^\star \tag{7.2}$$

The total energy expression can then be written with each term depending explicitly on either the density or the density matrix. With the kinetic energy term in terms of the

density matrix, this means that there is no role for the Kohn-Sham orbitals.

$$E[n,\rho] = E_{\mathrm{KE}}[\rho(\mathbf{r},\mathbf{r}')] + E_{\mathrm{har+xc+LocPP}}[n(\mathbf{r})] + \quad (7.3)$$

$$E_{\mathrm{KE}} = \frac{-\hbar^2}{2m}\int \mathrm{d}\mathbf{r}\mathrm{d}\mathbf{r}'(\nabla_r^2\rho(\mathbf{r},\mathbf{r}'))\delta(\mathbf{r}-\mathbf{r}') \quad (7.4)$$

$$E_{\mathrm{NLPP}} = 2\int \mathrm{d}\mathbf{r}\ \mathrm{d}\mathbf{r}'\ V_{\mathrm{NLPP}}(\mathbf{r}',\mathbf{r})\rho(\mathbf{r}',\mathbf{r}) \quad (7.5)$$

$$n(\mathbf{r}) = 2\rho(\mathbf{r},\mathbf{r}) \quad (7.6)$$

The near-sightedness of electronic matter is then used to impose the spatial cut-off on the density matrix. The use of sparse matrix multiplication routines and efficient load distribution of the calculation across processors [123] allows the required multiplications and energy minimization to be performed in a linear scaling manner. The result of an $\mathcal{O}(N)$ calculation gradually approaches that of a diagonalization calculation as the density matrix cut-off is increased.

The key point of linear scaling DFT is that at no point is a matrix diagonalized, as this is an operation that scales cubicly with matrix dimensions. To see how the density matrix is used to minimize the energy without diagonalization, it is first noted that it is computationally very difficult to work with a 6-dimensional object like $\rho(\mathbf{r},\mathbf{r}')$, no matter how local it is made. As in conventional DFT a basis must be introduced and used to represent the density matrix. Doing so assumes that the density matrix is separable. In CONQUEST the density matrix is expanded in terms of 'support functions' defined within atomic centred spheres, which themselves are expanded in a basis. Two possible basis sets can be used in CONQUEST. These are B-Splines (BLIPS) [124] and Pseudo-Atomic-Orbitals (PAO) [125]. Both basis sets can be used to perform linear scaling calculations. However, to create population schemes needed in a cDFT calculation, an atom centred basis is required and therefore the PAOs are used in the work here. Atomic orbitals, are functions that mimic the solutions to the Schrödinger equation for an isolated atom. These consists of radial functions, multiplied by spherical harmonics. Details of how CONQUEST creates similar functions to these and uses them to perform integrals and create matrices can be found in [125]. The other basis set available is B-splines [126, 127]. These allow better performance in linear scaling calculations, but will not be used here. Note that although a basis is used, the wave-functions are never built from it, only the density matrix elements directly. Formally the following can be

written:

$$\psi_i = \sum_\alpha c_{i\alpha}\phi_\alpha \tag{7.7}$$

$$\rho(\mathbf{r},\mathbf{r}') = \sum_{\alpha\beta} \phi_\alpha(\mathbf{r}) K_{\alpha\beta}\phi_\beta(\mathbf{r}') \tag{7.8}$$

$$K_{\alpha,\beta} = \sum_i f_i c_{i\alpha} c_{i\beta} \tag{7.9}$$

$$\rho(\mathbf{r},\mathbf{r}') \rightarrow 0 \text{ as } |\mathbf{r}-\mathbf{r}'| \rightarrow \infty \tag{7.10}$$

Locality is imposed by making these support functions only non-zero inside spherical regions around each atom. The density matrix then has a cut-off imposed meaning that elements describing interactions between support functions separated by distances greater than this will be zero. To perform a calculation, an approximate density is generated. A minimum energy for this density is found by varying the density matrix. This procedure takes the place of diagonalization in conventional DFT codes. The minimum energy density matrix will not correspond to the input density and therefore the process must be iterated to self-consistency using a suitable density mixing scheme.

During each minimization, certain constraints must be imposed on the density matrix to ensure physically reasonable results are produced. The most important of these is that the density matrix must be idempotent. That is that it must be a projector, in order to correspond to a real physical observable [36]. Idempotency requires that its eigenvalues must be exactly 0 and 1. CONQUEST imposes idempotency by enforcing weak idempotency, where eigenvalues are between 0 and 1, using the LNV implementation [128] of the McWeeny method [129]. This method recasts the density matrix using the following polynomial

$$f = 3x^2 - 2x^3 \tag{7.11}$$

This polynomial has the important property that its gradient anywhere between 0 and 1 will drive the values to either 0 and 1. The density matrix is written in terms of an auxiliary density matrix L and the overlap matrix S and real density matrix K. This matrix is varied at each step using a conjugate gradient scheme, until the energy is minimized. By minimizing the energy with respect to changes in L, but using K in all the energy expression equations, the energy is minimized whilst driving K towards

idempotency.

$$K = 3LSL - 2LSLSL \tag{7.12}$$

$$\frac{\partial E}{\partial L_{ij}} = 3(HLS + SLH) - 2(HLSLS + SLHLS + SLSLH) \tag{7.13}$$

$$L \rightarrow L + \lambda S^{-1}\frac{\partial E}{\partial L_{ij}}S^{-1} \tag{7.14}$$

Note that the matrices used in these multiplications must be sparse to enable the process to scale linearly.

7.3 Constrained DFT Formalism

7.3.1 Introduction

Having seen the workings of linear scaling code, in this section, the cDFT method is outlined. In cDFT, the density is forced to satisfy some physically or experimentally motivated constraint and then a search made for the lowest energy density that exhibits this property. Imposing charge constraints such as this is an idea that dates back to 1970 [34]. Indeed there are already constraints in conventional DFT, such as the density being forced to integrate to the correct number of electrons via the orthogonality of the Kohn-Sham orbitals. Until recently, cDFT implementations were rather inefficient. However recently, a new way of implementing cDFT was formulated by Wu and Van Voorhis that enables the calculations to be performed with only moderate extra computational cost and the same scaling compared to conventional DFT [35, 114, 130, 131]. By using this method to impose constraints on the charge densities produced by DFT, it will be possible to study both the case of localized individual electrons and charge separated states of the system. Furthermore, cDFT can be implemented into a linear scaling code, without affecting the $\mathcal{O}(N)$ behaviour. It will therefore provide a scheme within which ET simulations of larger systems can be performed.

7.3.2 Phenomenological Description

Stated simply, constrained DFT involves searching for an extra potential which, when added to the Kohn-Sham Hamiltonian, results in the density distribution possessing a desired property. To illustrate, consider the case of an unpaired electron being added to a symmetric molecule. As stated, often DFT will prefer to de-localize this elec-

tron across the whole molecule and create a symmetric geometry. The cDFT method aims to search for the additional potential V_c which produces the lowest energy whilst having the electron localized on one part of the molecule. Adding a potential to the Hamiltonian in this way can seem somewhat heavy handed, especially as the form of the potential appears arbitrary. A tall thin potential could be used. Or a short wide one, which may have the same effect. The role of cDFT is to formulate this extra potential in a physically reasonable way and to then locate the size, or depth, of the potential needed to impose the constraint, in a self-consistent manner. In the original implementations of cDFT this was done by selecting different potentials and performing a fully self-consistent calculation for each one, until one was found that imposed the desired constraint. This results in many fully self-consistent calculations being required to locate the desired constraining potential. The method was recently reformulated in a more efficient way by Wu and Van-Voorhis [35, 114, 130, 131] and this formalism is described in the next section.

7.3.3 Mathematical Formalism

A spatial function $w_c(\mathbf{r})$, is used to delineate the area within which the number of electrons must equal a certain value N_c. Constraints can be applied to specific types of electron in the system, such as those of a certain spin, or of a certain angular momentum. In this work it is only ever the total charge density that is constrained. The constraint can then be written as an integral of this spatial function, multiplied by the charge density, over all space:

$$\int w_c(\mathbf{r}) n(\mathbf{r}) \mathrm{d}\mathbf{r} = N_c \tag{7.15}$$

To minimize the Kohn-Sham energy whilst ensuring the charge satisfies this constraint, the method of Lagrange multipliers for constrained minimization is used, as outlined in chapter 2. A new functional is written that is the sum of the Kohn-Sham energy and the constraint term, multiplied by a variable, the Lagrange multiplier.

$$W[n(\mathbf{r}), V_c] = E_{\mathrm{KS}}[n] + V_c(\int w_c(\mathbf{r}) n(\mathbf{r}) \mathrm{d}\mathbf{r} - N_c) \tag{7.16}$$

This functional is now minimized with respect to the density and V_c to give the lowest energy subject to the constraint. The terms produced by differentiating the energy E_{KS}

are the same as those of conventional DFT. Differentiating the constraint simply gives $V_c w_c(\mathbf{r})$, resulting in:

$$\left[-\frac{1}{2}\nabla^2 + v_n(\mathbf{r}) + \int \frac{n(\mathbf{r})}{|\mathbf{r}-\mathbf{r}'|}\mathrm{d}\mathbf{r}' + v_{xc}(\mathbf{r}) + V_c w_c(\mathbf{r})\right]\phi_i = \epsilon_i \phi_i \tag{7.17}$$

$$(H_{KS} + V_c w_c)\phi_i = \epsilon_i \phi_i \tag{7.18}$$

This is a new single-particle Schrödinger equation containing an extra potential that ensures there are a certain number of electrons reside in the area $w_c(\mathbf{r})$. The form of the constraint $w_c(\mathbf{r})$, that is the shape of the potential mentioned earlier, is constant throughout the calculation and the definition of this shape will be discussed in the next section. However, the height of the extra potential, V_c, can be varied and needs to be determined.

Wu and Van-Voorhis showed that the functional W is convex with respect to changes in V_c and therefore it has just one stationary point and that this is guaranteed to be a maximum. The first differential is easily calculated and the second can be obtained using perturbation theory if desired.

$$\frac{\partial W}{\partial V_c} = \int w_c(\mathbf{r}) n(\mathbf{r}) d\mathbf{r} - N_c \tag{7.19}$$

Their availability provides a new way of formulating the calculation. At each step in the overall Kohn-Sham self-consistent cycle, the Lagrange multiplier is varied until the constraint is satisfied for the current density. When this is the case, the output density is used to create the input for the next Kohn-Sham self-consistent step. In this next step, the density has changed, and so V_c will need to be updated again to reinforce the constraint. The process continues in this loop within a loop structure. The convexity of the functional W guarantees, that this process will lead to the minimum energy, with the constraint satisfied. The availability of the first and second derivatives of W mean that updating the Lagrange multiplier in the inner loops can be done efficiently. It is noted that the second derivative is actually unavailable in a linear scaling code which does not have immediate access to the system's wave-function, though this is not a significant issue here.

7.3.4 Population Schemes

Now the form of the constraining potential is considered and a comparison between a number of different ways to formulate the constraining potential is presented. So far the weight potential has been treated as a spatial function $w(\mathbf{r})$. Building a physically reasonable spatial potential would be challenging. However with a basis this spatial function becomes a matrix

$$\langle \phi_i(\mathbf{r}) | w_c(\mathbf{r}) | \phi_j(\mathbf{r}) \rangle = w_{ij}^c \tag{7.20}$$

Therefore instead of considering $w_c(\mathbf{r})$ as a spatial function, it is possible to formulate it directly in terms of a matrix. This is done using atomic population schemes, discussed in the next section. Some of these have been demonstrated as being an accurate measure for the number of electrons associated with an atom. There is no un-ambiguous way to apportion electron density to atoms and so of course, the use of population schemes is an approximation.

The construction of the constraining potential via a population scheme is the limiting approximation of cDFT. A constraint will not reproduce the experimentally observed localized or charge separated state exactly. While at short ranges the energies can vary greatly between schemes, it has been found that for long ranges, the energies produced are not overly dependent on the exact form of the constraint [114]. Fortunately one of the principle areas to which these calculations will be applied, is large systems and long range electron transfer. When studying a system it is important to test different population schemes to ensure that results are not dependent on the type of constraint used to the point where the physical or chemical conclusions drawn are determined only by the form of the constraint used. For example, different population schemes should produce similar estimations for parameters such as the reorganization energy. There of course could also be different constraints entirely. For example, fixing the bias voltage across a sample in a NEGF calculation to give the steady state current distribution. Constrained DFT should not produce conclusions contradictory to those drawn accurately from experiments. Collaboration is therefore once again important.

7.4 Implementation of cDFT in CONQUEST

Having seen how cDFT can be implemented in a conventional DFT code, the slight changes needed for implementation into a linear scaling code that uses the density matrix, are outlined. This implementation has been done in such as way as to enable calculations can be performed both in linear scaling mode and in parallel. In a linear scaling implementation the expression

$$W = E_{\mathrm{KS}} + 2V_c\mathrm{Tr}[Kw_c] \tag{7.21}$$

is used directly, rather than the coupled set of Schrödinger equations. The density matrix is varied until the energy is minimized for a given $n(\mathbf{r})$. The Lagrange multiplier is then altered to impose the constraint. The density matrix is then minimized again and the process continued. As stated, minimizing the density matrix has the same effect as diagonalization. It therefore has to be done a number of times to get self-consistent charge density. There is a possibility that the updating of the Lagrange multiplier, could be incorporated within the density matrix minimization process, which would further speed up the process. However, this will not be explored for the moment.

7.4.1 Brent Minimization

Finding the Lagrange multiplier which imposes the constraint is equivalent to finding where the function $|\mathrm{Tr}[Kw_c] - N_c|$ is zero. This is simply a 1-dimensional line search. In CONQUEST this is done using the Brent algorithm for 1-dimensional minimization [132]. The first step is bracket the minimum using the simplest possible method. Once bounds for V_c have been established, its value is located using a golden-ratio search line minimization. Convergence is found to be rapid and stable for all systems tested, as it should be for this simple procedure.

7.4.2 Mullikan Population

The Mullikan population scheme is one of the simplest population schemes. It involves just the overlap matrix, which is easily available in a DFT code. It can be summarized as:

$$w^c_{\lambda\nu} \;=\; S_{\lambda\nu} \text{ if } \lambda \text{ and } \nu \;\in\; C \tag{7.22}$$

$$= \frac{1}{2} S_{\lambda\nu} \text{ if } \lambda \text{ or } \nu \in C \quad (7.23)$$

$$= 0 \text{ else} \quad (7.24)$$

where $S_{\lambda,\mu}$ is the overlap matrix between atomic basis functions given by $S_{\lambda,\mu} = \langle\phi_\lambda|\phi_\nu\rangle$. λ and μ and basis function indexes and C is the set of constrained atoms. Unfortunately this scheme does not produced a well defined constraint [114]. This is because it is not a projector and therefore cannot correspond to a physical observable, such as the density attached to a number of atoms. This results in the Mullikan scheme giving qualitatively incorrect energies for the constrained systems as seen in figure 7.2.

7.4.3 Löwdin Population

The Löwdin population is more complicated to implement as it involves the use of the square root of the overlap matrix. It is written in matrix form as:

$$w^c_{\lambda\nu} = \sum_{\mu\epsilon C} S^{1/2}_{\lambda\mu} S^{1/2}_{\mu\nu}$$

where C runs over the atoms in the constrained set. The Löwdin weight matrix is a projector and therefore corresponds to a physical observable [114]. It gives realistic energy changes when the constraint is imposed, as in figure 7.2. The $S^{1/2}$ matrix is not routinely available in CONQUEST and moreover, creating it is not immediately a linear scaling operation as conventionally it requires diagonalization of the overlap matrix.

As diagonalizations are to be avoided in a linear scaling code, in CONQUEST the $S^{1/2}$ matrix is obtained via a linear scaling iterative decomposition, recently devised by Jansik *et al* [133]. This method is able to produce the square root of the overlap and the inverse square root. Thus it then also provides a way to create the inverse S matrix required by linear scaling codes to minimize the density matrix in the conjugate gradient scheme, see equation 7.14. There are other recursive methods which can be used to build the inverse overlap matrix such as Hotelling's method [134] or that of [135], however these can find inversion difficult for some systems. Therefore investigating other potential inversion schemes is a useful side benefit.

The iterative method used to create the square-root overlap matrix is outlined below, following [133]. The method does not involve diagonalization, only matrix multiplications, which with care can be performed in a linear scaling manner.

$$\mathbf{Z_0} = \mathbf{I} \qquad \mathbf{Y_0} = \mathbf{S} \tag{7.25}$$

$$\mathbf{X_k} = \lambda \mathbf{Y_k Z_k} \qquad \mathbf{Z_{k+1}} = \mathbf{Z_k T_k^{(m)}} \qquad \mathbf{Y_{k+1}} = \mathbf{T_k^{(m)} Y_k} \tag{7.26}$$

$$\mathbf{S^{1/2}} = \lambda^{1/2} \lim_{k\to\infty} \mathbf{Z_k} \qquad \mathbf{S^{1/2}} = \lambda^{1/2} \lim_{k\to\infty} \mathbf{Y_k} \tag{7.27}$$

for

$$||\lambda \mathbf{S} - \mathbf{I}||_2 < 1 \tag{7.28}$$

The operator T is used in its third-order form:

$$\mathbf{T_k^{(3)}} = \frac{\mathbf{1}}{\mathbf{8}}(\mathbf{15I - 10X_k + 3X_k^2}) \tag{7.29}$$

And the scaling factor lambda coming from the Gershgorin circular theorem is given by

$$\lambda \frac{2}{\epsilon_{\max} + \epsilon_{\min}} \tag{7.30}$$

where ϵ are the limits to the minimum and maximum eigenvalues of the overlap matrix, which can be determined without diagonalization. Continuing iterations of this scheme produces the square-root and inverse square-root of the overlap matrix. Whilst an iterative procedure is somewhat time-consuming, this only needs to be performed each time the overlap matrix is updated. That is only once every atomic step. Steps in the electronic minimization use the same square-roots and therefore this procedure does not strongly affect the speed of the calculation. Note that this is only the case if the basis is not varied during the calculation step. CONQUEST is able to vary the support functions throughout the calculation in order to find a basis which produces the lowest energy minimum. However, varying of the basis will be avoided in the cDFT implementation here.

As stated, there is much interest in being able to accurately produce the dense S^{-1} matrices that come from the poorly conditioned overlap matrices often found in molecular systems. Inaccurate inversion limits the class of systems for which linear scaling schemes can perform well. The accuracy of the overlap matrix decomposition used here is investigated for two different system. An 8 atom bulk silicon cell

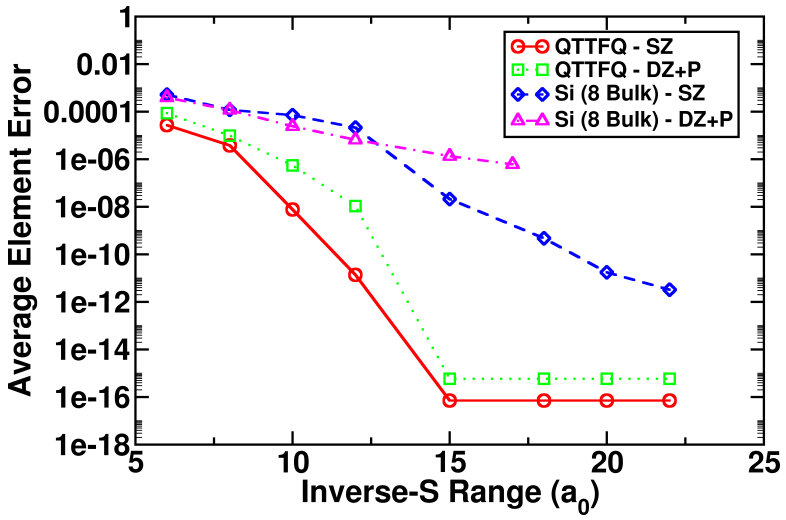

Figure 7.1: Graph showing the accuracy with which the basis function overlap matrix of a system can be decomposed into its square root, using the scheme outlined in section 7.4.3. SZ lines are calculations with a single-zeta basis, DZ+P with a double-zeta + polarization basis.

and small molecule known as tetrathiafulvalene diquinone (QTTFQ). The effect of the matrix multiplication ranges, which are in effect are determined by the density matrix cut-off, on the accuracy of the decomposition are shown in figure 7.1. The decomposition is less accurate for more poorly conditioned overlap matrices, such as those from double-zeta basis sets as opposed to simpler single-zeta. An interesting point is that it appears far harder to decompose the overlap matrix of a condensed phase system than an isolated molecule. This is because the the bulk silicon solid has a very dense inverse S matrix. While studying condensed phase systems will be challenging with this population scheme, for isolated molecules the method performs well. Care should be taken when using the Löwdin scheme, and iterative decompositions in general, to ensure the decomposition is performing accurately.

7.4.4 Becke Weight Population

The Becke weight population scheme involves partitioning the system into fuzzy spheres centred around each atom. These are similar, though more complicated, than the support function regions. By integrating the charge density on the grid points within these regions, a value for the electron population of each atom can be obtained. The cre-

ation of the spheres is described in detail in [136] and originates from methods which partition integrals into atomic spheres. The essential point is that the total charge of the Becke weights is equal to the total charge of the system. The partition radii and parameters can be adjusted to give the correct bond polarity making this scheme physically appealing. The weight matrix is then found by integrating across multiple atoms as follows:

$$w^c_{\lambda\nu} = \sum_{n\epsilon C} \int \mathrm{d}\mathbf{r} \phi_\lambda(\mathbf{r}) w_n(\mathbf{r}) \phi_\nu(\mathbf{r}) \tag{7.31}$$

The Becke system is considered to be the most accurate of the three population schemes over long ranges [114] and shows similar results to the Löwdin method in figure 7.2. Another advantage is that the constraint does not depend as strongly on the basis used as it does in for example the Löwdin scheme, where direct use is made of the overlap matrix elements.

A final point is that the Becke scheme allows analytic calculation of the force components in a far easier manner for an $\mathcal{O}(N)$ code than the other schemes. Finding the gradient of the Löwdin population involves finding the gradient of the $S^{1/2}$ matrix. This is only obtained straight-forwardly by diagonalizing the overlap matrix, which must be avoided in a linear scaling code. The gradient of the Becke population scheme has a simpler analytic expression to calculate the forces with. Calculations in the thesis will use the Becke scheme primarily. However, it is important to have more than one scheme available to check that results do not overly depend on the population scheme used.

7.4.5 $\mathcal{O}(N)$ Calculation Convergence

CONQUEST can perform DFT using either a conventional diagonalization method or linear scaling density matrix minimization. It remains to be shown that the code is able to perform cDFT accurately when running in $\mathcal{O}(N)$ mode as well as when using the diagonalization procedure. It is particularly important to show that limiting the range of the density matrix, does not adversely effect the application of a constraint. To illustrate this, a constraint is applied to alter the charge state of the central metal atom in a Magnesium porphyrin molecule. In figure 7.3, the energy for the constrained state is plotted as the density matrix range is increased for an $\mathcal{O}(N)$ and a diagonalization

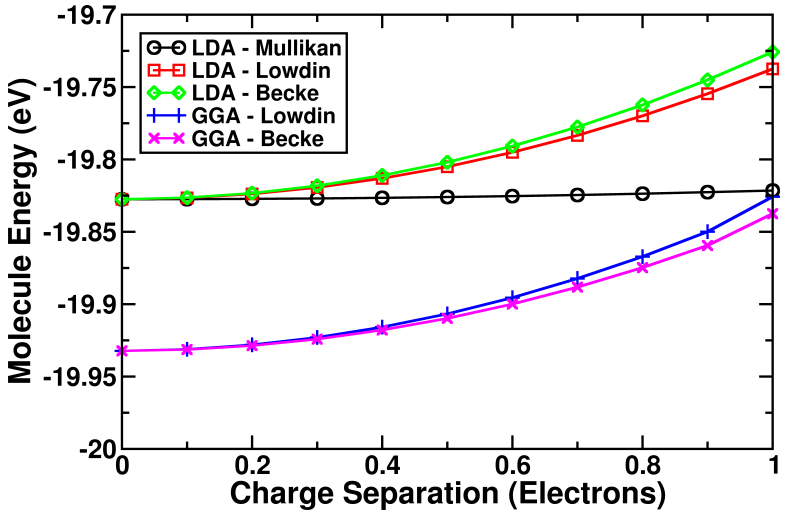

Figure 7.2: The change in energy as charge is separated in the nitrogen molecule. Energy cost is similar for both LDA and GGA exchange correlation functionals. Mullikan scheme energy change un-physically low.

run. The energy converges towards that of a diagonalization calculation. Once the range of the density matrix is larger than the maximum distance between two atoms, the energies are converged, to within the accuracy to which the constraint is applied, which is 10^{-4} Hartrees here.

7.5 Electron Transfer Parameters

Having outlined the methodology of linear scaling DFT and constrained DFT, the ways of extracting the important electron transfer parameters from a calculation, are now described. The electron transfer rate as in chapter 6 is given by:

$$k_{ET} = \frac{2\pi}{\hbar}|V_{RP}|^2 \frac{1}{\sqrt{4\pi\lambda k_{\mathrm{B}}T}} \exp\left(\frac{-(\lambda - \Delta E)^2}{4\lambda k_{\mathrm{B}}T}\right) \tag{7.32}$$

The first parameter to consider is the change in energy ΔE. Strictly, in a system at a finite temperature and including both a molecule and a solvent, the free energy ΔG should be used. Some implementations of cDFT have been designed specifically with this in mind [137]. However, the simulations in this thesis will be of just isolated molecules, and effectively at zero temperature. Therefore it will be sufficient to consider just the total energy ΔE and this can be read of as the difference between energy minimums of different constrained states.

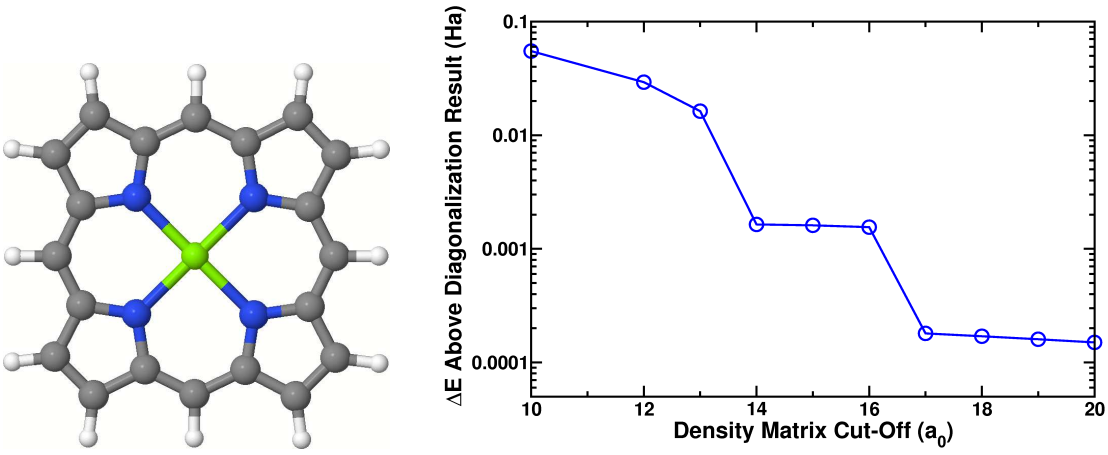

Figure 7.3: Graph showing the convergence of energy from a $\mathcal{O}(N)$ run to that of a diagonalization run, as the density matrix cut-off is increased. Once the range is larger than the greatest separation between atoms in the system, the energies should be the same to within the accuracy with which the constraint is imposed.

7.5.1 Reorganization Energy

The reorganization energy is the energy needed to distort a molecule from the geometry of one state to another, while not allowing the electronic distribution to change. The closer the donor and acceptor are to each other, the larger the reorganization that must occur when the electronic distribution around them changes. This serves to inhibit electron transfer. The reorganization energy can be calculated straightforwardly from the expression:

$$\lambda = E(\mathbf{R_D}, n^D(\mathbf{r})) - E(\mathbf{R_A}, n^D(\mathbf{r})) \tag{7.33}$$

Here, n^D refers to the charge density distribution when the electron is localized on the donor. While $\mathbf{R}_D$ means the minimum energy geometry when the electron is localized on the donor. $\mathbf{R}_A$ is the minimum energy geometry when the electron is localized on the acceptor. Therefore the second term is the energy with the structure in the acceptor's geometry, but the charge distribution held in the donor state configuration.

7.5.2 Coupling Matrix Element

The electronic coupling describes the probability of an electron tunneling through a potential barrier across to the other side of the molecule. It was defined as:

$$V_{RP} = \langle \Psi_R | H | \Psi_P \rangle \approx \langle \Phi_R^{SD} | H | \Phi_P^{SD} \rangle \tag{7.34}$$

where the replacement of Ψ, the many-body all-electron wave-function, with Φ^{SD} the Slater determinants on single-electron wave-functions, is an approximation. Calculating this quantity is far harder. In a conventional DFT code, the single electron wave-functions are readily available. These can then be combined into a Slater Determinant and used to calculate the expression above via matrix multiplication. Van Voorhis showed that by re-writing this expression in a 'suggestive form', the coupling between two states with a different Hamiltonian can be calculated [131]. It was then shown that this can be used be used to shift to an adiabatic frame of reference and that this then gives the actual electronic coupling as outlined in chapter 6.

$$\langle \phi_R^{SD} | H | \phi_P^{SD} \rangle = \langle \phi_R^{SD} | H + w_c V_c | \phi_P^{SD} \rangle - \langle \phi_R^{SD} | w_c V_c | \phi_P^{SD} \rangle \tag{7.35}$$

However in a linear scaling code the energy is formulated purely in terms of the density and density matrix and the wave-functions are not readily available. Therefore this approach cannot be easily used. There are a number of possible ways to work around this. Whilst the wave-functions are not readily available, there is a basis set being used - the support functions - that could be used to project out the wave-function and then build a Slater Determinant at the end of the calculation. This is a somewhat brute force method. A more interesting problem is whether the coupling matrix element can be extracted using only single-particle density matrices. However, the linear scaling DFT formalism uses the single-particle density matrix, not the full many-body density matrix and so cannot be used in this formula. Work on this aspect is currently being continued.

$$\begin{aligned} V_{RP} = |\langle \Psi_R | H | \Psi_P \rangle|^2 &= \langle \Psi_R | H | \Psi_P \rangle (\langle \Psi_R | H | \Psi_P \rangle)^\dagger & (7.36) \\ &= \langle \Psi_R | H | \Psi_P \rangle \langle \Psi_P | H | \Psi_R \rangle & (7.37) \\ &= \mathrm{Tr}[\rho_R H \rho_P H] & (7.38) \end{aligned}$$

This chapter has outlined the methodology of linear scaling DFT and constrained DFT. The aspects particular to the implementation of constrained DFT within the linear scaling DFT code CONQUEST have been described and some initial benchmarking presented. In the following chapter some studies using this methodology are carried out on small molecules as preparation for larger scale studies.

Chapter 8

Constrained DFT Results

8.1 Introduction

In this chapter cDFT is used to perform electron transfer calculations on some physically interesting systems. Two types of electron transfer process were identified in chapter 6. Those involving an unpaired electron transferring from one sub-unit to another and those involving charge separation and recombination in a neutral system. For both of these cases, this chapter will consider the transfer as a discrete hop. A different system illustrating each case will be investigated with a final section showing calculations performed on porphyrin molecules similar, to those in chapters 3 and 5. The ultimate aim of a linear scaling implementation is to perform large scale electron transfer calculations on interesting biological or technologically relevant surface-molecule systems. However the application of linear scaling calculations is not straightforward and calculations on large systems are challenging to perform. Care must be taken choosing the system to be studied and it is important to identify the relevant physical and chemical questions to be answered, in order to assess what a linear scaling cDFT calculation can contribute. Therefore, due to the limited time available, as a first step the calculations here are performed on small molecules which make up some large scale systems that are ultimately of interest. Calculations on large systems will be performed in future work.

8.2 Methods

Calculations are performed using CONQUEST and the implementation of cDFT outlined in the previous chapter. The Becke weight method is used to determined the atomic populations for the constraint. In all calculations a double-zeta+polarization pseudo atomic orbital (PAO) basis set used with one PAO to each support function. A PBE exchange-correlation functional [138] is used. As the molecules are small, calculations are performed using exact diagonalization, rather than $\mathcal{O}(N)$ minimization, as this is more efficient for small systems. The geometries were allowed to relax until forces were less than 0.01 eVÅ^{-1}.

8.3 DNA Base Pairs

8.3.1 Introduction

DNA is one of the most important molecules in nature and the discovery of its double helix structure [139] is one of science's most celebrated achievements. Recently, DNA molecules have begun to attract attention from the perspective of molecular electronics and electron transfer [140, 141]. The reasons for the interest in DNA is two-fold. The first is from a structural standpoint. DNA is able to self-assemble into a number of structures, the most prominent of which is the double helix. Thanks to DNA's molecular selectivity, these helices could act as templates around which 1-D charge carrying structures could be built [142, 143]. Secondly, it is possible that DNA itself could intrinsically act as a very good charge transporter. The π-stacking of DNA base pairs down the backbone of the helix is potentially a pathway through which electrons can transfer down the molecule [144, 145]. This is evidenced by the observation of oxidative damage to DNA occurring via the transfer of holes up to 200 Å along the strand [146]. Both templating and intrinsic transport have something in common with the Mn nanolines investigated in chapter 4.

Consequently there has been a much work investigating the transport properties of DNA, both experimentally and theoretically. However, experimental estimates for the resistivity of long range charge transport in DNA have varied hugely and there is no definitive consensus on DNA's charge transport properties [147]. This is primarily

due to the challenges in the experimental set-up of these measurements [148, 149]. If experiments are performed on dry DNA, it is possible that the absence of surrounding solvent greatly influences the results. When experiments are performed in solution, technical issues can often result in DNA strands being stretched or deformed during measurement. This results in the overlap of the base pairs in the stack widening and thus the transfer being made less efficient. There is consensus on some aspects of DNA charge transport. It is usually agreed that charge transfer is primarily hole based and that the hole is likely to traverse through the strand via the HOMO of the guanine bases which have a particularly low ionization potential [150]. It has also been found that transfer in DNA is dependent on the concentration of guanine molecules [151].

8.3.2 This Study

As experiments are challenging to perform, there has been a push to study charge transport in DNA using theoretical and computational methods. However studying these systems computationally is also challenging, due to the large number of atoms which constitute DNA strands. As guanine molecules have the lowest ionization potential of the bases in a DNA strand, charge transfer is often mediated primarily by transfer between these bases. Electron transfer involving guanine molecules is therefore pertinent to the study of the DNA charge transport and is a good small scale starting point that can provide insight into the overall process.

Recent work by Parrinello *et al* [152], looked at hole localization within guanine dimers for this reason. The simulations studied positively-charged co-facial guanine dimers, as in figure 8.1 and calculated the binding energies using DFT. They found that the hole delocalized across both molecules. Then calculations were performed again with a fully self-interaction corrected (SIC) DFT implementation and the change in binding energy investigated. In this section similar simulations are performed, however instead of a SIC method, cDFT is used to impose localization of the hole within the charged dimers. By imposing a constraint, the hole wave-function is forced to localize on one of the bases and the change in binding energy from the unconstrained case calculated. This is repeated for dimers of each of the four DNA bases. This system serves as an example of charge localization in an approximately symmetric system. The con-

straint imposed simply asks there to be one fewer charge on one dimer than the other. Other types of constraint could have been chosen, such as forcing the electron onto a specific atom or part of the molecule. However, apart from at very small separations, this should not effect the trend of the binding greatly, which is likely to be dependent simply on whether the charge is shared equally or not. Using a constraint of this form also allows better comparison with the SIC results of [152].

In the study here, DFT calculations were performed of both a neutral and positively charged isolated guanine molecule, to find the equilibrium geometry of each one. These two molecules were then put together in a co-facial dimer, separated by either 2.5 Å, as shown in figure 8.1, or 6 Å. The simulations were performed in box with a 20Å z dimension, so that the separation between periodic images of the guanine molecules was always at least 14 Å. The dimers' geometries were kept constant during the calculations and binding energies was calculated for both the DFT and cDFT methods at the two different separations, using the following formula. This gives a positive energy as a binding interaction and a negative energy as a repulsive interaction.

$$\Delta E_{\mathrm{Bind}} = E^{\mathrm{DFT}}_{\mathrm{cation}} + E^{\mathrm{DFT}}_{\mathrm{neutral}} - E^{\mathrm{DFT\backslash cDFT}}_{\mathrm{dimer}} \tag{8.1}$$

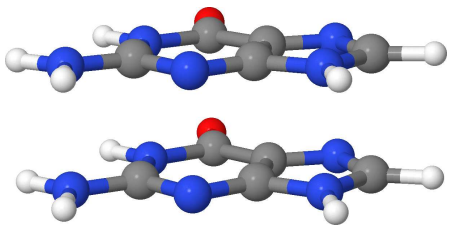

Figure 8.1: Geometry of positively charge guanine dimer.

8.3.3 Results

The binding energy for a positively charged guanine dimer separated by 2.5Å calculated using the DFT method is shown in table 8.1 as -2.321eV, a repulsive interaction. The charge difference between a neutral guanine dimer and this positively charged dimer, calculated using the DFT method, is plotted in figure 8.2(a). It shows that the hole is distributed symmetrically across the whole dimer and does not localize on the molecule

with the cation geometry when using this method. The cDFT method was then used to force the hole to localize on the cation guanine base within the dimer. The binding energy was then recalculated and is also shown in table 8.1 as -3.410eV. A plot of the charge difference between the neutral dimer and the constrained system is shown in figure 8.2(b). It clearly illustrates that the hole has been localized by the constraint. Calculations were repeated with other base dimers and at different separations. Binding energies for all the different cases are shown in table 8.1.

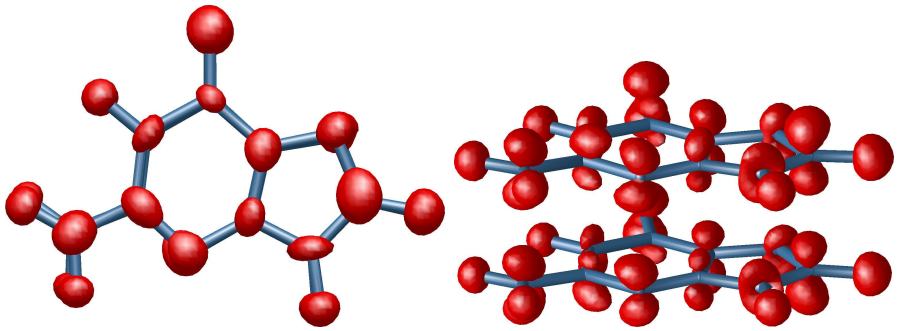

(a) DFT case

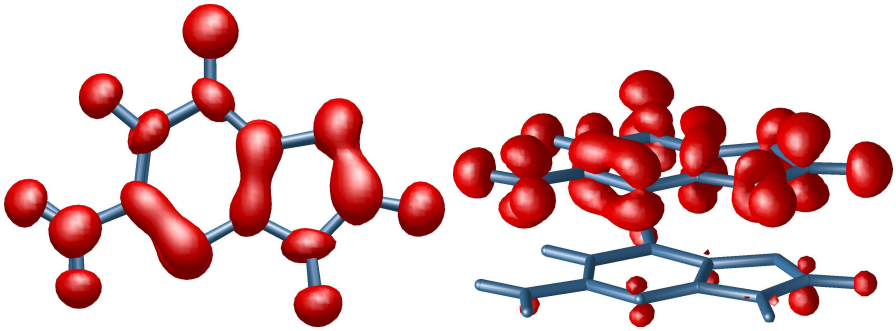

(b) cDFT case

Figure 8.2: (Negative) Charge difference density plot showing distribution of positive hole in a) DFT and b) when constrained to be on the upper guanine. In the figure, these molecules are 2.5 Å apart.

8.3.4 Discussion

These results show that when cDFT is used to localize a hole in DNA base dimers it produces energy changes which are often similar to those from fully self-interaction corrected methods. Although cDFT does not always give a similar binding energy, it always move the result in the correct direction. In general at short separations, the cDFT method moves results closer to those from the B3LYP method. At large separations,

cDFT produces results more like those of a SIC corrected method. Overall the results indicate that some of the important physical characteristics of a system can be corrected or captured by correcting the charge distribution in this way. These calculations were performed without allowing the structures to relax, in order to compare with a previous work. It is possible that exact nature of the binding depends on the geometric changes that occur when the electron is localized, particularly when the molecules are closer together. Furthermore, the two guanine molecules, particularly at small separations may interact and this too may affect the geometry. In future the effect of geometry relaxation could be investigated. However, for the well-separated dimers, where the delocalization error is greatest, this should be small. cDFT is not as useful for finding the actual electronic state of a system. In effect the state would have to be known for cDFT to be able to specify it exactly. It is unlikely that a general constraint can be applied and then cDFT used to find the exact electronic state from this reduced charge configuration space. However, as described in chapter 6, it is hoped that many of the important physical and chemical characteristics can be captured using just a general constraint and this study gives an indication to that effect. Extending this study to look at a larger strand of DNA is another avenue to be explored. Seeing how the change

Table 8.1: Binding energies for positively charged DNA base dimers. Application of a constraining potential is found to bring the energies closer to the SIC values. B3LYP and SIC values are from ref [152].

		Binding Energy (eV)			
Molecule	Separation (Å)	DFT(PBE)	cDFT	DFT(B3LYP)	SIC
Adenine	2.50	-1.084	-2.019	-3.533	-3.450
	6.00	0.848	0.094	0.677	-0.182
Guanine	2.50	-2.321	-3.410	-3.936	-4.418
	6.00	0.691	-0.082	0.538	0.030
Cytosine	2.50	-0.308	-1.558	-2.348	-6.440
	6.00	1.001	0.015	0.812	0.017
Thymine	2.50	-3.421	-4.564	-5.477	-6.302
	6.00	0.955	0.102	0.625	0.013

in binding energy brought on by the localization of the hole is affected by other bases and surrounding solvent, is relevant to understanding how the charge is transferred in reality. CONQUEST has been used previously to investigate DNA molecules [153] and adding a constraint to these types of calculations would be interesting.

8.4 Charge Separated Biphenyls

8.4.1 Introduction

As outlined in chapters 1 and 6, the field of molecular electronics [30] is becoming increasingly important. Owing to the ever decreasing size of electronic devices, a fundamental limit will soon be reached beyond which conventional silicon devices cannot be miniaturized any further [16]. Molecular electronics has attempted to create many analogues of conventional electronic components, such as transistors [154], wires [155] and switches [29] in a bid to overcome the eventual limits of conventional silicon electronics. The ultimate aim is to construct functional information processing and storage devices on a molecular scale.

One of the most sought after components is a molecular switch [29]. Switches are used in many electronic systems to process or store information. The principle idea is to find a system that can be quickly and reversibly switched between two bi-stable states, which have different conductive or transport properties. Many attempts have been made to produce such devices, for example [156–158]. These molecular switches can operate in many different ways. They can utilize electric fields, mechanical force, (for example STM) or chemical changes, to change the transport properties of the molecule. As when studying DNA there are particular experimental difficulties. One of these is that the properties of the molecule are determined not only by its own electronic structure, but also that of the leads to which it is coupled and any surrounding solvent or environment. The interplay between the structural and electronic properties of the system is extremely complicated and difficult to understand in many experimental situations. Theoretical modelling and computational simulation therefore have a large role to play in helping to identify or design suitable systems.

8.4.2 This Study

One way of switching molecular devices is via the application of light. So called photo-switches, in which there is a 'reversible photo-induced transformation between two molecular states' are extremely sought after [159] and many prototype devices have been reported, for example [160, 161]. One recent study [162] looked at three bi-phenyl molecules, shown in figure 8.3, and the conformational changes that occur in them upon photo-excitation. It was experimentally observed that upon photo excitation, the molecules became charge separated. The right hand end, the benzonitrile, was found to act as an electron acceptor, while the left hand end, the dimethylaniline, became a positive electron donor. This charge separation induced a structural change in the molecule's dihedral angle ϕ. The experiments investigated the twist potential of the three molecules. That is, the change in energy as a function of the dihedral angle. Molecule I is rotationally restricted, but the others are free to rotate and have a clear twist potential. In [162], the ground state twist potential of molecule II was found to have a minimum at 39° while molecule III had a minimum at 78°. When the molecules were photo-excited to a charge separated state, the equilibrium angles were found to change to 0° for molecule II and 40° for molecule III. This change in geometry caused by photo-excitation could effect the transport properties of these molecules. The ideas of a change in conformation upon application of light, give the molecules potential to act as the molecular photo-switches outlined above.

In the work here, the ground state twist potentials are calculated using DFT. Then the cDFT method is used to create the charge separated state in these molecules II and III, and the geometry changes occurring in ϕ are investigated. This enables the assessment of whether the structural changes occurring upon charge separation in these systems can be accurately captured using constrained density functional methods. The constraint imposed here, splits the molecules in half between the two benzene rings. Then it imposes that there is one net negative charge on the right hand side and one net positive charge on the left hand side. Thus a charge separated state akin to that seen in the experiment is created. Other constraint could have been chosen, such as choosing to constrain the electron to specific atoms at either end of the molecule. However, it is not clear which atom the electron and hole should be localized on and this simple left-right

charge separation across the centre of the molecule, ought to capture the main effects in any case. However, the changes caused by using different constraints or population schemes could also be investigated in future work.

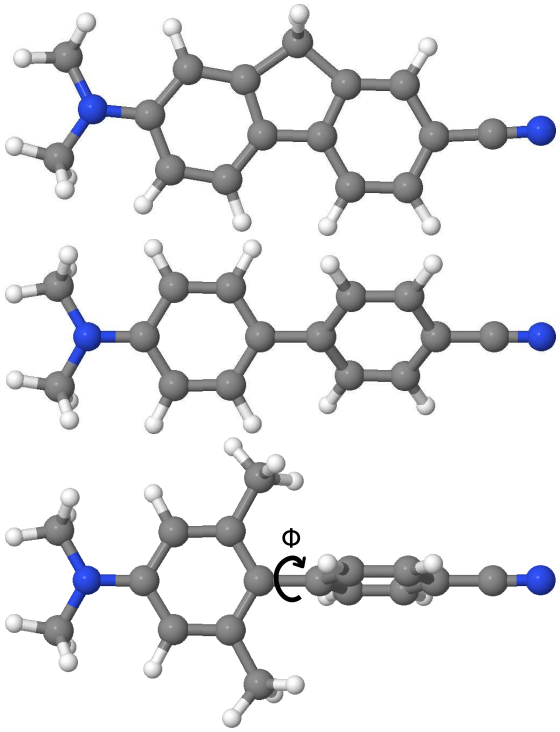

Figure 8.3: The structure of the three biphenyls used in the simulations here and ref. The first compound (I) is rotationally restricted. Compound II has a ground state equilibrium twist angle of 39° and compound III a twist angle of 78°.

8.4.3 Results

Twist potentials were created by fixing the atoms defining the dihedral angle ϕ at 10° intervals and allowing the other atoms in the molecule to relax. Figure 8.4 shows the ground state twist potentials calculated using standard DFT. They are extremely shallow, agreeing in magnitude with AM2 calculations of [162], but the results are well enough converged to provide at least a qualitative indication of the ground state angle and agree well with the calculations of [162]. It is clear that DFT can produce accurate ground state geometries for these compounds, as would be expected.

cDFT was then used to create the charge separated distribution. The twist potential for this state is shown in figure 8.5. The potential is now much deeper, which again

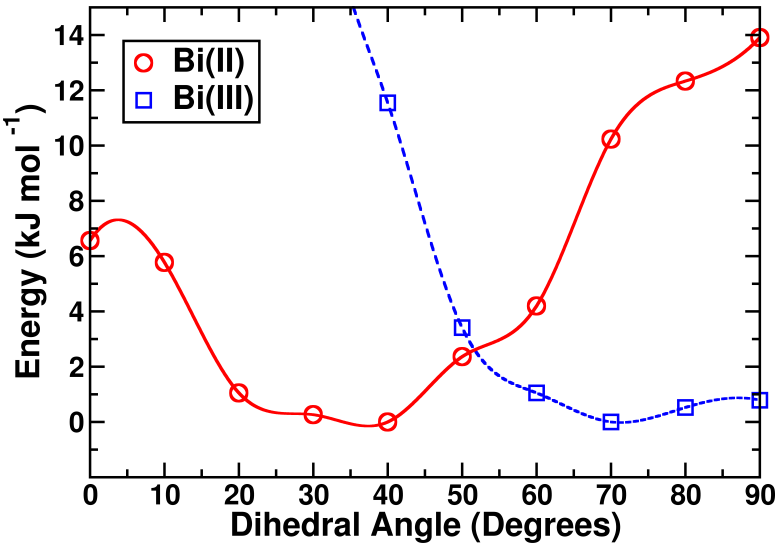

Figure 8.4: The twist potential for the ground state of biphenyl II (Red Line) and biphenyl III (Blue Line). Produced using standard DFT.

agrees with the experimental results of [162]. However more importantly, there is a clear change in the equilibrium angle in both the cases. These equilibrium angles have reduced to values approximately in agreement with the experimental work. This is an encouraging result that demonstrates that even though the electronic state of a system cannot be specified exactly by cDFT, important geometrical changes of the system are reproduced, using just the general constraint of a positive charge on one half of the molecule and a negative charge on the other. The difference in charge between the DFT and cDFT charge distributions are plotted in figures 8.6 for BiII and 8.7 for BiIII. These illustrate where the constraint adds and removes charge as compared to the ground state.

Table 8.2: Change in twist angle when charge is separated in 3 different biphenyl complexes.

	Twist Angle (ϕ)			
Molecule	AM2(G.st)	Expt (CS.St)	DFT(G.St)	cDFT(CS.St)
I	0°	0°	0°	0°
II	39°	0°	35°	8°
III	79°	36°	75°	41°

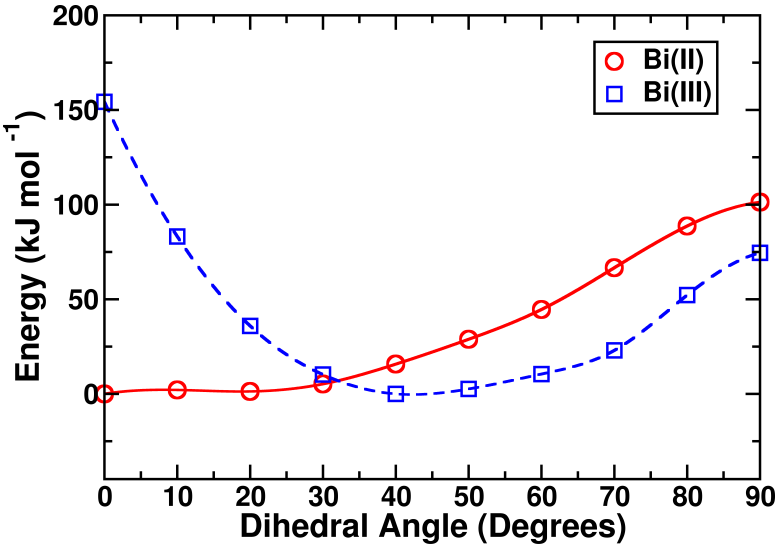

Figure 8.5: The twist potentials for charge separated state of biphenyl II (Red Line) and biphenyl III (Blue Line). Produced using constrained DFT.

The structural changes found upon upon charge separation can be used to calculate the reorganization of this electron transfer event. The reorganization energy is calculated from the following expression, as outlined in chapter 7.

$$\lambda = E(\mathbf{R_D}, n_D) - E(\mathbf{R_A}, n_D) \tag{8.2}$$

The energy differences between ground different electronic states at the different geometries are shown in table 8.3.

Table 8.3: Change in energy for ground state and excited state for the two compounds. This enables calculation of the reorganization energy.

	Energy Relative To Compounds' Ground State (kJ mol^{-1})				
Molecule	ϕ_{Eq}	$\phi = 0°$	$\phi = 90°$	$\phi = 0°$	$\phi = 40°$
II	40°	6.50	13.90	6.50	-
III	70°	88.95	0.79	-	11.55
	Energy Relative To Compounds' Excited State (kJ mol^{-1})				
Molecule	ϕ_{Eq}	$\phi = 0°$	$\phi = 90°$	$\phi = 40°$	$\phi = 70°$
II	0°	0	101.32	15.74	-
III	40°	154.29	74.52	-	22.99

From the two right-most columns in table 8.3, the reorganization energies of the

charge separation in the two molecules can be calculated. These are, 11.12kJmol^{-1} for molecule II and 17.27kJmol^{-1} for molecule III. The larger reorganization energy for molecule III is expected due to the larger number of atoms in the system. Here the reorganization energy for the separation event and recombination event have been averaged. That is $\lambda_{II} = \frac{6.50+15.74}{2} = 11.12$kJmol^{-1} and $\lambda_{III} = \frac{11.55+22.99}{2} = 17.27$kJmol^{-1}. The separation and recombination reorganizations differ by around 10kJmol^{-1} in each case, as the two states are not exact diabatic states of the system, as described in chapter 6. In both cases the cDFT results give the reorganization from the charge separated state as larger than that from the neutral state. This arises from the sharper diabatic surface produced by cDFT for the charge separated state of the biphenyl molecule.

These cDFT values are similar in magnitude to those found by [162]. There, adsorption and fluorescence measurements gave values of 1000cm^{-1} (11.96kJmol^{-1}) and 2000cm^{-1} (23.93kJmol^{-1}) for molecules II and III respectively. Alternatively, figures can be calculated from their graphs, figures 6 and 9 in [162], which give values of approximately 8.6kJmol^{-1} and 16.0kJmol^{-1} for molecules II and III. It would be interesting to investigate what effect the absence of a solvent has on the cDFT calculation. A solvent may well damp the energetic penalty to changing the geometry without transferring the electron. This is indeed the case when comparing the results in the experimental paper for the molecule III in different solvents.

8.4.4 Discussion

This study has shown that the straight forward constraints used in a cDFT calculation can enable some important structural properties of charge separated systems to be reproduced. The good reproduction of the structural changes for this system, indicates that in this case these are determined by 'broad' features, such as orbitals of charge interacting with each other resulting in a certain equilibrium angle. These orbitals clearly interact differently when charge is separated across the molecule. Again, it should be emphasized that the electronic state is not necessarily reproduced accurately. The excited states for small molecules can actually be written down in some cases and determined by symmetry arguments. Although unable to do this, cDFT can still capture the essential features and geometric results and this will prove very useful.

Figure 8.6: Charge difference plots for biphenyl II at the excited state equilibrium twist angle. Created by taking the difference (cDFT - DFT) between the charge distributions. Yellow shows areas of excess charge, blue shows areas of charge depletion.

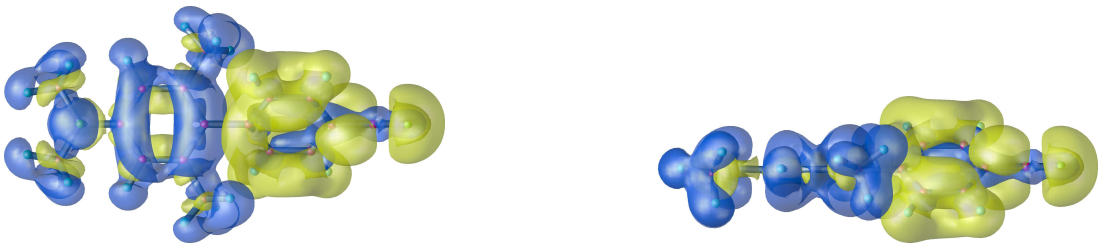

Figure 8.7: Charge difference plots for biphenyl III at the excited state equilibrium twist angle. Created by taking the difference (cDFT - DFT) between the charge distributions. Yellow shows areas of excess charge, blue shows areas of charge depletion.

There are some interesting avenues down which to extend this work. In particular, experimental results were performed with the molecule in a variety of solutions as well as in vacuum (the results compared with are those from in vacuum experiments). The solvent appeared to have an effect on the equilibrium dihedral angle of the charge separated molecule. It would be interesting to perform a large scale constrained molecular dynamics calculation of the biphenyl surrounded by the solvent and to see if the effects of the solvent could be accurately investigated. This would be a great aid in determining whether DFT and cDFT are accurate in these cases. This is important as many interesting biological systems are surrounded by solvent and this can often have a crucial role in the ET properties. If cDFT can capture this then these systems can be investigated more thoroughly and whether or not the solvent is crucial for mediating ET in certain cases, determined. When including solvents, free energies become very important and other cDFT implementations focus primarily on this aspect [137].

8.5 Electron Transfer In Porphyrin Molecules

8.5.1 Introduction

The final section of this chapter draws different elements of the thesis together by applying constraints to porphyrin molecules similar to those studied in chapters 3 and 5. The aim is to demonstrate the different types of calculation that may be useful when investigating electron transfer in porphyrin molecules on surfaces. The principle system studied in this chapter is the Magnesium porphyrin. These molecules, along with the similar Zinc porphyrins, have attracted interest due to the important role they play in the process of photosynthesis within both bacteria and plants [163, 164]. They have been considered as promising for use as the active component in artificial solar cells [8] or charge transport devices [26]. The photosynthetic systems that contain these porphyrins are large complicated systems, which a linear scaling application of cDFT would be suited to studying. Here, Magnesium porphyrins are studied under a variety of physically motivated constraints and the changes in energetics investigated.

8.5.2 Charge Separation in MgPor-Por

Charge separation is an important process in the photosynthetic reaction centre of plants and bacteria [164]. Zinc and Magnesium porphyrins are important constituents of these biological systems and therefore charge separated porphyrin dimers are of interest. The potential for them to be used in artificial solar cells, has resulted in much investigation of these systems. In this section the charge separated $MgPor^{+}$-$FbPor^{-}$ dimer, is created using constrained DFT and its energy calculated at various separations R, the distance between the nearest Carbon atoms of the two rings, shown as the equilibrium value 5.87Åin figure 8.8. The correct $\frac{1}{R}$ dependence is observed as the distance between the two molecules is varied, figure 8.8. The difference in energy between the ground state and charge separated state is $\Delta E = 5.133(3.75)$ eV for $MgPor^{+}$-$FbPor^{-}$ and $\Delta E = 5.579(3.94)$ eV for $MgPor^{-}$-$FbPor^{+}$. Bracketed values indicate the energy differences found in [35] for a charge separated ZnBC-BC (where BC is a Bacteriochlorin) complex. The charge difference plots figure 8.9, for the lower energy state $MgPor^{-}$-$FbPor^{+}$, show where the charge has been lost and gained in the two cases. This is not symmetric due to the difference of a FbPor and a MgPor. These results show that the

electron-hole interaction is being described correctly in the system. This is something that methods such as TDDFT fail to capture correctly [35].

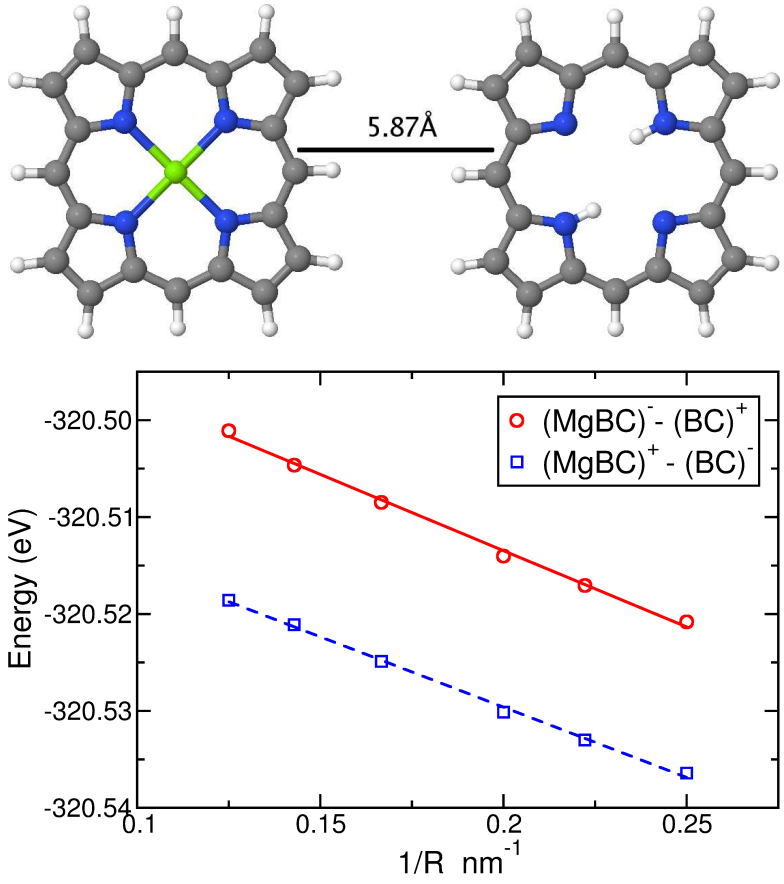

Figure 8.8: Top: Structure of the MgPor-Por compound studied. Equilibrium separation was found to be 6Å. Bottom: Graph showing the change in energy as the distance between the charge separated compounds is changed. The correct $\frac{1}{R}$ dependence is observed.

The porphyrins in these dimers are sometimes joined together by a bridge, for example a benzene ring or other conjugated molecule. The conjugated electrons of the bridge are then expected to mediate charge transfer between the two molecules. In other cases, some systems have porphyrins bound directly to each other. Porphyrins are bonded into tape structures with the aim of creating a system that will support charge transfer over long distances [24]. These tape-porphyrin systems are considered in the next section.

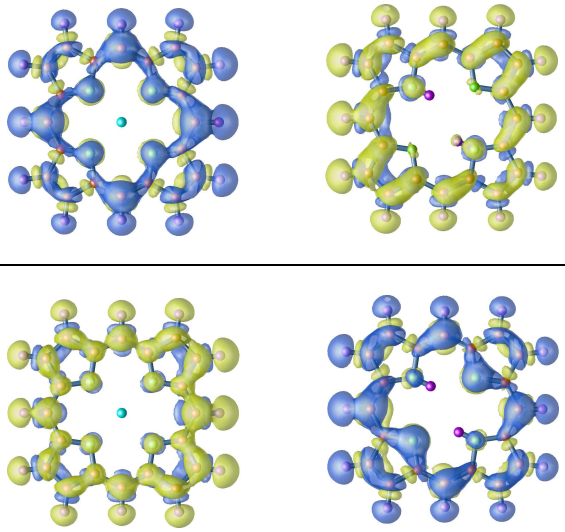

Figure 8.9: Charge difference plots for $MgPor^{+}$-Por^{-}(top) and $MgPor^{-}$-Por^{+} (bottom). These are obtained by subtracting the charge separated charge distribution from the neutral molecule charge distribution. Yellow shows areas of excess charge and blue areas of charge depletion.

8.5.3 Charge Localization in Tape Porphyrins

Tape porphyrins have been studied recently as they possess a number of potential uses, both as transport devices [24] and as molecular sensors [165]. Transport along a tape porphyrin requires excess charge to be present and travelling through the system. The transport of this excess charge may be band-like or hopping. Constrained DFT simulations could give some indication as to which mode is more prevalent by looking at whether there are large energetic barriers or structural changes, required for the charge transfer. When adding an extra electron to a tape structure, it will delocalize across the whole system when treated with conventional DFT, as in the guanine dimer. It is interesting to see the effect of the charge localizing onto one of the porphyrin molecules.

First the bound porphyrin dimer of figure 8.10 was simulated in isolation. Figure 8.11(a) shows the charge difference between a neutral and negatively charged bound dimer, calculated using DFT. This illustrates the delocalization of the electron across both molecules. There is some charge on the central of the three bonds joining the porphyrin, however most is pushed to the opposite ends of the molecule, reflecting

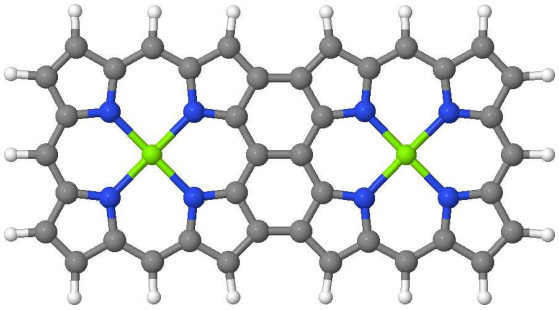

Figure 8.10: The structure of two molecules of a tape porphyrin. This molecule was simulated in isolation first and then periodically repeated to create a full tape porphyrin.

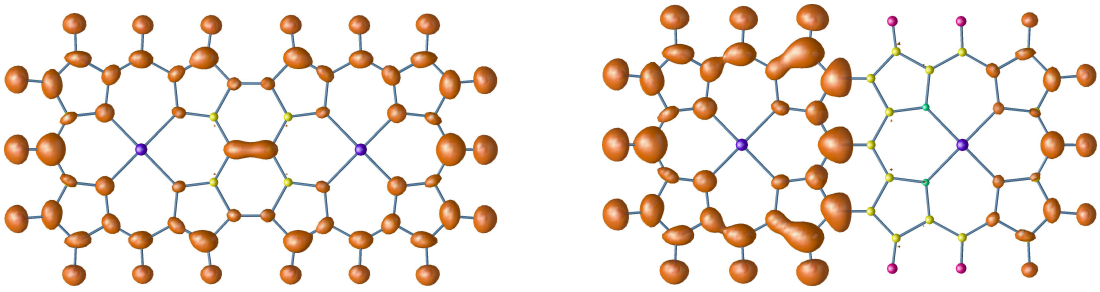

(a) Location of extra electron in negatively charged dimer, using DFT.

(b) Location of extra electron in negatively charged dimer using cDFT

Figure 8.11: Plots showing the location of the excess electron in a tape-porphyrin dimer.

the electrostatic repulsion between the electrons. In figure 8.11(b) a constraint has been applied to force the extra electron onto the left hand porphyrin. The adjacent neutral porphyrin clearly has an effect on the negatively charge porphyrin, as the charge distribution across it is not symmetric, as it would be for a negatively charged isolated porphyrin. The electron on the left hand porphyrin has also repelled charge repelled charge on the neutral porphyrin and forced some to move over to the far side of the molecule. Again this illustrates electrostatic repulsion. Periodic cells have long range electrostatic interactions as they are infinitely repeated. Excessive charge is neutralized using a positive background charge, however this does leave dipoles. There should not be a too large an effect, as a cell size was chosen to leave at least a 15 Å gap between this bound dimer and the next periodic image in each direction. Having seen that adjacent porphyrins affect each other and change the charge distribution from that of an isolated negative porphyrin, the question of an infinite chain of tape porphyrin

with a larger spacing between the donor and acceptor is investigated.

For this study a chain of three bound porphyrins is used and then a periodic cell is used to repeat the structure infinitely, as shown in figure 8.12. This three porphyrin periodic structure now has two neutral porphyrins between each negatively charged porphyrin. The neutral porphyrins of figure 8.12 are now not so strongly influenced by the adjacent charged porphyrin as those of figure 8.11(b) are compared. It is noted that in both the tape dimer and the full tape porphyrin, none of the additional electron is ever present on the central metal atom. This indicates that for the purposes of transport the macro-cycle is the important feature.

These calculations have all been performed statically. In the future it would be revealing to look at the structural relaxation occurring when the electron is localized. Self trapping can be an important feature of some conjugated systems such as polymers and may also play a role here.

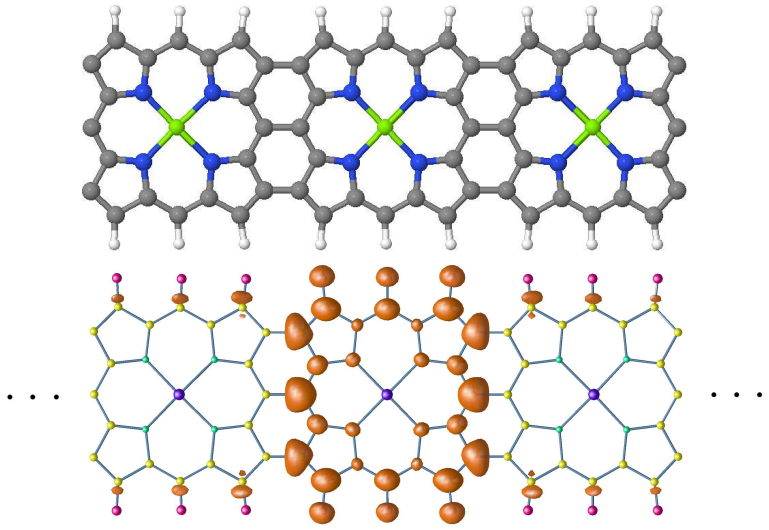

Figure 8.12: Upper panel: Structure of an infinitely repeated tape porphyrin. Lower panel: Charge difference between a DFT calculation and cDFT calculation of the negatively charged periodically repeated porphyrin chain. The excess electron is localized onto the central porphyrin.

8.5.4 Summary

This final section has illustrated the use of cDFT on porphyrin molecules. The charge separation in a separated porphyrin dimer was studied and shown to give a $\frac{1}{R}$ potential

energy curve between the two molecules, illustrating correct electron-hole interaction. Then a negatively charged bound porphyrin pair was studied and cDFT used to localize the extra electron onto one of the two porphyrins. The charge distribution this produced was not simply the same as a negatively charged porphyrin and a neutral porphyrin, due to the interaction between the two molecules. The localization of an electron within an infinite tape porphyrin was studied, and demonstrated that when the charged porphyrin was well-separated the electron constrained on it distributes as it would in an isolated porphyrin. In each case, the central atom played only a small role, never taking extra charge. This again indicates that the macrocycle is the most important conduit for charge transport in these systems. In the future the structural changes in these systems could be studied, in particular the self-trapping of electrons in tape porphyrins. Going further, studying tape porphyrins whilst they are on a surface and investigating the effect of the porphyrin constraint on the surface geometry would also be interesting. These are the kinds of large systems that a linear scaling implementation of cDFT is suited to studying.

8.6 Conclusions Electron Transfer Studies

In the second half of the thesis, constrained DFT has been implemented into a linear scaling DFT code. The code has been bench-marked and found to operate accurately in $\mathcal{O}(N)$ mode, using two different populations schemes. Using this implementation, some electron transfer calculations on small molecules were performed and illustrated accurate reproduction of some experimental and theoretical charge transfer and electron localization properties. Finally, some cDFT calculations on porphyrins were performed to demonstrate how these methods might be applied to the systems studied in the first half of the thesis. Together these results provide the ground work to enable electron transfer calculations to be performed on large systems with potential applications.

The implementation of cDFT into a linear scaling code is useful and important, as many interesting long-range electron transfer situations take place in large biological systems. In addition, many biological systems are surrounded by solvent and including this requires extra computational overhead. Large scale simulation of these systems will be important in identifying desirable features of potential systems. To simulate the

electron transfer in these situations is exciting and enables computational physics to make important contributions. cDFT provides an easily implemented, understood and executed method of addressing some specific problems and opening some new paths of work.

However, it is important to state that rarely is there a 'catch-all' method that will be superior in almost all situations. There are a number of implementations of cDFT available that themselves have specialized in particular areas, such as calculating the reaction barriers in small molecules [166], or the free energy changes in large systems [137]. The implementation here fits into a highly parallel linear scaling code with the potential to perform on extremely large systems, which should prove a useful addition to currently available codes. In addition to other cDFT implementations, there are numerous other approaches, to addressing electron transfer, such as time-dependent DFT and steady band transport in open systems, Non-Equilibrium Green's Function methods and first principles molecular dynamics [117] and others [115, 116]. These have made large contributions, as outlined in the introduction and will continue to do so. They offer more exact ways to treat certain situations and in particular are the only way to access a dynamic interpretation of electron transfer processes.

Many future simulations could be performed using the implementation of cDFT described here. Firstly systems built from the two small molecules studied in this chapter, such as large DNA systems surrounded by a solvent and large biphenyl derivatives coupled to leads, are of particular interest. However, another extension to this work is use the method to address electron transfer in surface systems. One potential avenue of investigation is to use cDFT to simulate the effect of charge separation in a molecule on a surface and the subsequent diffusion of the electron into the substrate. This is seen in dye molecules on TiO_2 which have been suggested as potential photo-voltaic devices.

As stated at the end of chapter 7 there is also much work to be done on theoretical extensions. Coupling matrix elements using single-particle density matrices for example. There are numerous other ways to correct some of the errors addressed by cDFT. One of the most prominent is the development of new functionals for the exchange and correlation. In particular functionals which aim to combat the self-interaction error such as self-interaction-corrected functionals [110] or hybrid functionals [45]. And

also those that aim to capture weak dispersive interactions such as van-der-Waals forces [167], which are prevalent in weakly bound systems. Further theoretical developments such as these would further enhance the method.

Chapter 9

Thesis Summary and Outlook

The desire to address a number of important technological problems has led to much study in the field of nanotechnology. Traditional surface science has already made an impact in a diverse range of applications such as detectors, catalysis, and microelectronics. The natural extension of some surface science techniques down to the nano-scale has allowed many potential technological advances, such as molecular wires, nano-scale magnetic storage, spintronic information processing devices, quantum computing, artificial photo-voltaic cells, improved catalytic materials and many more, to be explored. The computational study of nano-scale surface systems has played an important role within this. It has provided valuable guidance to current experiments, suggested future avenues for work and given insight into more speculative systems not yet amenable to experimental study. Within many of these potential device systems, the transfer of charge is an important feature and techniques studying this process are highly sought after. There has been much work focused on the computational simulation of electron transport processes in nano-scale systems, particularly those on surfaces.

This thesis has provided a framework within which the electron transfer properties of large molecules on surfaces may be investigated computationally and has done so in two parts. First, through a series of density functional studies on surface systems, which revealed the different binding regimes and assembly paradigms possible for atoms and molecules on silicon surfaces. And second, by the implementation and demonstration of the constrained density functional formalism within a highly parallel and linear scaling code, that enables electron transfer calculations to be performed on very large systems. By bringing the results and insights from these two aspects together,

new simulations of electron transfer in large surface systems can be performed. These simulations can then be used to provide insight into whether or not certain molecules are suitable required for nano-scale applications.

9.1 Surface Systems

In chapter 2 the basic formalism of density functional theory was presented. In chapter 3 a study of Haem(b) on the Si(111):H surface was performed and confirmed the weak nature of the interaction between porphyrin derivatives and hydrogen passivated surfaces. It was also found that this interaction could be marginally strengthened and the molecule-surface distance decreased, by creating a defect in the surface's hydrogen layer. The defect then acted as a favourable binding site for the molecule on the surface. Such tethering of molecules to silicon surfaces has been observed experimentally for phthalocyanines on the Si(001): and Si(111):H and could provide a method of directed assembly to create desired patterns of molecules. Throughout this chapter, the ideas of strengthening weak interactions via hydrogen desorption were emphasized.

Chapter 4 investigated the binding of Mn atoms at low coverages, to the Si(001) surface. In contrast to chapter 3, these systems bound very strongly to the surface. This caused them to induce structural rearrangements of the surface and bind cooperatively with each other at certain coverages and conformations. A structure of Mn atoms on the surface was proposed to explain the line-like structures recently observed in STM experiments on this system. The differences in comparison with chapter 3, now that the interaction between adsorbate and surface is strong, were highlighted. Specifically, how the strong interaction is linked to a mode of structure building that is now a more passive growth process. This results in the properties of the system changing upon, and being determined by, the adsorption.

Chapter 5 combined elements of the previous two chapters and investigated a manganese porphyrin (MnPor) on the clean Si(001) surface, a system which also has potential technological applications of its own. MnPor was found to bind strongly to the Si(001) surface and induce structural rearrangements of the surface, with the interaction varying greatly over different sites. This is in contrast to the weak dispersive binding seen for the molecule on some other surfaces. In chapter 3, DFT may not have been

capturing the full dispersive interaction between molecule and surface but in the case of the MnPor in chapter 5, much of the interaction appeared to be due to strong covalent bonding between the porphyrin ring and the surface. This is clearly a different binding regime to that of haem on the hydrogen terminated surface. The study also provides an indication that MnPor on Si(001) will have a preferable binding site, similar to the binding of a benzene ring on the surface, due to the lattice match. Individually, all three of these works also provide visual and structural interpretation to experimentalists working on these systems. Together they illustrate the effect of differing surface interaction strengths, on possible morphologies, construction methods and uses.

9.2 Electron Transfer

Chapter 6 outlined the Marcus theory of electron transfer to provide background to the following studies. Chapter 7 described the implementation of the constrained density functional formalism into the linear scaling DFT code CONQUEST. Technical issues were discussed, regarding population schemes, forces and convergence, pertaining specifically to implementation within a linear scaling code. Some benchmarking calculations were performed illustrating the codes operation. These showed similar population scheme behaviour to previous works and found a Becke weight population scheme to be the best suited for use in a linear scaling code. A brief description of how electron transfer parameters are extracted from cDFT calculations was then given and the difficulties faced in this regard by an $\mathcal{O}(N)$ implementation, pointed out. The implementation of cDFT in CONQUEST will allow linear scaling calculations of large systems to be performed. However due to the limited time available, as a first step, the following chapter featured calculations performed only on small molecules.

Chapter 8 used this implementation of constrained DFT to study charge localization and separation in three different small systems and compared the work to past experiments and theoretical calculations. Investigations were performed, studying the energetics of positively charged dimers of DNA base molecules, the structural rearrangements of charge separated biphenyl molecules and the charge separation and localization in Magnesium porphyrin molecules. The method was shown to work well for each of these systems, when compared with past cDFT calculations or experimental

work. With these results, larger scale simulations of systems based on these molecules can be performed with more confidence. Chapter 8 demonstrated that, following the work in this thesis, it is possible to perform large scale electron transfer calculations on molecules, such as the systems studied in the first half of the thesis. Some ideas for these future calculations were outlined in the relevant chapters and are recapitulated here.

9.3 Future Work: Combining The Two

The study of surface systems and electron transfer will remain important and challenging areas. Much experimental and theoretical work is needed to continue to design and improve potential devices and reach the stage where useful systems can be easily produced. From a theoretical standpoint, with regards linear scaling studies of electron transfer, a particularly useful development would be extraction of the electron transfer coupling matrix element from just single-particle density matrices. In addition, the recent advances in other cDFT codes such as the constrained computation of free energies and reaction barrier methods, will enable more calculations to be performed. In the wider context, density functional theory and indeed all computational methods, are continuously being developed and improved with attempts to increase their accuracy and efficiency always underway. These include new functionals, scaling behaviour and basis sets, that are accurate and allow rapid calculations in different situations. Many other methods will continue to provide important work, such as TDDFT and NEGF methods and all of these will hope to answer different questions in this area. These do not possess one of cDFT's main limitations, that it cannot easily provide a dynamical description of an electron transfer event. The question of exactly how a process will occur, cannot be answered easily by cDFT. Instead, fixed points must be picked that will be important in the process and these used to build up a picture and say something constructive about the transfer event.

There are also many potential simulations that can follow from the work here. In particular detailed investigations of the binding of metallopophyrins to dangling bonds on surfaces could be performed. For example, ascertaining the atomic physics behind the $3d_{z^2}$-$2p_z$ hybridization might reveal important features of the binding. However,

the most novel studies will involve looking at electron transfer in large systems. A particular example currently being investigated is the charge separation that occurs when a dye molecule is photo-excited on a TiO_2 surface. The electron from the electron-hole pair can subsequently diffuse into the surface and thus energy from a photon is converted into electrical energy and the systems operates as a solar cell. This work is currently being performed and forms part of a collaborative effort between the developers of CONQUEST and experimental groups. The behaviour of the charge separation while on the surface and the way in which the surface carries the electron away from the molecule, are important considerations in how such devices could work. A linear scaling implementation of cDFT is ideally suited to provide insight to these types of question. In addition $\mathcal{O}(N)$ calculations make including water and other solvents in calculations possible. This is important in calculations of a biological nature. Another potential study is to look at the transfer of a sodium ion through an ion channel. cDFT can be used to constrain the valence of the ion as it passes through this large solvated complex and the structural changes investigated. This may help reveal the structural and electronic features most important to the functioning of these systems. DNA molecules will also be of interest, these too can be effected by a surrounding solvent. Calculating the reorganization energy for these situations would enable assessment to be made of how important the solvent is in mediating electron transfer processes.

9.4 Closing Summary

The contribution of this thesis is to provide a framework within which large scale electron transfer calculations of molecular systems and surfaces can be performed. By investigating molecule-surface systems with differing binding strengths, the ways in which the interaction with a surface can be altered and tailored to purpose were identified. By implementing constrained density functional theory into an existing linear scaling density functional code, much knowledge has been gained about applying this method to these kinds of systems. The initial calculations performed help enable exciting new electron transfer calculations to be performed with confidence.

Bibliography

[1] J.V. Barth, G. Costantini, and K. Kern. Engineering atomic and molecular nanostructures at surfaces. *Nature*, 437(7059):671–679, 2005.

[2] G. Binnig and H. Rohrer. In touch with atoms. *Reviews of Modern Physics*, 71(2):S324–S330, 1999.

[3] John A. Venables. *Introduction to Surface and Thin Film Processes*. Cambridge University Press, 2000.

[4] D. Drakova. Theoretical modelling of scanning tunnelling microscopy, scanning tunnelling spectroscopy and atomic force microscopy. *Reports On Progress In Physics*, 64:205–290, 2001.

[5] M. Ternes, C.P. Lutz, C.F. Hirjibehedin, F.J. Giessibl, and A.J. Heinrich. The force needed to move an atom on a surface. *Science*, 319(5866):1066–1069, 2008.

[6] J. Lin, I.A. Balabin, and D.N. Berantan. The nature of aqueous tunneling pathways between electron-transfer proteins. *Science*, 310(5752):1311–1313, 2007.

[7] K.R. Harikumar, T. Lim, I.R. McNab, J.C. Polyani, L. Zotti, S. Ayissi, and W.A. Hofer. Dipole-directed assembly of lines of 1,5-dichloropentane on silicon substrates by displacement of surface charge. *Nature Nanotechnology*, 3:222–228, 2008.

[8] W.M. Campbell, A.K. Burrell, D.L. Officer, and K.W. Jolley. Porphyrins as light harvesters in the dye-sensitised TiO_2 solar cell. *Coordination Chemistry Reviews*, 248:1363–1379, 2004.

[9] J. Ryou, S. Hong, and G. Kim. Ab initio study of hydrogen binding on Ca-inserted porphyrin. *Vacuum*, 84(5):537–539, 2009.

[10] W. Fang, W. Feng, C. Shi, Q. XinPing, and C. LiQuan. A comparison of iron phthalocyanine and cobalt porphyrin on the electrochemical catalysis in Ni-MH battery. *Chinese Science Bulletin*, 52(1):71–77, 2007.

[11] A.D.F. Dunbar, T.H. Richardson, A.J. McNaughton, J. Hutchinson, and C.A. Hunter. Investigation of free base, Mg, Sn, and Zn substituted porphyrin LB films as gas sensors for organic analytes. *Journal of Physical Chemistry B*, 110(33):16646–16651, 2006.

[12] M. Mannini, F. Pineider, P. Sainctavit, C. Danieli, E. Otero, C. Sciancalepore, A. M. Talarico, M-A. Arrio, A. Cornia, D. Gatteschi, and R. Sessoli. Magnetic memory of a single-molecule quantum magnet wired to a gold surface. *Nature Materials*, 8:194–197, 2009.

[13] P.G. Piva, G.A. DiLabio, J.L. Pitters, J. Zikovsky, M. Rezeq, S. Dogel, W. Hofer, and R.A. Wolkow. Field regulation of single-molecule conductivity by a charged surface atom. *Nature*, 435:658–661, 2005.

[14] H. Wende, M. Bernien, J. Luo, C. Sorg, N. Ponpandian, J. Kurde, J. Miguel, M. Piantek, X. Xu, PH. Eckhold, W. Kuch, K. Baberschke, P.M. Panchmatia, B. Sanyal, P.M. Oppeneer, and O. Eriksson. Substrate-induced magenetic ordering and switching of iron porphyrin molecules. *Nature Materials*, 6:516–520, 2007.

[15] F.A. Buot. Mesoscopic physics and nanoelectronis: nanoscience and nanotechnology. *Physics Reports*, 234:73–174, 1993.

[16] M. Mathur. Nanotechnology: Beyond the silicon roadmap. *Nature*, 419:573–575, 2002.

[17] A. Kaur and U. Gupta. A review on applications of nanoparticles for the preconcentration of environmental pollutants. *Journal of Materials Chemistry*, 19:8279–8289, 2009.

[18] A. Szabo and N.S. Ostlund. *Modern Quantum Chemistry: Introduction to advanced electroinc structure theory*. Collier Macmillan Publishers, 1989.

[19] P. Hohenberg and W. Kohn. Inhomogeneous electron gas. *Physical Review*, 136(3B):B864–B871, 1964.

[20] W. Kohn and L.J. Sham. Self-consistent equations including exchange and correlation effects. *Physical Review*, 140(4A):A1133–A1138, 1965.

[21] A.J. Cohen, P. Mori-Sànchez, and W. Yang. Insights into current limitations of density functional theory. *Science*, 321:792–794, 2008.

[22] D. Dolphin, editor. *The porphyrins, Vol I-VII*. Academic Press Inc, New York, 1978.

[23] S. Heutz, C. Mitra, W. Wu, A.J. Fisher, A. Kerridge, M. Stoneham, A.H. Harker, J. Gardener, H-H. Tseng, T.S. Jones, C. Renner, and G. Aeppli. Molecular thin films: A new type of magnetic switch. *Advanced Materials*, 19(21):3618–3622, 2007.

[24] K. Tagami, M. Tsukada, T. Matsumoto, and T. Kawai. Electronic transport properties of free-base porphyrin molecular wires studied by self-consistent tight-binding calculations. *Physical Review B*, 67(24):245324, 2003.

[25] H. Nobukuni, Y. Shimazaki, F. Tani, and Y. Naruta. A nanotube of cyclic porphyrin dimers connected by nonclassical hydrogen bonds and its inclusion of C60 in a linear arrangement. *Angewandte Chemie International Edition*, 46:8975–8978, 2007.

[26] A.A. Kocherzhenko, S. Patwardhan, F.C. Grozema, H.L. Anderson, and L.D.A. Siebbeles. Mechanism of charge transport along zinc porphyrin-based molecular wires. *Journal of The American Chemical Society*, 131(15):5522–5529, 2009.

[27] W.A. Hofer and J. Redinger. Scanning tunneling microscopy of binary alloys: first principles calculation of the current for PtX(100) surfaces. *Surface Science*, 447:51, 2000.

[28] W.A. Hofer and J. Redinger. Challenges and errors: Interpreting high resolution images in scanning tunneling microscopy. *Progress in Surface Science*, 71:147, 2003.

[29] D. Feldheim. Nanotechnology: Flipping a molecular switch. *Nature*, 408:45–46, 2000.

[30] J.R. Heath and M.A. Ratner. Molecular electronics. *Physics Today*, May, 2003.

[31] R.A. Marcus. Electron transfer reactions in chemistry: Theory and experiment. *Journal of Electroanalytical Chemistry*, 438(1):251–259, 1997.

[32] M.A.L. Marques and E.K.U. Gross. Time-dependent density functional theory. *Annual Review of Physical Chemistry*, 55:427–455, 2004.

[33] J.R. Reimers, G.C. Solomon, A. Gagliardi, A. Bili, N.S. Hush, T. Frauenheim, A. Di Carlo, and A. Pecchia. The Green's function density functional tight-binding (gDFTB) method for molecular electronic conduction. *The Journal of Physical Chemistry A*, 111(26):5692–5702, 2007.

[34] P. H. Dederichs, S. Blgel, R. Zeller, and H. Akai. Ground states of constrained systems: Application to cerium impurities. *Physical Review Letters*, 53:2512–2515, 1984.

[35] T. Van Voorhis and Q. Wu. Direct optimization method to study constrained systems within density-functional theory. *Physical Review A*, 72(2):024502, 2005.

[36] S. Goedecker. Linear scaling electronic structure methods. *Reviews of Modern Physics*, 71(4):1085, 1999.

[37] R.G. Parr and W. Yang. *Density-Functional Theory of Atoms and Molecules*. Oxford Science Publications, 1989.

[38] R.M. Martin. *Electronic Structure: Basic Theory and Practical Methods*. Cambridge University Press, 2004.

[39] M.B. Ruskai and J.E. Harriman. N-representability problem for an odd number of fermions. *Physical Review*, 169:101113, 1968.

[40] W. Stich, E.K.U. Gross, P. Malzacher, and R.M. Dreizler. Accurate solution of the Thomas-Fermi-Dirac-Weizscker variational equations for the case of neutral atoms and positive ions. *Zeitschrift fr Physik A Hadrons and Nuclei*, 309(1):5–11, 1982.

[41] P. Pulay. Convergence acceleration of iterative sequences. The case of SCF iteration. *Chemical Physics Letters*, 73:393–398, 1980.

[42] G.P. Kerker. Efficient iteration scheme for self-consistent pseudopotential calculations. *Physical Review B*, 23:3082–3084, 1980.

[43] J. P. Perdew, K. Burke, and M. Ernzerhof. Generalized Gradient Approximation Made Simple. *Physical Review Letters*, 77:3865, 1996.

[44] J.P. Perdew, J.A. Chevary, S.H. Vosko, K.A. Jackson, M.R. Pederson, D.J. Singh, and C. Fiolhais. Atoms, molecules, solids, and surfaces: Applications of the generalized gradient approximation for exchange and correlation. *Physical Review B*, 46:6671, 1992.

[45] A.D. Becke. Density-functional thermochemistry. III. The role of exact exchange. *Journal of Chemical Physics*, 98:5648, 1993.

[46] A.D. Becke. Density-functional thermochemistry. II. The effect of the Perdew Wang generalized-gradient correlation correction. *Journal of Chemical Physics*, 97:9173, 1992.

[47] A.D. Becke. Density-functional thermochemistry. I. The effect of the exchange-only gradient correction. *Journal of Chemical Physics*, 96:2155, 1992.

[48] P. Pulay. Ab initio calculation of force constants and equilibrium geometries in polyatomic molecules. *Molecular Physics*, 17(2):197–204, 1969.

[49] P.E. Blochl. Projector augmented-wave method. *Physical Review B*, 50:17953, 1994.

[50] G. Kresse and D. Joubert. From ultrasoft pseudopotentials to the projector augmented-wave method. *Physical Review B*, 59:1758, 1999.

[51] V.I. Anisimov, I.V. Solovyev, M.A. Korotin, M.T. Czyzyk, and G.A. Sawatzky. Density-functional theory and NiO photoemission spectra. *Physical Review B*, 48:16929, 1993.

[52] S.L. Dudarev, G.A. Botton, S.Y. Savrasov, C.J. Humphreys, and A.P. Sutton. Electron-energy-loss spectra and the structural stability of nickel oxide: An LSDA+U study. *Physical Review B*, 57:1505, 1998.

[53] J. Bardeen. Tunnelling from a many-particle point of view. *Physical Review Letters*, 6(2):57–59, 1961.

[54] J. Tersoff and D. R. Hamann. Theory of the scanning tunneling microscope. *Physical Review B*, 31(2):805–813, 1985.

[55] G.A.D. Briggs and A.J. Fisher. STM experiment and atomistic modelling hand in hand: Individual molecules on semiconductor surfaces. *Surface Science Reports*, 33:1–81, 1999.

[56] J.P. Collman, R. Boulatov, C.J. Sunderland, and L. Fu. Functional analogues of cytochrome(c) oxidaze, myoglobin and hemoglobin. *Chemical Reviews*, 104(2):561, 2004.

[57] A.F. Riggs. Haemoglobins. *Current Opinions in Structural Biology*, 1:915, 1991.

[58] D.A. Scherlis, M. Cococcioni, P. Sit, and N. Marzari. Simulation of haem using DFT+U: A step toward accurate spin-state energetics. *Journal of Physical Chemistry B*, 111:7384, 2007.

[59] D. Khvostichenko, Q-Z. Yang, and R. Boulatov. Simple haem dimers with strongly cooperative ligand binding. *Angewandte Chemie*, 46:8368, 2007.

[60] P.M. Panchmatia, B. Sanyal, and P.M. Oppeneer. *Ab inito calculations of the electronic structure and magnetism of iron porphyrin-type molecules: A benchamrking study*. Springer Berlin / Heidelberg, 2007.

[61] M. Bernien, J. Miguel, C. Weis, Md.E. Ali, J. Kurde, B. Krumme, P.M. Panchmatia, B. Sanyal, M. Piantek, P. Srivastava, K. Baberschke, P.M. Oppeneer, O. Eriksson, W. Kuch, and H. Wende. Tailoring the nature of magnetic coupling of Fe-porphyrin molecules to ferromagnetic substrates. *Physical Review Letters*, 102:047202, 2009.

[62] M.P. Johansson, M.R.A. Blomberg, D. Sundholm, and M. Wikstrom. Change in electron and spin density upon electron transfer to haem. *Biochimica et Biophysica Acta*, 1553:183, 2001.

[63] D.M.A. Smith, K.M. Rosso, M. Dupuis, M. Valiev, and T.P. Straatsma. Electronic coupling between Heme Electron-Transfer Centres and its Decay with Distance Depends Strongly on Relative Orientation. *Journal of Physical Chemistry B*, 110:15582, 2006.

[64] L.A. Zotti, G. Teobaldi, W.A. Hofer, W. Auwarter, A. Weber-Bargioni, and J.V. Barth. Ab-inito calculations and STM observationson tetrapyridyl and Fe(II)-tetrapyridil-porphyrin moleucles on Ag(111). *Surface Science*, 601:2409, 2007.

[65] K. Leung, B. Rempe, P.A. Schultz, E.M. Sproviero, V.S. Batista, M.E. Chandross, and C.J. Medforth. Density functional theory and DFT+U study of transition metal porphines adsorbed on Au(111) surfaces and effects of applied electric fields. *Journal of The American Chemical Society*, 128(11):3659, 2006.

[66] A.J. Baldwin, R. Bader, J. Christodoulou, C.E. MacPhee, C.M Dobson, and P.D. Barker. Cytochrome display on amyloid fibrils. *Journal of The American Chemical Society*, 128(7):2162, 2006.

[67] S.Weigelt and C.Durkan. Private communication, 2008.

[68] M.C. Hersam, N.P. Guisinger, and J.W. Lyding. Silicon-based molecular nanotechnology. *Nanotechnology*, 11:70–76, 2000.

[69] M.C. Hersam, J. Lee, N.P. Guisinger, and J.W. Lyding. Implications of atomic-level manipulation on the Si(100) surface: From enhanced CMOS reliability to molecule nanoelectroincs. *Superlattices and Microstructures*, 27:583, 2000.

[70] G. Kresse and J. Hafner. Ab initio molecular dynamics for liquid metals. *Physical Review B*, 47:558, 1993.

[71] G. Kresse and J. Furthmuller. Efficient iterative schemes for ab initio total-energy calculations using a plane-wave basis set. *Physical Review B*, 54:11169, 1996.

[72] P.M. Panchmatia, B. Sanyal, and P.M. Oppeneer. GGA+U modeling of structural, electronic, and magnetic properties of iron-porphyrin type molecules. *Chemical Physics*, 343:47–60, 2008.

[73] V.I. Anisimov, J. Zaanen, and O.K. Andersen. Band theory and Mott insulators: Hubbard U instead of Stoner I. *Physical Review B*, 44:943, 1991.

[74] H. Peisert, T. Schwieger, J.M. Auerhammer, M.S. Knupfer, M.and Golden, J. Fink, P.R. Bressler, and M. Mast. Order on disorder: Copper phthalocyanine thin films on technical substrates. *Journal of Applied Physics*, 90:466, 2001.

[75] M. Lein, J.F. Dobson, and E.K.U. Gross. Toward the description of van der Waals interactions within density functional theory. *Journal of Computational Chemistry*, 20:12–22, 1999.

[76] M. Dion, H. Rydberg, E. Schrder, D.C. Langreth, and B.I. Lundqvist. Van der Waals density functional for general geometries. *Physical Review Letters*, 92:246401, 2004.

[77] O.A. Vydrov, A. Wu, and T. Van Voorhis. Self-consistent implementation of a nonlocal van der Waals density functional with a Gaussian basis set. *Journal of Chemical Physics*, 129:141106, 2008.

[78] W. A. Hofer, A. J. Fisher, G. P. Lopinski, and R. A. Wolkow. Adsorption of benzene on Si(100)-(2$\times$1): Adsorption energies and STM image analysis by ab initio methods. *Physical Review B*, 63(8):085314, 2001.

[79] W.A. Hofer, A.J. Fisher, and R.A. Lopinski, G.P. Wolkow. Benzene on silicon: Combining STM experiments with first principles studies. *Surface Science*, 482-485(Part 2):1181–1185, 2001.

[80] N. Papageorgiou, E. Salomon, T. Angot, L-M. Layet, L. Giovanelli, and G. Le Lay. Physics of ultra-thin phthalocyanine films. *Progress in Surface Science*, 77:139, 2004.

[81] A. Nilsson, L.G.M. Pettersson, and J. Norskov. *Chemical Bonding at Surfaces and Interfaces: pp72-74*. Elsevier, 2007.

[82] D.D. Awschalom and M.E. Flatt. Challenges for semiconductor spintronics. *Nature Physics*, 3:153–159, 2007.

[83] A.H. MacDonald, P. Schiffer, and N. Samarth. Ferromagnetic semiconductors: Moving beyond (Ga,Mn)As. *Nature Materials*, 4:195–202, 2005.

[84] D.R. Bowler. Atomic-scale nanowires: physical and electronic structure. *Journal of Physics: Condensed Matter*, 16:R721–R754, 2004.

[85] R.H. Miwaa, W. Orellanab, and G.P. Srivastavac. A theoretical study of Fe adsorption along Bi-nanolines on the H/Si(001) surface. *Applied Surface Science*, 254:96–98, 2007.

[86] K. Miki, D.R. Bowler, G.A.D. Owen, J.H.G. Briggs, and K. Sakamoto. Atomically perfect bismuth lines on Si(001). *Physical Review B*, 59:14868–14871, 1999.

[87] A. Zhao, Q. Li, L. Chen, H. Xiang, W. Wang, S. Pan, B. Wang, X. Xiao, J. Yang, J.G. Hou, and Q. Zhu. Controlling the Kondo effect of an adsorbed magnetic ion through its chemical bonding. *Science*, 309:1542, 2005.

[88] H. Wu, P. Kratzer, and M. Scheffler. Density-functional theory study of half-metallic heterostructures: Insterstitial Mn in Si. *Physical Review Letters*, 98:117202, 2007.

[89] H. Wu, M. Hortamani, P. Kratzer, and M. Scheffler. First-principles study of ferromagnetism in epitaxial Si-Mn thin films on Si(001). *Physical Review Letters*, 92:237202, 2004.

[90] M.R. Krause, A.J. Stollenwerk, J. Reed, V.P. LaBella, M. Hortamani, P. Kratzer, and M. Scheffler. Electronic structure changes of Si(001)-(2×1) from subsurface Mn observed by STM. *Physical Review B*, 75:205326, 2007.

[91] H. Liu and P. Reinke. Formation of manganese nanostructures on the Si(100)-(2×1) surface. *Surface Science*, 602:986, 2008.

[92] A.Z. AlZahrani, G.P. Srivastava, and R.H. Miwaa. Theoretical investigation of Mn adsorbates aside self-organised Bi nanolines on hydrogenated Si(001) surface. *Surface Science*, 602:2789–2795, 2008.

[93] M. Hortamani, H. Wu, P. Kratzer, and M. Scheffler. Epitaxy of Mn on Si(001): Adsorption, surface diffusion, and magnetic properties studied by density-functional theory. *Physical Review B*, 74:205305, 2006.

[94] G. Shao. Red shift in manganese- and iron-doped TiO2: A DFT+U analysis. *Journal of Physical Chemistry C*, 113(16):6800–6808, 2009.

[95] H. Gwon, D-H. Seo, S-W. Kim, J. Kim, and K. Kang. Combined first-principle calculations and experimental study on multi-component olivine cathode for lithium rechargeable batteries. *Advanced Functional Matrials*, 19:3285–3292, 2009.

[96] K. Kang, Y.S. Meng, J. Breger, and G. Grey, C.P. Ceder. Electrodes with high power and high capacity for rechargeable lithium batteries. *Science*, 311:977, 2006.

[97] M. M. R. Evans and J. Nogami. Indium and gallium on Si(001): A closer look at the parallel dimer structure. *Physical Review B*, 59(11):7644, 1999.

[98] Z.-C. Dong, D. Fujita, and H. Nejoh. Adsorption and tunneling of atomic scale lines of indium and lead on Si(100). *Physical Review B*, 63(11):115402, 2001.

[99] P. Reinke. Private communication, 2009.

[100] D. Rutkowska-Zbik, M. Witko, and E.M. Serwicka. Epoxidation of cyclohexene catalyzed by manganese porphyrins: Ab initio DFT studies. *Catalysis Today*, 91-92:137–141, 2004.

[101] D. Balcells, C. Raynaud, R.H. Crabtree, and O. Eisenstein. CH oxidation by hydroxo manganese(V) porphyrins: a DFT study. *Chemical Communications*, pages 1772–1774, 2009.

[102] S. Heutz. Private communication, 2008.

[103] Md. Ehesan Ali, B. Sanyal, and P.M. Oppeneer. Tuning the magnetic interaction between manganese porphyrins and ferromagnetic Co substrate through dedicated control of the adsorption. *Journal of Physical Chemistry C*, 113:14381–14383, 2009.

[104] S.R. Bishop, N.L. Tran, G.C. Poon, and A.C. Kummel. Dynamics of analyte binding onto a metallophthalocyanine: NO/FePc. *Journal of Chemical Physics*, 127:214702, 2007.

[105] N.L. Tran and A.C. Kummel. A density functional theory study of the binding of NO onto FePc films. *Journal of Chemical Physics*, 127:214701, 2007.

[106] H. Taube. *Nobel Lectures Chemistry 1981-1990: Electron Transfer between Metal Complexes - Retrospective*. World Scientific Publishing Co., 1992.

[107] R.A. Marcus. *Nobel Lectures: Electron Transfer Reactions in Chemistry: Theory and Experiment*. World Scientific Publishing Co., 1997.

[108] D. Devault. Quantum mechanical tunnelling in biological systems. *Quarterly Reviews of Biophysics*, 13(4):387–564, 1980.

[109] A. M. Stoneham. *Theory of Defects in Solids*. Oxford University Press, 1975.

[110] J.P. Perdew and A. Zunger. Self-interaction correction to density-functional approximations for many-electron systems. *Physical Review B*, 23:5048, 1981.

[111] A.J. Johansson, M.R.A. Blomberg, and P.E.M. Siegbahn. Quantifying the effects of the self-interaction error in density functional theory: When do the delocalized states appear? II. Iron-oxo complexes and closed-shell substrate molecules. *The Journal of Chemical Physics*, 129:154301, 2008.

[112] C. Toher, A. Filippetti, S. Sanvito, and K. Burke. Self-Interaction Errors in Density functional calculations of electronic transport. *Physical Review Letters*, 95:146402, 2005.

[113] P. Mori-Sanchez, A.J. Cohen, and W. Yang. Localization and delocalization errors in density functional theory and implications for band-gap prediction. *Physical Review Letters*, 100:146401, 2008.

[114] T. Van Voorhis and Q. Wu. Constrained density functional theory and its applications in long range electron transfer. *Journal of Chemical Theory and Computation*, 2(3):765–774, 2006.

[115] Y. Tateyama, J. Blumberger, T. Ohno, and M. Sprik. Free energy calculation of water addition coupled to reduction of aqueous RuO_4^-. *Journal of Chemical Physics*, 126(20):204506, 2007.

[116] J. L. Suter, E. S. Boek, and M. Sprik. Adsorption of a sodium ion on a smectite clay from constrained ab initio molecular dynamics simulations. *Journal of Physical Chemistry C*, 112:18832–18839, 2008.

[117] P.H.-L. Sit, M. Cococcioni, and N. Marzari. Realistic quantitative descriptions of electron transfer reactions: Diabatic free-energy surfaces from first-principles molecular dynamics. *Physical Review Letters*, 97:028303, 2006.

[118] E. Artacho, E. Anglada, O. Dieguez, J.D. GAle, A. Garcia, J. Junquera, R.M. Martin, P. Ordejon, J.M. Pruneda, D. Sanchez-Portal, and J.M. Soler. The SIESTA method; developements and applicability. *Journal of Physics: Condensed Matter*, 20:064208, 2008.

[119] C-K. Skylaris, P.D. Haynes, A. Mostofi, and M.C. Payne. Recent progress in linear-scaling density functional calculations with plane waves and pseuopoten-

tials: The ONETEP code. *Journal of Physics: Condensed Matter*, 20:064209, 2008.

[120] T. Ozaki and K. Terakura. Convergent recursive O(N) method for ab initio tight-binding calculations. *Physical Review B*, 64:195126, 2001.

[121] M.J. Gillan, D.R. Bowler, A.S. Torralba, and T. Miyazaki. Order-N first-principles calculations with the CONQUEST code. *Computer Physics Communications*, 177:14–18, 2007.

[122] E. Prodan and W. Kohn. Nearsitedness of electronic matter. *PNAS*, 102:33, 2003.

[123] V. Brazdova and D.R. Bowler. Automatic data distribution and load balancing with space-filling curves: implementation in CONQUEST. *Journal of Physics Condensed Matter*, 20:275223, 2008.

[124] E. Hernández, M. J. Gillan, and C. M. Goringe. Basis functions for linear-scaling first-principles calculations. *Physical Review B*, 55(20):13485–13493, 1997.

[125] A.S. Torralba, M. Todorovic, V. Brazdova, R. Choudhury, T. Miyazaki, M.J. Gillan, and D.R. Bowler. Pseudo-atomic orbitals as basis sets for the O(N) DFT code CONQUEST. *Journal of Physics: Condensed Matter*, 20:294206, 2008.

[126] E. Hernandez, M.J. Gillan, and C.M. Goringe. Linear-scaling density-functional-theory technique: The density matrix approach. *Physical Review B*, 53(11):7147–7157, 1996.

[127] D.R. Bowler, T. Miyazaki, and M.J. Gillan. Recent prgress in linear scaling ab initio electronic structure techniques. *Journal of Physics: Condensed Matter*, 14:2781, 2002.

[128] X.-P. Li, R.W. Nunes, and D. Vanderbilt. Density-matrix electronic-structure method with linear system-size scaling. *Physical Review B*, 47(16):10891–10894, 1993.

[129] R. McWeeny. Some recent advances in density matrix theory. *Reviews of Modern Physics*, 32:335–339, 1960.

[130] T. Van Voorhis and Q. Wu. Direct calculation of electron transfer parameters through constained density functional theory. *The Journal of Physical Chemistry A*, 110:9212, 2006.

[131] Q. Wu and T. Van Voorhis. Extracting electron transfer coupling elements from constrained DFT. *The Journal of Chemical Physics*, 125:164105, 2006.

[132] William H. Press, Saul A. Teukolsky, William T. Vetterling, and Brian P. Flannery. *Numerical recipes in Fortran 90 (2nd ed.): the art of parallel scientific computing*. Cambridge University Press, 1996.

[133] B. Jansik, S. Host, P. Jorgenssen, J. Olsen, and T. Helgaker. Linear-scaling symmetric square-root decomposition of the overlap matrix. *Journal of Chemical Physics*, 126:124104, 2007.

[134] Adam H. R. Palser and David E. Manolopoulos. Canonical purification of the density matrix in electronic-structure theory. *Physical Review B*, 58(19):12704–12711, 1998.

[135] E.H. Rubensson, N. Bock, E. Holmstrom, and A.M.N. Niklasson. Reverse inverse factorization. *Journal of Chemical Physics*, 128:104105, 2008.

[136] A.D. Becke. A multicenter numerical integration scheme for polyatomic molecules. *Journal of Chemical Physics*, 88(4):2547, 1988.

[137] H. Oberhofer and J. Blumberger. Charge constrained density functional molecular dynamics for simulation of condensed phase electron transfer reactions. *Journal of Chemical Physics*, 131:064101, 2009.

[138] A.S. Torralba, D.R. Bowler, T. Miyazaki, and M.J. Gillan. Non-self-consistent density-functional theory exchange-correlation forces For GGA functionals. *Journal of Chemical Theory and Computation*, 5(6):1499–1505, 2009.

[139] J.D. Watson and F.H.C. Crick. Molecular structure of nucleic acids: A structure for deoxyribose nucleic acid. *Nature*, 171:737–738, 1953.

[140] S. Priyadarshy. DNA conductance: A basic review. *Synthesis and Reactivity in Inorganic, Metal-Organic, and Nano-Metal Chemistry*, 37(5):353–356, 2007.

[141] Y-W. Kwon, C.H. Lee, D-H. Choi, and J-I. Jin. Materials science of DNA. *Journal of Materials Chemistry*, 19:1353–1380, 2009.

[142] Q. Gu, C. Cheng, R. Gonela, S. Suryanarayanan, S. Anabathula, K. Dai, and D.T. Haynie. DNA nanowire fabrication. *Nanotechnology*, 17:R14–R25, 2006.

[143] M. Fischler, A. Sologubenko, J. Mayer, G. Clever, J. Burley, G. Gierlich, T. Carellc, and U. Simon. Chain-like assembly of gold nanoparticles on artificial DNA templates via click chemistry. *Chemical Communications*, pages 169–171, 2008.

[144] D.D. Eley and D.I. Spive. Semiconductivity of organic substanceslong. *Transactions of the Faraday Society*, 58:411–415, 1962.

[145] S. Delaney and J.K. Barton. Long-range DNA charge transport. *The Journal of Organic Chemistry*, 68(17):6475–6483, 2003.

[146] M. E. Nunez, D. B. Hall, and J. K. Barton. Long-range oxidative damage to DNA: Effects of distance and sequence. *Chemistry and Biology*, 6:8597, (1999).

[147] R.G. Endres, D.L. Cox, and R.R.P. Singh. Colloquium: The quest for high-conductance DNA. *Reviews of Modern Physics*, 76(1):195–214, 2004.

[148] E.M. Boon and J.K. Barton. Charge transport in DNA. *Current Opinion in Structural Biology*, 12:320329, 2002.

[149] D.B. Hall, R.E. Holmlin, and J.K. Barton. Oxidative DNA damage through long-range electron transfer. *Nature*, 382:731–735, 1996.

[150] X. Guo, A.A. Gorodetsky, J. Hone, J.K. Barton, and C. Nuckolls. Conductivity of a single DNA duplex bridging a carbon nanotube gap. *Nature Nanotechnology*, 3:163, 2008.

[151] K. Kawai, H. Kodera, and T. Osakada, Y.and Majima. Sequence-independent and rapid long-range charge transfer through DNA. *Nature Chemistry*, 1:156–159, 2009.

[152] Y.A. Mantz, F.L. Gervasio, T. Laino, and M. Parrinello. Charge localization in stacked radical cation DNA base pairs and the benzene dimer studied by self-interaction corrected density-functional theory. *The Journal of Physical Chemistry A*, 111(1):105–112, 2006.

[153] T. Otsuka, T. Miyazaki, T. Ohno, D.R. Bowler, and M.J. Gillan. Accuracy of order-N density-functional theory calculations on DNA systems using CONQUEST. *Journal of Physics: Condensed Matter*, 20:294201, 2008.

[154] S. J. Tans, A. R. M. Verschueren, and C. Dekker. Room-temperature transistor based on a single carbon nanotube. *Nature*, 393:4952, 1998.

[155] A. Nitzan and M.A. Ratner. Electron transport in molecular wire junctions. *Science*, 300:1384, 2003.

[156] S. Ying Quek, M. Kamenetska, M.L. Steigerwald, H. Joon Choi, S.G. Louie, M.S. Hybertsen, J.B. Neaton, and L. Venkataraman. Mechanically controlled binary conductance switching of a single-molecule junction. *Nature Nanotechnology*, 4:230–234, 2009.

[157] T. Terabe, K. Hasegawa, T. Nakayama, and M. Aono. Quantized conductance atomic switch. *Nature*, 433:47–50, 2005.

[158] H. Qian and J-Q Lua. Molecular electronic switch using Carbon nanotube electrodes. *Physics Letters A*, 371(5-6):465–468, 2007.

[159] M. Sauer. Reversible molecular photoswitches: A key technology for nanoscience and fluorescence imaging. *Proceedings of the National Academy of Sciences*, 102(27):9433–9434, 2005.

[160] X. Sallenavea, S. Delbaereb, G. Vermeerschb, A. Salehc, and J-L. Pozzo. Photoswitch based on remarkably simple naphthopyrans. *Tetrahedron Letters*, 46(18):3257–3259, 2005.

[161] M. Irie, T. Fukaminato, T. Sasaki, Tamai. N., and T. Kawai. Organic chemistry: A digital fluorescent molecular photoswitch. *Nature*, 420:759–760, 2002.

[162] M. Maus, W. Rettig, D. Bonafoux, and R. Lapouyade. Photoinduced intramolecular charge transfer in a series of differently twisted donor acceptor biphenyls as revealed by fluorescence. *The Journal of Physical Chemistry A*, 103(18):3388, 1999.

[163] U. Ermler, G. Fritzsch, S.K. Buchanan, and H. Michel. Structure of the photosynthetic reaction centre from rhodobacter sphaeroides at 2.65A resolution: Cofactors and protein-cofactor interactions. *Structure*, 2(10):925–936, 1994.

[164] F. D'Souza, R. Chitta, L.M. Gadde, S.and Rogers, P.A. Karr, M.E. Zandler, Y. Sandanayaka, A.S.D.and Araki, and O. Ito. Photosynthetic reaction center mimicry of a special pair dimer linked to electron acceptors by a supramolecular approach: Self-assembled cofacial zinc porphyrin dimer complexed with fullerene(s). *Chemistry - A European Journal*, 13(3):916–922, 2007.

[165] H. Nakanishi, M.Y. David, E.S. Dy, R. Tanaka, and H. Kasai. CO adsoprtion effects on the electroinc properties of Fe tape-porphyrin. *Journal of Physics: Condensed Matter*, 19:365234, 2007.

[166] Q. Wu, B. Kaduk, and T. Van Voorhis. Constrained density functional theory based configuration interaction improves the prediction of reaction barrier heights. *Journal of Chemical Physics*, 130(3):034109, 2009.

[167] O.A. Vydrov and T Van Voorhis. Nonlocal van der Waals density functional made simple. *Physical Review Letters*, 103:063004, 2009.